AER/AGS Special Report 120

Alberta Energy Regulator

Airborne Geophysics Data Analysis and Interpretation, Southern Alberta

AGS
ALBERTA GEOLOGICAL SURVEY

AER/AGS Special Report 120

Airborne Geophysics Data Analysis and Interpretation, Southern Alberta

A. Brem, G.P. Lopez, D. McGill and J. McKenzie

Ronacher McKenzie Geoscience Inc.

September 2024

ISBN 978-1-4601-5721-3

Brem, A., Lopez, G.P., McGill, D. and McKenzie, J. (2024): Airborne geophysics data analysis and interpretation, southern Alberta; Alberta Energy Regulator / Alberta Geological Survey, AER/AGS Special Report 120, 106 p.

Publications in this series have undergone only limited review and are released essentially as submitted by the author.

Authors address:
A. Brem, G.P. Lopez, D. McGill and J. McKenzie
Ronacher McKenzie Geoscience Inc.
6 – 2140 Regent Street
Sudbury, ON P3E 5S8
Canada

Tel: 705.419.1508
Email: info@rmgeoscience.com

Published September 2024 by:
Alberta Energy Regulator
Alberta Geological Survey
Suite 205
4999 – 98 Avenue NW
Edmonton, AB T6B 2X3
Canada

Tel: 780.638.4491
Email: AGS-Info@aer.ca
Website: ags.aer.ca

Contents

Appendices

Digital Appendix A – Interpretation – GIS files

The appendix is in the accompanying folder entitled 'Digital Appendix A – Interpretation – GIS files', located in the download zip file.

Digital Appendix B – Aeromagnetic map products

The appendix is in the accompanying folder entitled 'Digital Appendix B – Aeromagnetic map products', located in the download zip file.

Digital Appendix C – Automatic detection – Fathom Geophysics

The appendix is in the accompanying folder entitled 'Digital Appendix C – Automatic Detection – Fathom Geophysics', located in the download zip file.

Foreword

The Alberta Geological Survey (AGS) outsourced the geological interpretation of the 2022 and 2023 high-resolution aeromagnetic survey conducted by the Alberta Energy Regulator (AER) / AGS in southern Alberta. This interpretation focused on refining the location of known basement domains (e.g., Medicine Hat domain, Vulcan domain), distinguishing anomalies in the basement (e.g., granitoids, ductile structures), and identifying late brittle faults and dikes in the Western Canada Sedimentary Basin (WCSB). Although this report does not identify any mineral occurrences or potential mineral exploration targets, the information will allow for a better understanding of geological features that are linked to increased critical mineral potential.

All production of geophysical products and interpretation of data was conducted by Ronacher McKenzie Geoscience Inc. (RMG), as well as subcontractor Fathom Geophysics LLC, with oversight and approval by the AER and AGS. Using the 2022 and 2023 aeromagnetic data, RMG synthesized a selection of grid-based filter products to aid subsequent interpretation. Additionally, RMG commissioned Fathom Geophysics LLC to produce automatic structure and radial symmetry detection filters, and other geophysical products. By integrating this new information with existing geological data, the authors' interpretation included modifications to basement domain boundaries, identification of a possible intrusion, delineation of some faults and astroblemes, and correlations to known stratigraphy and petroleum accumulations within the WCSB. Subsequently, a compilation map and report were produced by RMG to highlight all new geological interpretations in southern Alberta. RMG also included an array of new GIS and geophysical products in their deliverables.

This work was completed under the Mineral Grant provided by the Government of Alberta dated June 22, 2021.

Geological Interpretation of the 2022-2023 Aeromagnetic Data

Southern Alberta

Prepared For:

Alberta Geological Survey

Alberta Energy Regulator | AGS Alberta Geological Survey

Prepared By:

Arjan Brem, PhD, P.Geo.
Gloria Lopez, PhD, P.Geo.
Darcy McGill, P.L. (Geo.)
Jenna McKenzie, P.Geo.
Ronacher McKenzie Geoscience Inc.

29 March 2024

TABLE OF CONTENTS

FIGURES

TABLES

APPENDICES

DIGITAL APPENDICES

Digital Appendix A – Interpretation - GIS files
Digital Appendix B – Aeromagnetic map products
Digital Appendix C – Automatic Detection - Fathom Geophysics

1.0 SUMMARY

The Alberta Geological Survey ("AGS") contracted Ronacher McKenzie Geoscience ("RMG") to provide a geological interpretation of the 2023 high-resolution aeromagnetic survey conducted over southern Alberta (NTS map sheets 72E, 72L, 82H, and 82I).

This report presents the results of the geological interpretation, which includes the southern Alberta basement and the overlying Western Canada Sedimentary Basin ("WCSB"). This report supplements the GIS files produced for this project.

The Alberta Energy Regulator ("AER") contracted EON Geosciences Inc. to fly an aeromagnetic survey covering the project area between October 2022 and March 2023. RMG reviewed the digital data for completeness and data quality.

The new aeromagnetic data and the associated images enable improved understanding of the 3D architecture of the basement in southern Alberta. The observations were integrated with and calibrated against existing results of legacy geophysical studies, geological information and regional structural interpretations. Care was taken to avoid mistaking potential cultural magnetic response for geology-related anomalies.

The main conclusions are:

- The magnetic images and the automatic structure and intrusion detection products provide detailed insights into the basement and the overlying sedimentary rocks in the Southern Plains of Alberta.
- Integration with available geological data and public reports highlights an intricate 3D crustal architecture.
- Adjustments to basement domains include edits to the Vulcan domain boundary and division of the Medicine Hat block into three subdomains. This strengthens the structural framework in the region that underpins any tectonic model.
- Faults are ambiguous in their appearance on magnetic images and require integration on a local and regional scale. Many published faults do not have a distinct signature on the magnetic images. For the few faults that do show a correlation, their responses on the magnetic images are equivocal.
- The fold-and-thrust belt contains a distinct magnetic signature that can be correlated with stratigraphy.
- The presence of shallow NW-SE trending magnetic lineaments in the region is persistent. These may not all be Eocene dykes as previously reported; some of these features are interpreted to be stratigraphic boundaries or brittle faults.

2.0 INTRODUCTION

2.1 Project Overview

The province of Alberta has seen an increase in competition over its subsurface usage. Along with the established petroleum sector, recent carbon sequestration, wastewater disposal, helium exploitation, geothermal and mineral (e.g., lithium) exploration projects are part of the Albertan resource sector. In these sectors most projects require fluid extraction from and/or fluid injection into the subsurface. It is expected that competition over the pore space and associated permeability pathways will continue into the future. Thus, it is important to continuously improve our understanding of the subsurface in the region, for economic, environmental, safety and societal purposes.

The basement in southern Alberta is hidden below several kilometers of Paleozoic to Cenozoic sedimentary rocks, therefore the understanding of its architecture, composition and correlation with structures in the overburden is strongly dependant on geophysical studies, including aeromagnetic and gravity datasets.

The Alberta Geological Survey ("AGS") commissioned Ronacher McKenzie Geoscience ("RMG") to complete a geological interpretation of the 2022-2023 high-resolution aeromagnetic survey conducted by EON Geosciences over southern Alberta with the following regional objectives:

- Improve definition of basement features such as the Medicine Hat domain and the Vulcan domain.
- Outline basement anomalies from granitoids to ductile structures in the oldest basement recognized in Alberta (Medicine Hat block)
- Improve the interpretation of brittle fracture networks and Eocene dykes by correlating these with individual magnetic lineaments and broader lineaments bands.
- Identify late brittle faults that may have acted as pathways for fluids (e.g., helium, mineralizing fluids) or hydrocarbon traps.

This report is associated with parallel studies on the Canadian Shield (Lopez et al., 2024) and Northern Alberta (Lopez et al., in progress).

Universal Transverse Mercator ("UTM") coordinates were provided in the datum of WGS 84 zone 11N for all aeromagnetic digital files (vector and map files) and reprojected in ArcGIS to NAD83 Zone 12N for map figures found in this report.

2.2 Previous Regional Studies

Previous regional studies that involve geophysical acquisition and/or geological interpretations include:

- The pioneering work by Hoffmann (1988), Ross et al., (1989) and Villeneuve et al., (1993) where aeromagnetic and gravity data was used to subdivide the basement in Alberta into tectonic domains.

- Burwash et al., (1994) provided geological interpretation of the basement rocks based on petrography, whole-rock geochemistry, and isotopic age determinations carried out on samples collected from oil and gas well cores that had penetrated the basement.

- Lithoprobe was a national research project that studied the 3D structure and evolution of the subsurface in Canada. Studies relating to Lithoprobe's project in southern Alberta can be found in e.g. Hope et al., (1999), Eaton et al., (1999), Lemieux (1999), and Lemieux et al., (2000).

- Ross et al., (1997) documented the presence of distinct small-wavelength aeromagnetic anomalies in the Lethbridge and Milk River region and interpreted these to be Eocene dykes.

- Pilkington et al., (2000) used quantitative and anomaly enhancement methods to emphasize the internal character of domains, and refined the basement subdivision, notably the Vulcan Low.

- Lyatsky et al., (2005; and references therein) used aeromagnetic and gravity data and applied quantitative methods to identify lineaments. They supported the conclusions by Eaton et al., (1995) that basement faults have a control on hydrocarbon traps in the Central Alberta basin.

- McKenzie et al., (2021) completed a regional interpretation of geophysical data for the Peace River Arch and southern Alberta areas as part of a helium and lithium prospectivity project by the AGS.

2.3 Recent Advances

Over the past two decades, advances in computing power have enabled new geophysical data processing methods and visualization techniques, particularly for large scale datasets that would have been previously impossible to process, display, model and interpret. In addition, 3D integration and modelling of subsurface data is now commonplace in all industries, enabled by these same computing advances.

New acquisition of state-of-the-art aeromagnetic data allows better and more accurate analysis of the results, particularly since much legacy aeromagnetic data was flown at very large line spacings, without the spatial accuracy made possible by satellite positioning and navigation systems.

An increasing need for subsurface information by diverse industry sectors proves the value of updated regional mapping initiatives. Many data compilations and linked reports are being made accessible to the public by the Alberta Geological Survey using interactive web applications, such as the structural lineament compilation by Pană et al., (2021). Furthermore, there is growing recognition of the correlations between regional faults, subsurface fluid flow and earthquake occurrences (Alberta Earthquake Dashboard).

2.4 RMG Qualifications

RMG is an international consulting company with offices in Toronto and Sudbury, Ontario, Canada. RMG's mission is to use intelligent geoscientific data integration to help mineral explorers focus on what matters to them. We help a growing number of clients understand the factors that control the location of mineral deposits.

With a variety of professional experience, our team's services include:

- Data Integration, Analysis, and Interpretation
- Geophysical Services
- Project Generation and Property Assessment
- Exploration Project Management
- Resource Estimation and Independent Technical Reporting
- Project Promotion
- Lands Management

The primary author of this report is Arjan Brem, PhD, P.Geo., Associate Geologist at Ronacher McKenzie Geoscience and a geoscientist in good standing with the Association of Professional Geoscientists of Ontario (APGO #3798). Dr. Brem has worked globally as a structural geologist in the petroleum industry since 2007.

Co-author of this report is Mr. Darcy McGill, BSc, P.Geo. (Limited), P.L. (Geo). Mr. McGill is a Senior Geophysicist at Ronacher McKenzie Geoscience and a geophysicist in good standing with the Association of Professional Geoscientists of Ontario (APGO #2010) and Professional Licensee with the Association of Professional Engineers and Geoscientists of Alberta (#316505). Mr. McGill has worked in geophysical data acquisition, processing, and interpretation for mineral exploration since 1995.

A second co-author of this report is Gloria Lopez, PhD, P.Geo., Senior Geologist at Ronacher McKenzie Geoscience, and a geologist in good standing with the Association of Professional Engineers and Geoscientists of Alberta (#181673) and Professional Engineers and Geoscientists Newfoundland and Labrador (# 11213). Dr. Lopez has over two decades of experience working as an economic geologist.

A third co-author of this Report is Ms. Jenna McKenzie, Hons BSc, P.Geo. Ms. McKenzie is co-founder and Principal Geophysicist to Ronacher McKenzie Geoscience and a geoscientist in good standing with the Association of Professional Geoscientists of Ontario (APGO #1653) and the Association of Professional Engineers and Geoscientists of Alberta (#315719). Ms. McKenzie has worked as a geophysicist since 2001 in the exploration and mining industry on a variety of exploration properties with specific focus on geophysics surveying and interpretation.

Additionally, Fathom Geophysics completed the automatic structure, depth to basement and intrusion detection on behalf of RMG.

3.0 PROJECT LOCATION

The project area is in southern Alberta, adjoining Saskatchewan and Montana (Figure 3-1). The survey area lies between latitudes 49° and 51°3'N, and longitudes 110° and 114°5'W, and is covered by NTS map sheets 072E, 072L, 082H, and 082I.

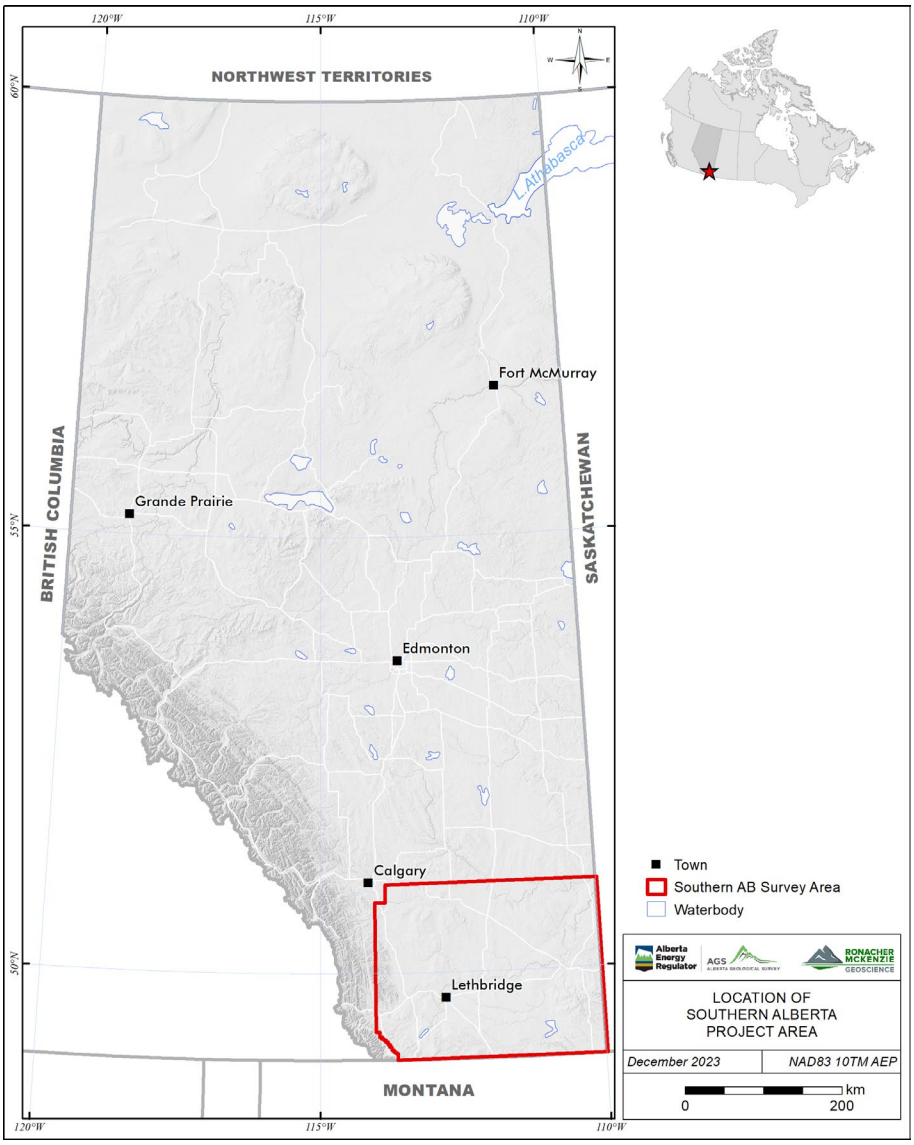

Figure 3-1. Southern Alberta survey area location map.

4.0 GEOLOGICAL SETTING

The southern Alberta project area encompasses the Southern Plains (Prior et al., 2013). It comprises crystalline basement of the Canadian Shield that is overlain by a Middle Cambrian to Cenozoic sedimentary succession. A sliver of the Cordilleran fold-and-thrust belt is located in the southwest corner of the project area (Figure 4-1).

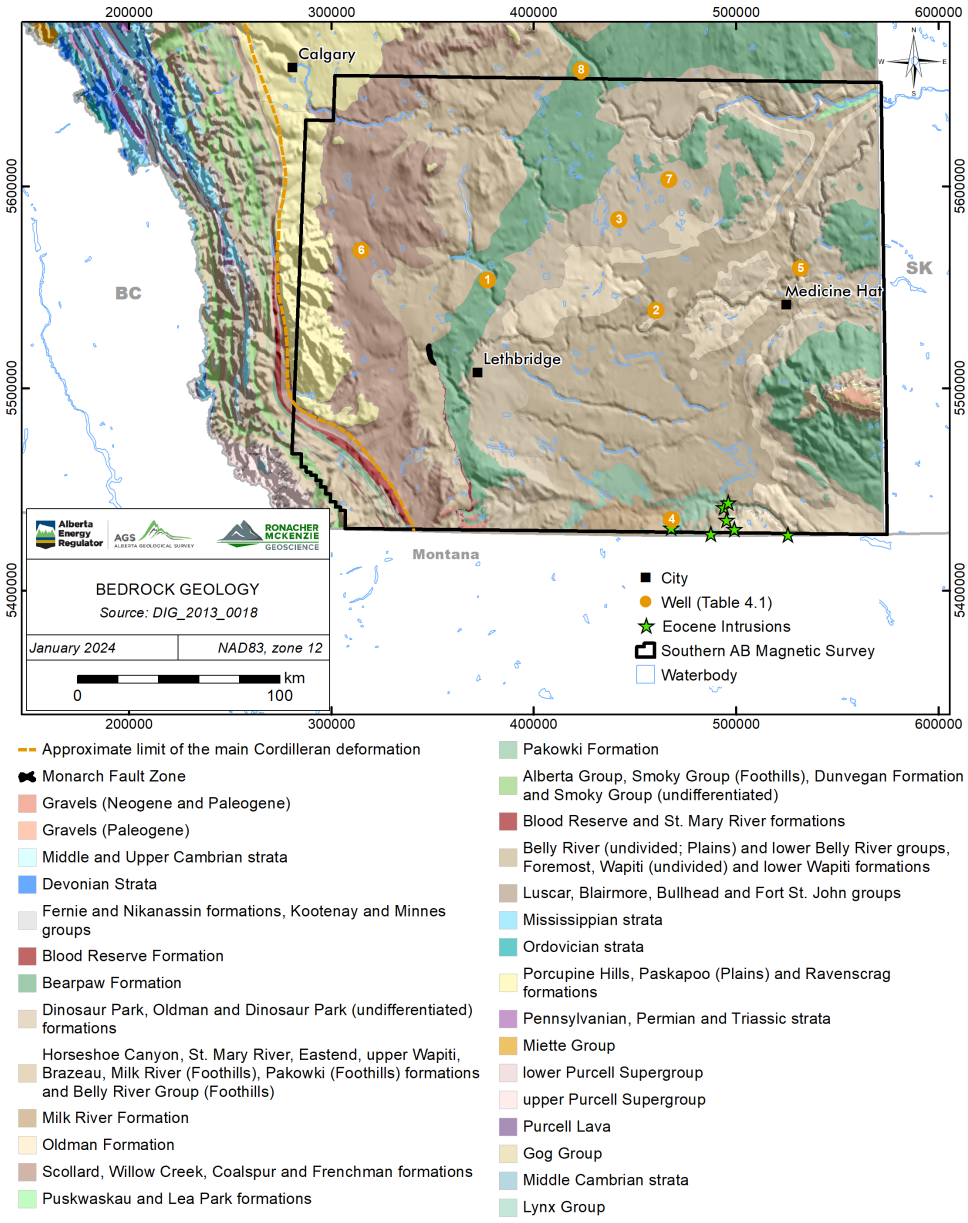

Figure 4-1. Geological map over southern Alberta.

4.1 Crystalline Basement

Crystalline basement in Alberta is comprised of Archean and Paleoproterozoic terranes (Figure 4-2) that were assembled into Laurentia during the Paleoproterozoic (e.g., Hoffman, 1988; Ross et al., 1994; Pană et al., 2021).

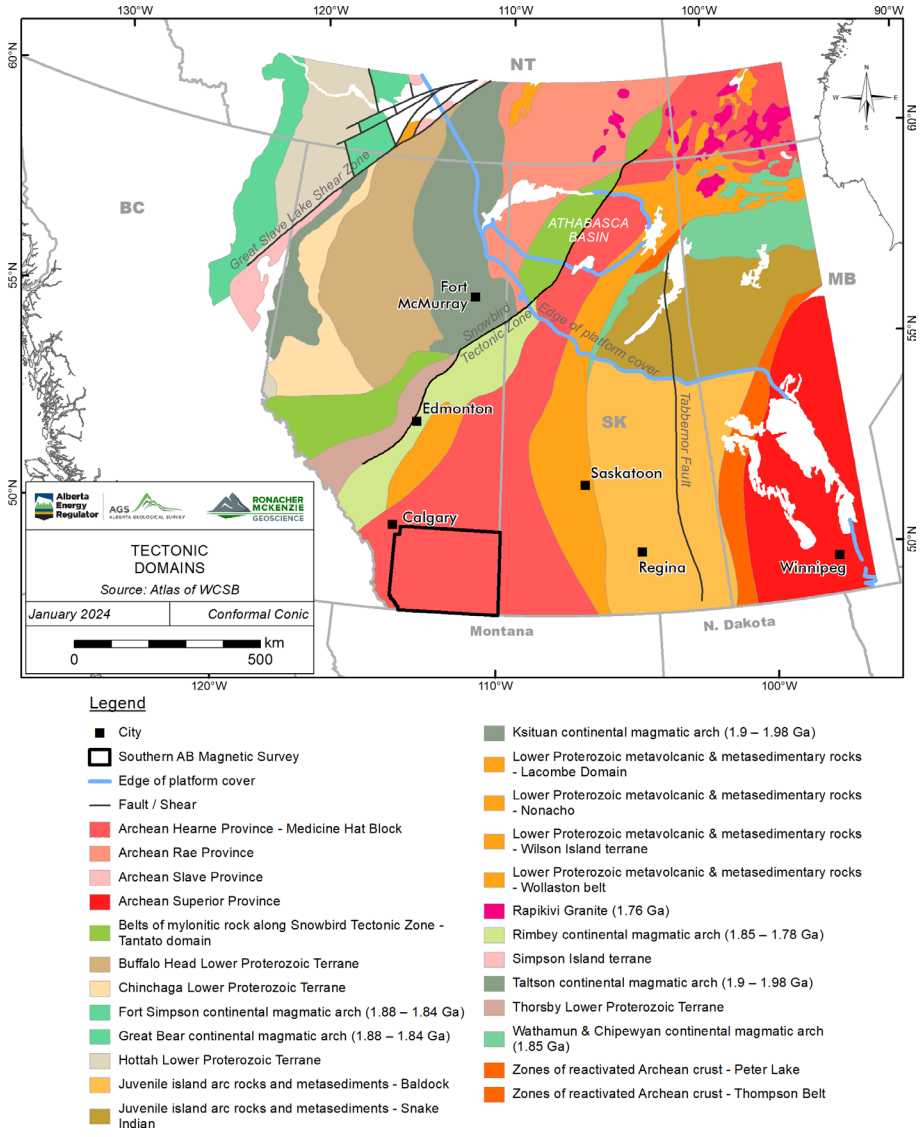

Figure 4-2. Tectonic domains in Western Canada (after Ross et al, 1994).

In southern Alberta, the basement is covered by several kilometers of Phanerozoic sedimentary rocks. Therefore, geophysical tools have long been used to characterize the basement. Lithological and geochronological controls on these basement rocks are based on sparse core samples from eight dispersed petroleum wells (Villeneuve et al., 1993; Figure 4-1; Table 4-1). Further characterization of the crustal architecture in 3D has significantly benefitted from integration with Lithoprobe deep seismic reflection studies (e.g. Hope et al., 1999; Eaton et al., 1999) and resistivity modeling (Nieuwenhuis et al., 2014).

The basement in southern Alberta forms part of the Archean Hearne Province and was subdivided into three distinct domains: the Vulcan domain, the Medicine Hat block and the Matzhiwin high (Figure 4-3; Table 4-1).

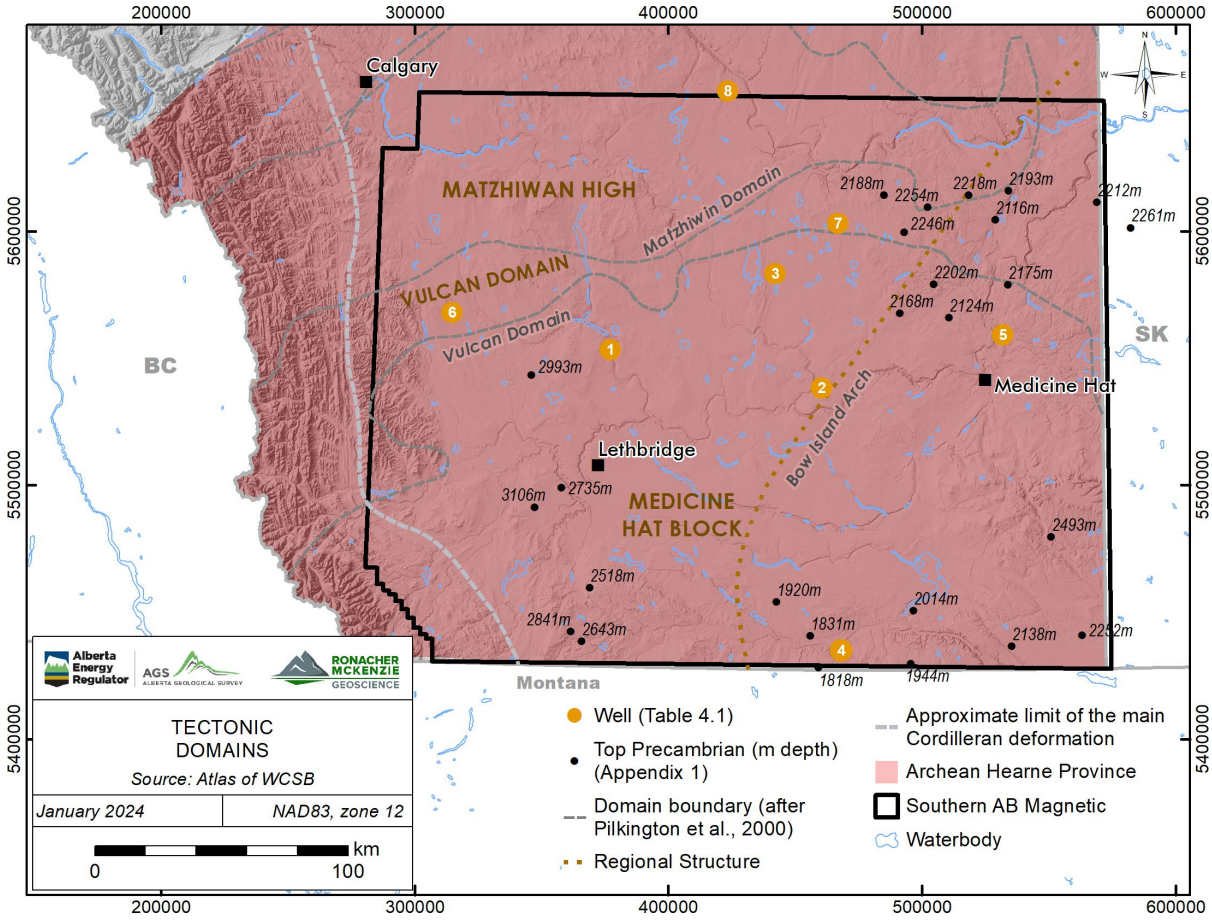

Figure 4-3 Tectonic domains of southern Alberta (domain boundaries after Pilkington et al., 2000).

The Vulcan domain (Vulcan low, Vulcan structure) was established as a distinct, east-trending corridor that is characterized by a magnetic low and a gravity high (Villeneuve et al., 1993). The Vulcan domain juxtaposes two domains with distinctly different aeromagnetic, gravity and seismic fabrics as well as different (modeled) resistivity and density. The crustal architecture and structural evolution of each domain is therefore different. To the north, the Matzhiwin high is characterized by a positive magnetic anomaly (TMI) and a weak northeast trending fabric. Little is known about its lithology. Some reports do not recognize the Matzhiwin high as a separate entity and refer to the area as the Loverna block (e.g. Eaton et al., 1999). To the south, the Medicine Hat block is a large, undifferentiated block that is generally characterized by northwest-trending magnetic fabric. Sampled rocks from this block include weakly deformed to gneissic granites. Although geophysical differences have been documented, the Medicine Hat block has not been previously subdivided.

It is commonly accepted that the Vulcan domain represents a crustal-scale boundary. Differences in the positioning of the Vulcan domain boundaries exist in published reports and there are various tectonic models discussing the structural evolution of the Vulcan domain, including rift basin, collision zone, and suture zone (Pană et al., 2021; and discussion therein).

Table 4-1. Lithological and geochronological constraints from wells (Villeneuve et al., 1993); the ID corresponds to their surface locations on Figure 4-1 and Figure 4-3.

ID	Name	Surface Location	Rock type	Age (Ma)	Domain
1	PCP Travers	01-31-013-20W4	Granodiorite gneiss	2612 $^{+36}/_{-23}$	Medicine Hat block
2	BA Grand Forks	12-14-012-12W4	Biotite quartz monzonite	2721 $^{+35}/_{-30}$	Medicine Hat block
3	Imp Calstan Lake Newell	05-01-017-14W	Pegmatite granite gneiss	2715 $^{+41}/_{-23}$	Medicine Hat block
4	Home Pacific Knappen	16-29-001-11W4	Mylonitic quartz diorite	3278 $^{+22}/_{-21}$	Medicine Hat block
5	PCP Medicine Hat	12-19-014-04W4	Granodiorite gneiss	2.7-2.8 Ga	Medicine Hat block
6	Cal Std Parkland	04-12-015-27W4	Amphibolite	2627 $^{+4}/_{-3}$	Vulcan domain
7	CPOG Princess	10-04-019-11W4	Calcsilicate	n/a	Vulcan domain
8	Mobil CPR Hutton	11-18-024-15W4	Hbl-Bt granitoid	2586 $^{+12}/_{-11}$	Matzhiwin high

The top of the Precambrian basement is constrained by drilling records from 32 dispersed wells (Appendix 1), 30 of which are within the survey area. Depth to basement is more than 1800 m in the south and varies up to greater than 3 km near the Cordilleran deformation front (Figure 4-3). Present-day elevation of the basement varies from 700 m below sea-level in the south, to 1400m in the east and 2500 m in the west.

4.2 Western Canada Sedimentary Basin

The Western Canada Sedimentary Basin ("WCSB") stratigraphy reflects deposition in three different tectonic settings: 1) Mesoproterozoic (1.50–1.32 Ga) intracontinental rift exposed within the Cordilleran fold-and-thrust belt; 2) Neoproterozoic to Middle Jurassic passive continental margin, dominated by carbonates, mudstones and minor evaporites; and 3) Middle Jurassic to Oligocene foreland basin dominated by clastic sequences (Mossop and Shetsen, 1994).

The WCSB comprises two major sedimentary basins: the NW-trending Alberta Basin, which underlies the Interior and Southern Plains, and the Williston Basin, which stretches from the southeastern part of the Southern Plains into southern Saskatchewan and northern Montana. The saddle between these basins is the Bow Island Arch, a subtle structural element in the Paleozoic that became more clearly defined in the Mesozoic and Cenozoic (Wright et al., 1994). The Bow Island Arch joins the northern half of the Sweetgrass Arch at the Kevin-Sunburst Dome, an area with Tertiary igneous activity (Section 4.4).

4.3 Deformation in the Western Canada Sedimentary Basin

4.3.1 Foothills

Evidence for regional deformation is present in the southwestern corner of the survey, where the survey is underlain by outboard sections of the Cordilleran fold-and-thrust belt (Figure 4-1; Pană and Elgr, 2013). Clastic sedimentary rocks of Cretaceous age were deformed and transported to form textbook fold-and-thrust belt geometries. The eastern extent of this regional deformation front is the Cordilleran deformational front.

4.3.2 The Southern Plains

East of the Cordilleran deformational front, numerous NNW-SSE trending extensional faults have been documented based on seismic data; several of these extend from Precambrian basement upward through the entire Cretaceous sequence (Wright et al., 1994; Hope et al., 1999; Schultz et al., 2015; Warren and Cooper, 2017). A complex Cretaceous-Tertiary deformational history that includes extensional faulting, thin-skinned thrusting, and thick-skinned compression including inversion of extensional faults is suggested to have taken place (Warren and Cooper, 2017); but to date, a comprehensive understanding of deformation in a regional context is absent.

4.3.3 The Monarch Fault Zone

The Monarch Fault zone is a unique outcrop in the Southern Plains in which significant deformation is registered (Warren and Cooper, 2017). The outcrop is located along the Oldman River, ca. 10 km northwest of Lethbridge (Figure 4-1). This complex fault zone is mapped as a NNW-trending reverse fault with an east-side-up sense of motion. It juxtaposes the St. Mary River Formation with the Bearpaw Formation, both of Upper Cretaceous age. It is reported that the outcrop coincides with a steep NNW-SSE reverse fault rooted in the basement, possibly an inverted extensional fault.

4.3.4 Local Structures

Localized structures that affect the sedimentary strata have been documented (Mossop and Shetsen, 1994; Prior et al., 2013). Such structures have been mapped using downhole geophysical well logs and seismic sections, and include:

- Structures related to salt withdrawal.
- Structures associated with differential compaction around carbonate reefs.
- Astroblemes; the (eroded) remnants of meteorite impact craters.

4.4 Eocene Igneous Rocks

In the Milk River area near the US border, potassic dykes, small plugs and an intrusive complex are exposed (Figure 4-1, Rukhlov and Pawlowicz, 2012). Most of these potassic igneous rocks are classified as alkali and peralkaline minettes.

The dykes trend N (Bear Creek), NE (Black Butte, Philip Coulee) and ENE (49th parallel). Individually, these narrow intrusive bodies are 0.5-3 m wide and can be intermittently traced on satellite between 200 m and 1 km.

Different radiometric age dating techniques on several igneous bodies yielded a consistent Early Eocene age (52-49 Ma; see discussion in Rukhlov and Pawlowicz, 2012). Temporally and spatially, they correspond to the more extensive Sweet Grass Hills intrusive complex ca. 20 km to the south.

4.5 Quaternary Drift

The Southern Plains are blanketed by a Quaternary drift succession that averages about 30 m in thickness (locally up to 100 m), which commonly restricts bedrock outcrops to coulees. The Quaternary deposits contain alternating series of predominantly till (diamicton) and secondary stratified sediments (lacustrine and fluvial deposits) that record multiple glacial and nonglacial intervals (Mossop and Shetsen, 1994). Of note is that the sediments contain clasts of Precambrian and Paleozoic bedrock that have been glacially transported from the east and north; mapped glacial flowlines and observations from satellite imagery and LiDAR show diverse orientations of transport direction (Atkinson and Utting, 2021).

5.0 AEROMAGNETIC SURVEY DATA

5.1 Data Review

RMG reviewed the digital data available in the AER's archives, for both completeness and data quality. It was determined that the AER data repository was missing final databases; replacement copies were obtained from the airborne contractor. The dataset was collected by EON Geosciences between October 2022 and March 2023 (Alberta Geological Survey 2023).

The aeromagnetic survey was flown at 800 m line spacing, at a nominal terrain clearance of 200 m. The northern portion of the survey area was flown using north-south oriented lines, and the southern portion of the survey area was flown using east-west oriented lines. Tie lines were flown perpendicular to survey lines at 2500 m spacing.

The final processed data were reviewed with reference to the raw measured data to identify any potential data processing and levelling problems. No significant issues were identified.

The airborne contractor (EON Geosciences) applied a combination of filtering and manual editing to attenuate cultural effects in the measured data. Cultural effects have not been completely removed but have been attenuated sufficiently to avoid significant problems with calculated filter products.

5.2 Derivative and Filter Products

Grid-based filter products were calculated from the total magnetic intensity ("TMI") and International Geomagnetic Reference Field ("IGRF") -removed residual magnetic intensity ("RMI") grids (Table 5-1). The various filter products are used to enhance and highlight different features in the measured data to aid in geologic interpretation. RGB ternary images were also created from selected filter products to produce pseudo-structure and pseudo-geology maps.

Table 5-1. Magnetic Filter Products.

Product	Abbreviation	Description
Total Magnetic Intensity	TMI	Measured data.
Residual Magnetic Intensity	RMI	Measured data, IGRF removed.
TMI/RMI, Pole Reduced	RTP	Transform to vertical magnetic field, simplifies anomaly shapes.
X Horizontal Derivative	DX	Highlights near surface features in N-S direction.
Y Horizontal Derivative	DY	Highlights near surface features in E-W direction.
1st Vertical derivative	VD1	Highlights near surface features.
2nd Vertical derivative	VD2	Enhances subtle near surface features.
Analytic Signal (Total Gradient)	AS	Highlights discrete magnetic bodies and zones of high gradients.
Total Horizontal Derivative	THD	Highlights horizontal changes in the total field.
1st Vertical Derivative of Total Horizontal Derivative	THD_VD1	Enhances THD.
Tilt Derivative	TD	Tilt angle between vertical and horizontal derivatives, highlights magnetic contacts, amplitude independent.
Total Horizontal Derivative of Tilt Derivative	TD_THD	Used with TD to estimate depth of discrete magnetic sources.
Area	AREA	Highlights discrete areas.
Edge	EDGE	Highlights edges of discrete areas.
Geology	GEOLOGY	Pseudo-geology map. Ternary image (RMI/RTP, VD1, VD2) only, no grid data.
Structure	STRUCTURE	Pseudo-structure map. Ternary image (DX, DY, VD1) only, no grid data.
Differential Upward Continuation	DIF_XXX_YYY	Highlights features at selected approximate depths.

Selected filter products are presented in Figure 5-1 through Figure 5-9. All filter products are provided to the AGS in a digital appendix to this report.

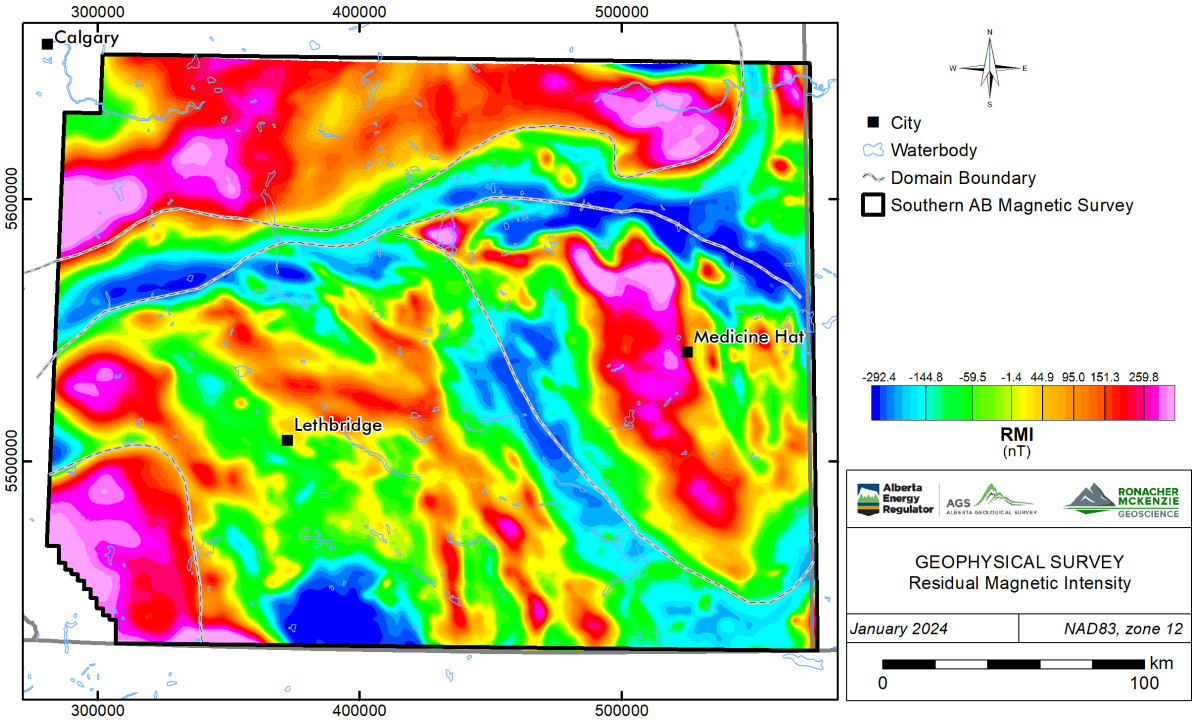

Figure 5-1. Residual Magnetic Intensity ("RMI").

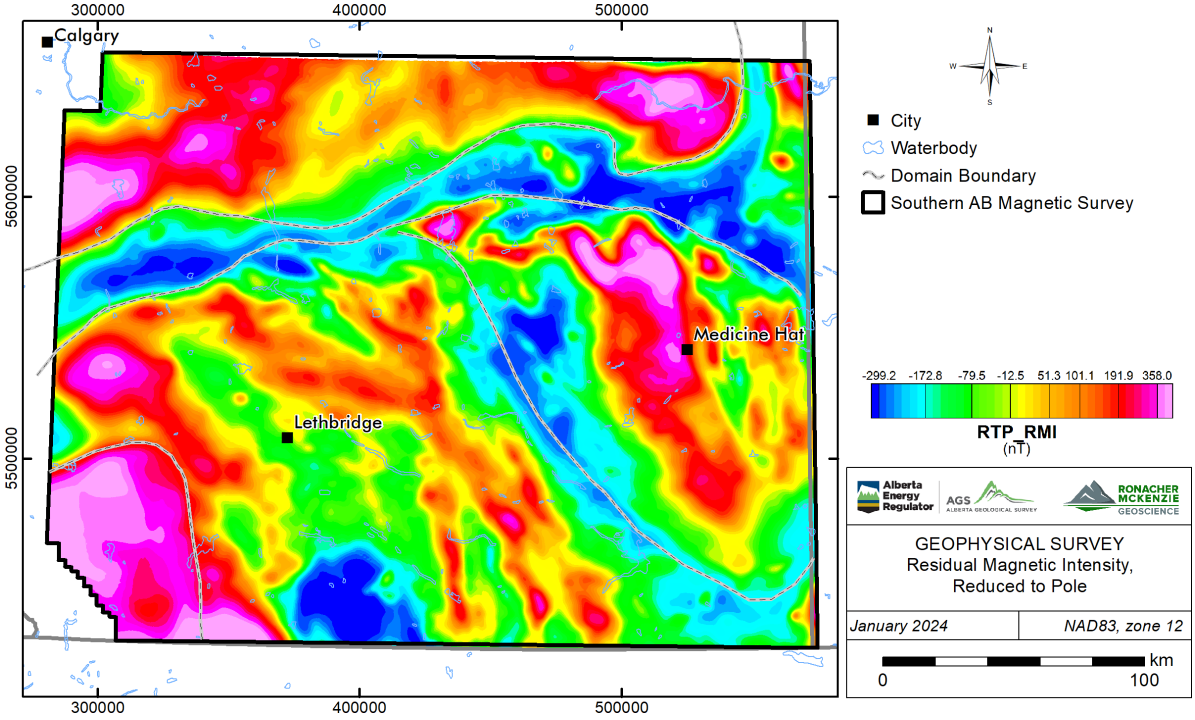

Figure 5-2. RMI, reduced to pole.

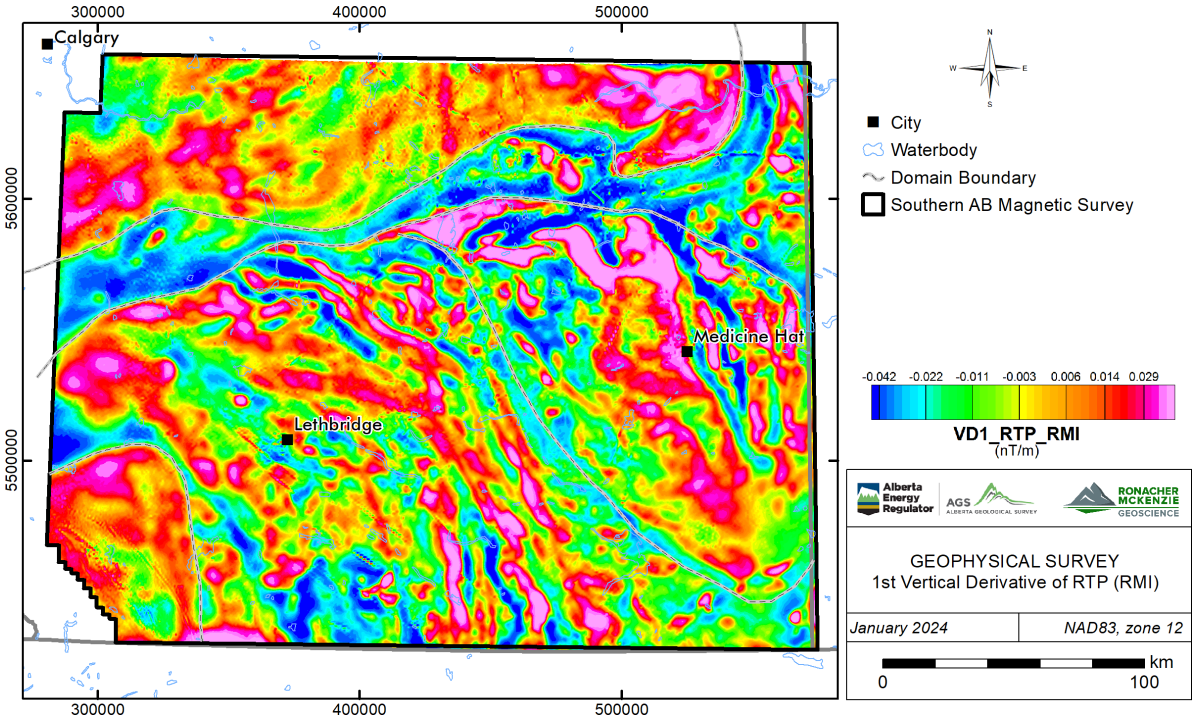

Figure 5-3. RMI, reduced to pole, 1st vertical derivative.

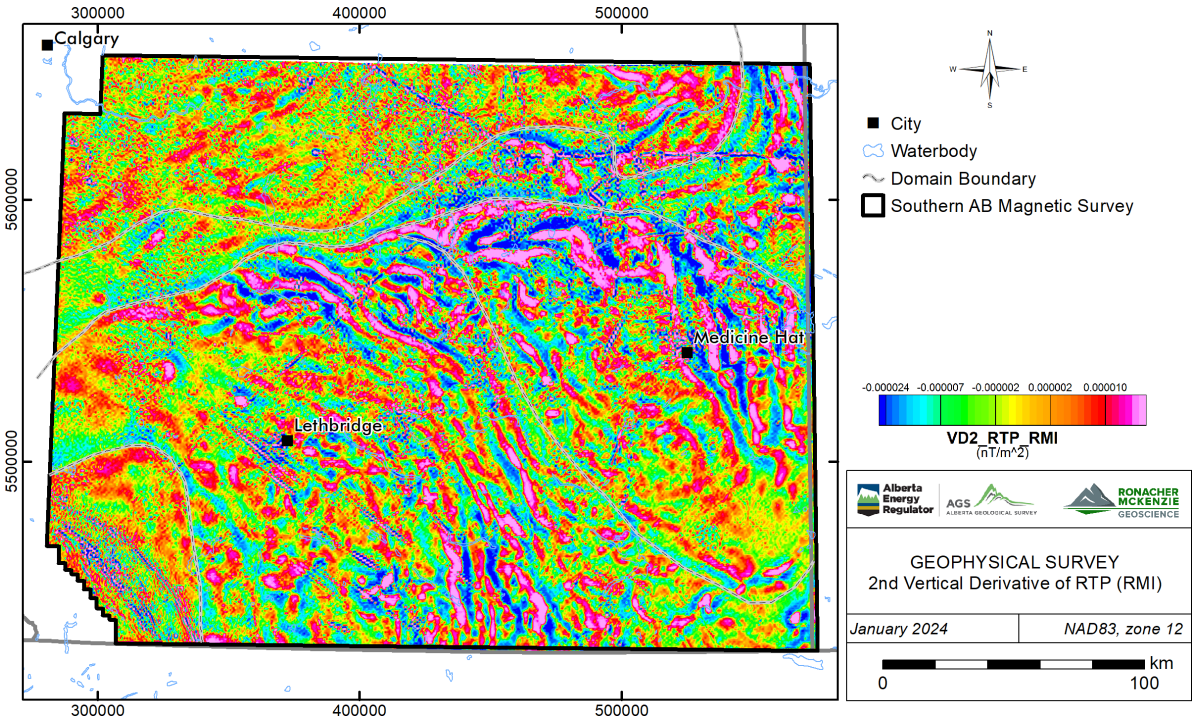

Figure 5-4. RMI, reduced to pole, 2nd vertical derivative.

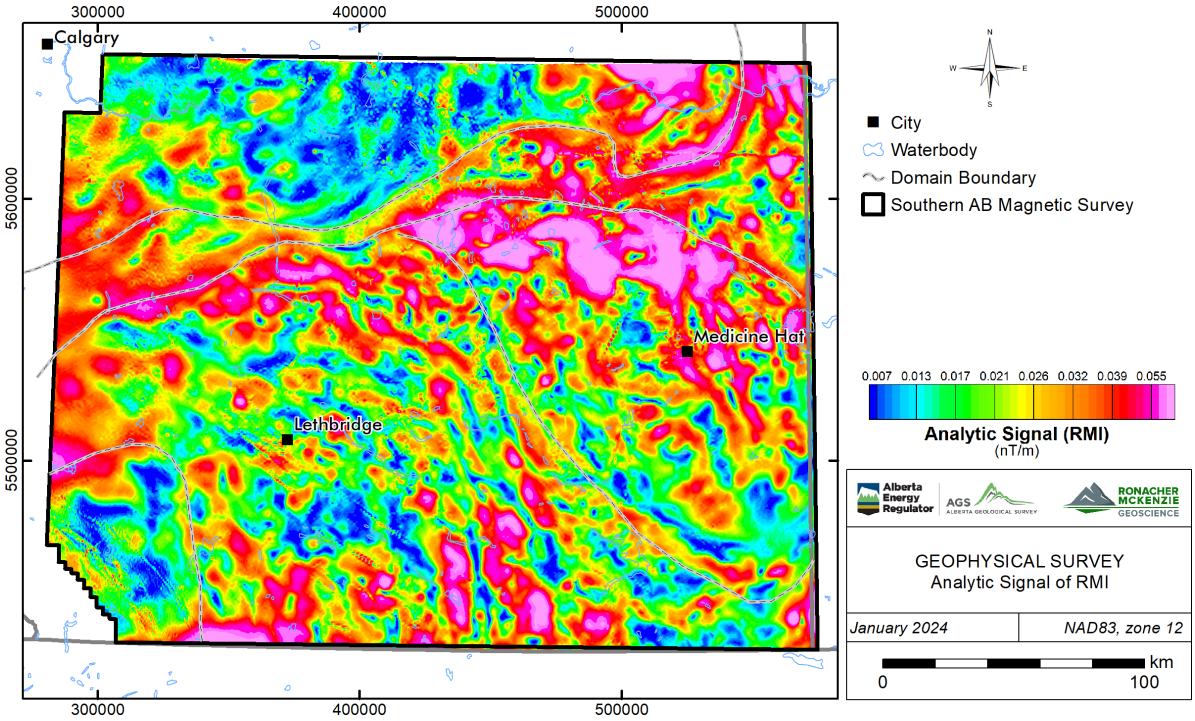

Figure 5-5. RMI, Analytic Signal.

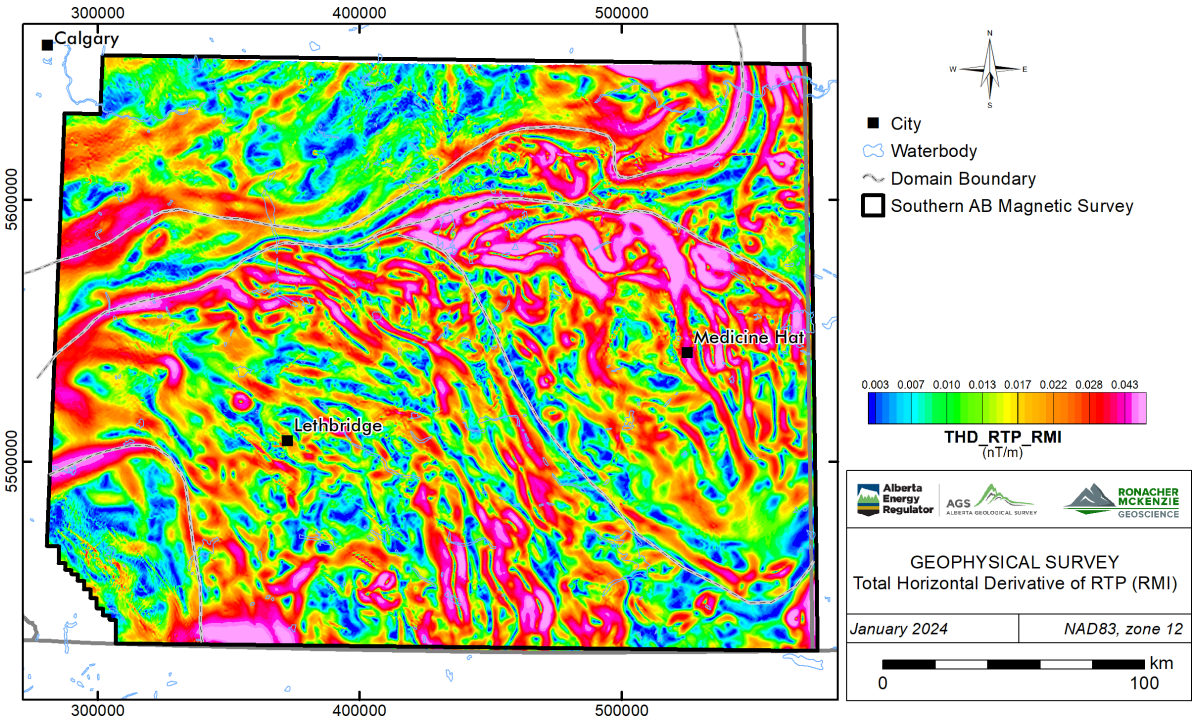

Figure 5-6. RMI, reduced to pole, total horizontal derivative.

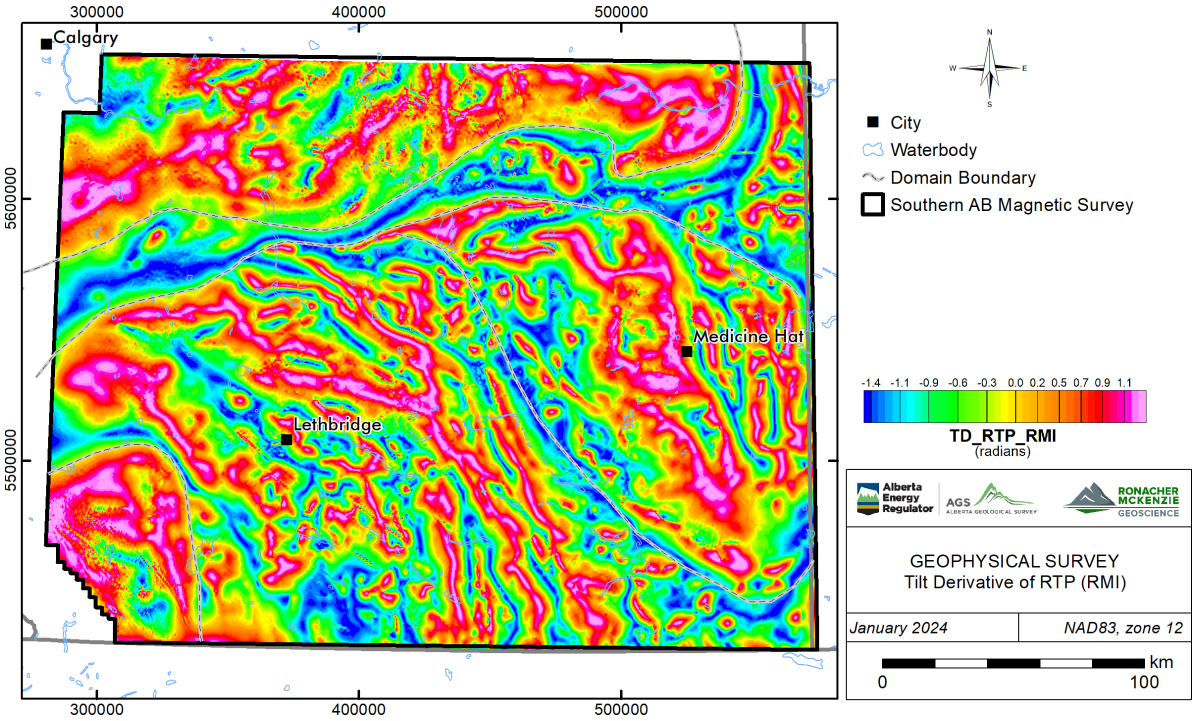

Figure 5-7. RMI, reduced to pole, tilt derivative.

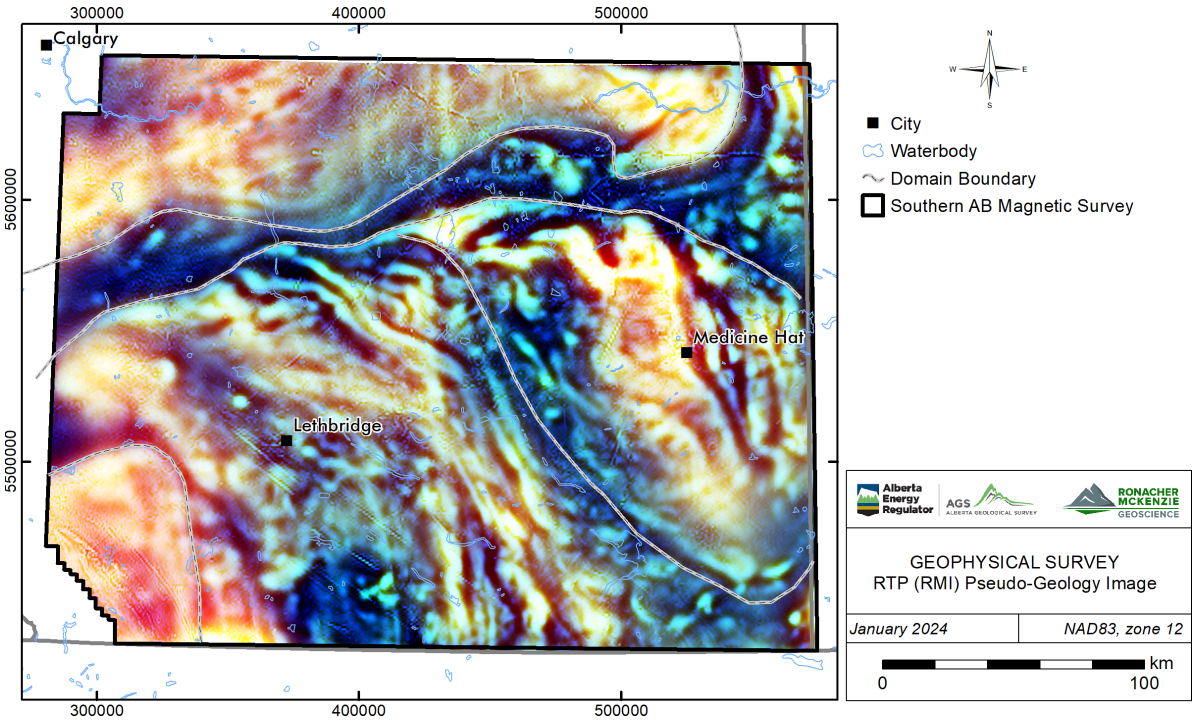

Figure 5-8. RMI, reduced to pole, pseudo-geology ternary image.

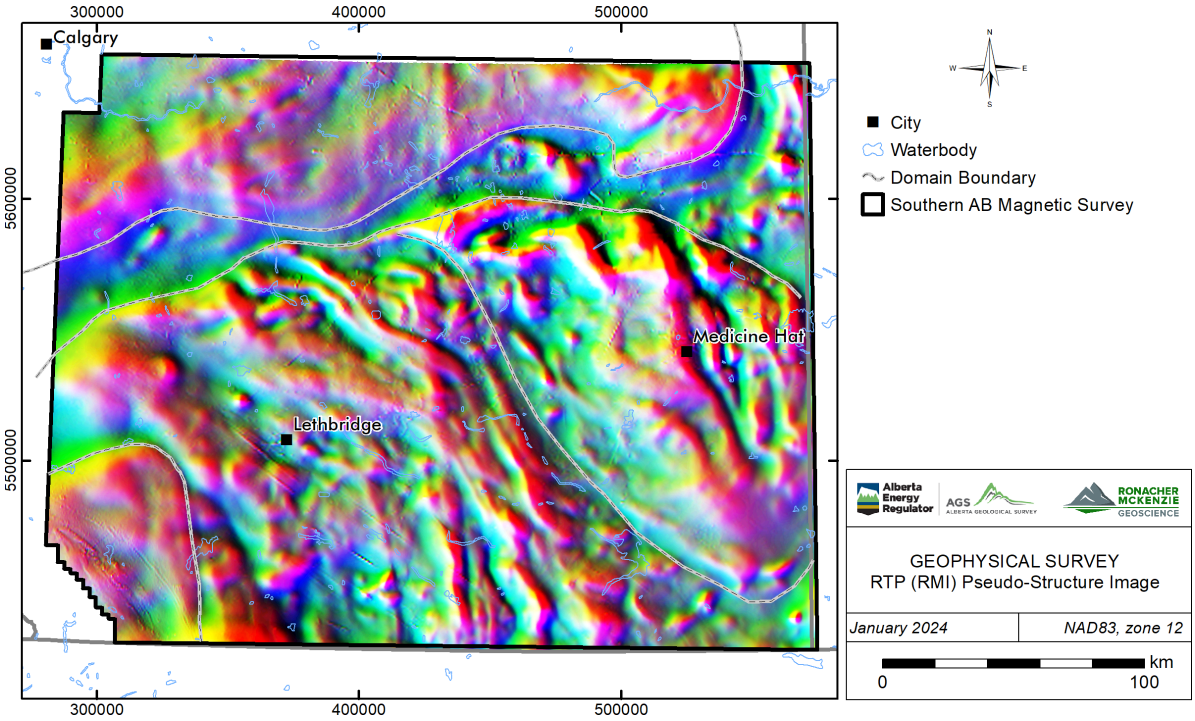

Figure 5-9. RMI, reduced to pole, pseudo-structure ternary image.

Differential upward continuation grids were created to extract information from selected approximate depths, by subtracting grids of the pole reduced RMI upward continued by different distances. Differential grids show information from an approximate depth range equal to half of the upward continuation distances (e.g., the 3000-5000 m differential grid will show information from approximately 1500 to 2500 m depth). Selected differential maps are presented in Figure 5-10 and Figure 5-11.

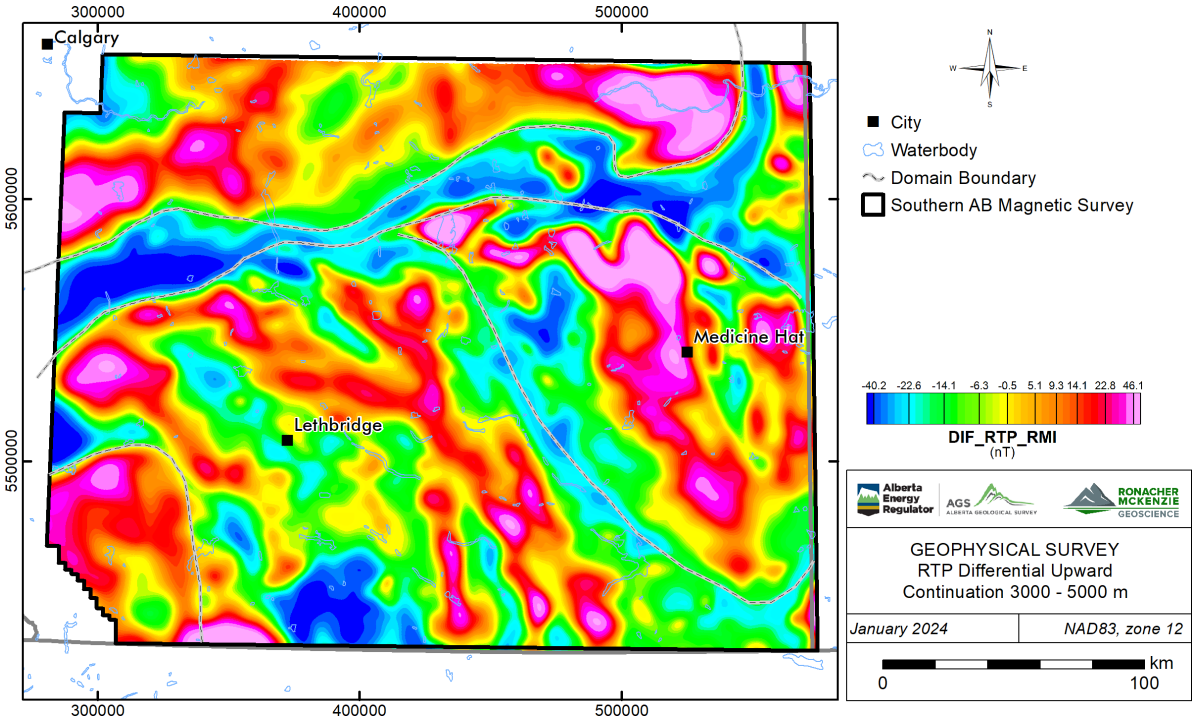

Figure 5-10. Differential upward continuation, 3000-5000 m (1500-2500 m approximate depth).

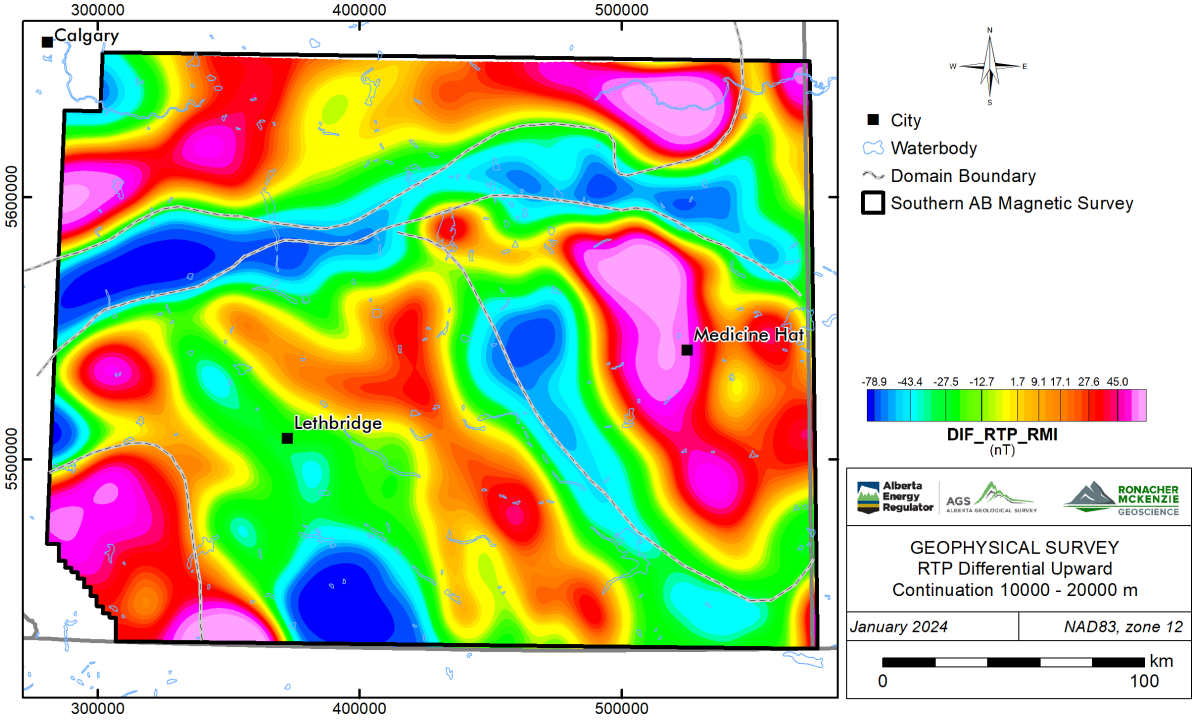

Figure 5-11. Differential upward continuation, 10000-20000 m (5000-10000 m approximate depth).

The gridded magnetic data are also displayed using alternate colour distributions, to aid in data interpretation (Table 5-2). Different colour distributions are used to help identify structures in the interpretation process. For example, greyscale maps are useful for highlighting high and low areas while minimizing the effects of local amplitudes, and isoluminant palettes (e.g., CET i1 described in Kovesi 2015) mitigate artificial highlighting caused by perceived brighter colours in commonly used rainbow palettes, particularly in the yellow and green ranges.

Table 5-2. Colour palettes applied to geophysical datasets.

Colour Distribution	Abbreviation	Description
Rainbow	(none)	Standard blue through purple colour palette.
Greyscale	BW	Black to white colour range, often easier to see structures.
Centre for Exploration Targeting (I1)	CET	Isoluminant colour range developed by University of Western Australia. No 'bright spots' in the spectrum to artificially attract the eye.

Selected examples of alternate colour distributions are shown in Figure 5-12 through Figure 5-14.

A complete set of georeferenced gridded data including alternate colour distributions is included in the digital appendix delivered with this report.

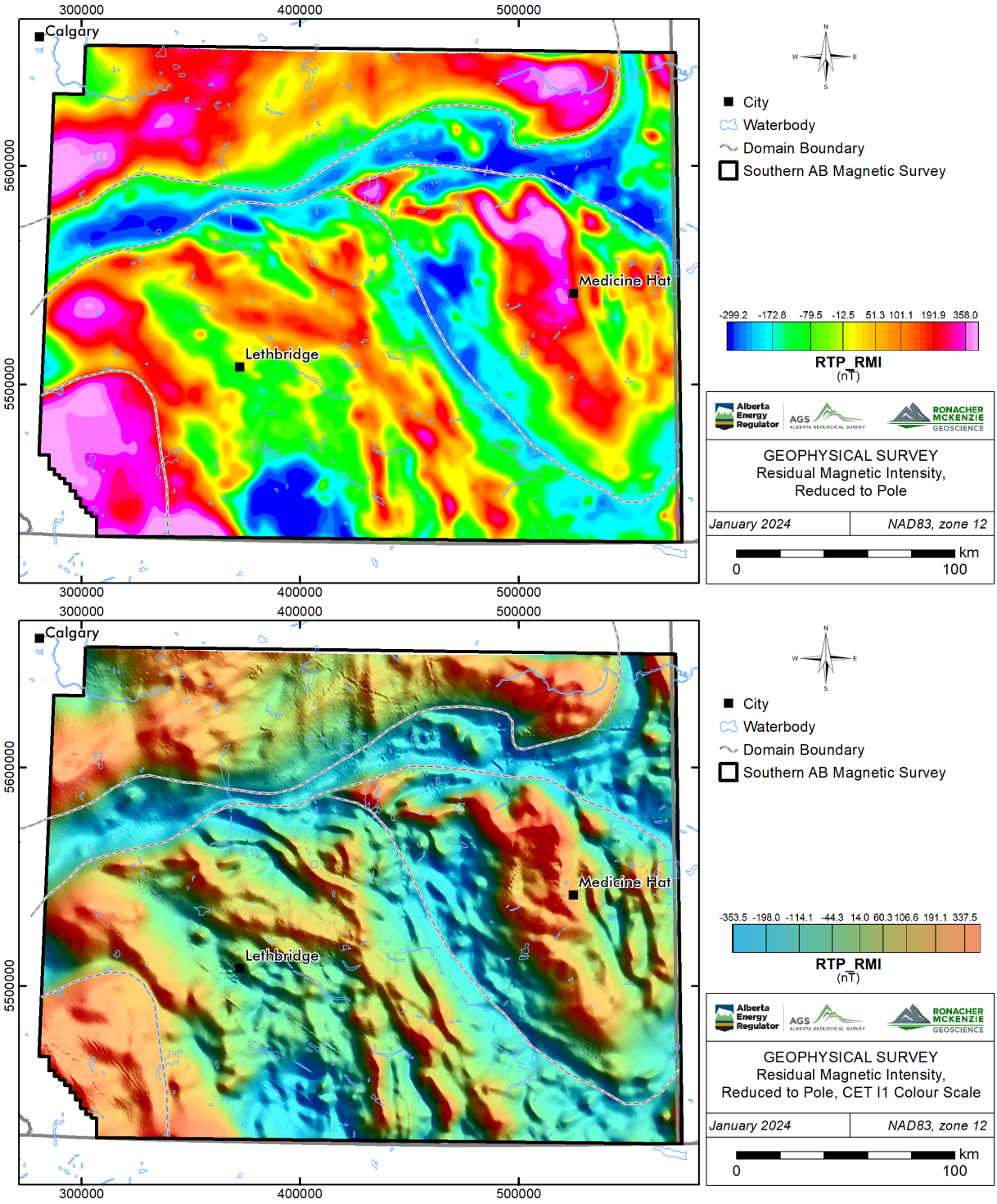

Figure 5-12. RMI, reduced to pole, standard rainbow (top) and CET i1 isoluminant (bottom) colour distributions.

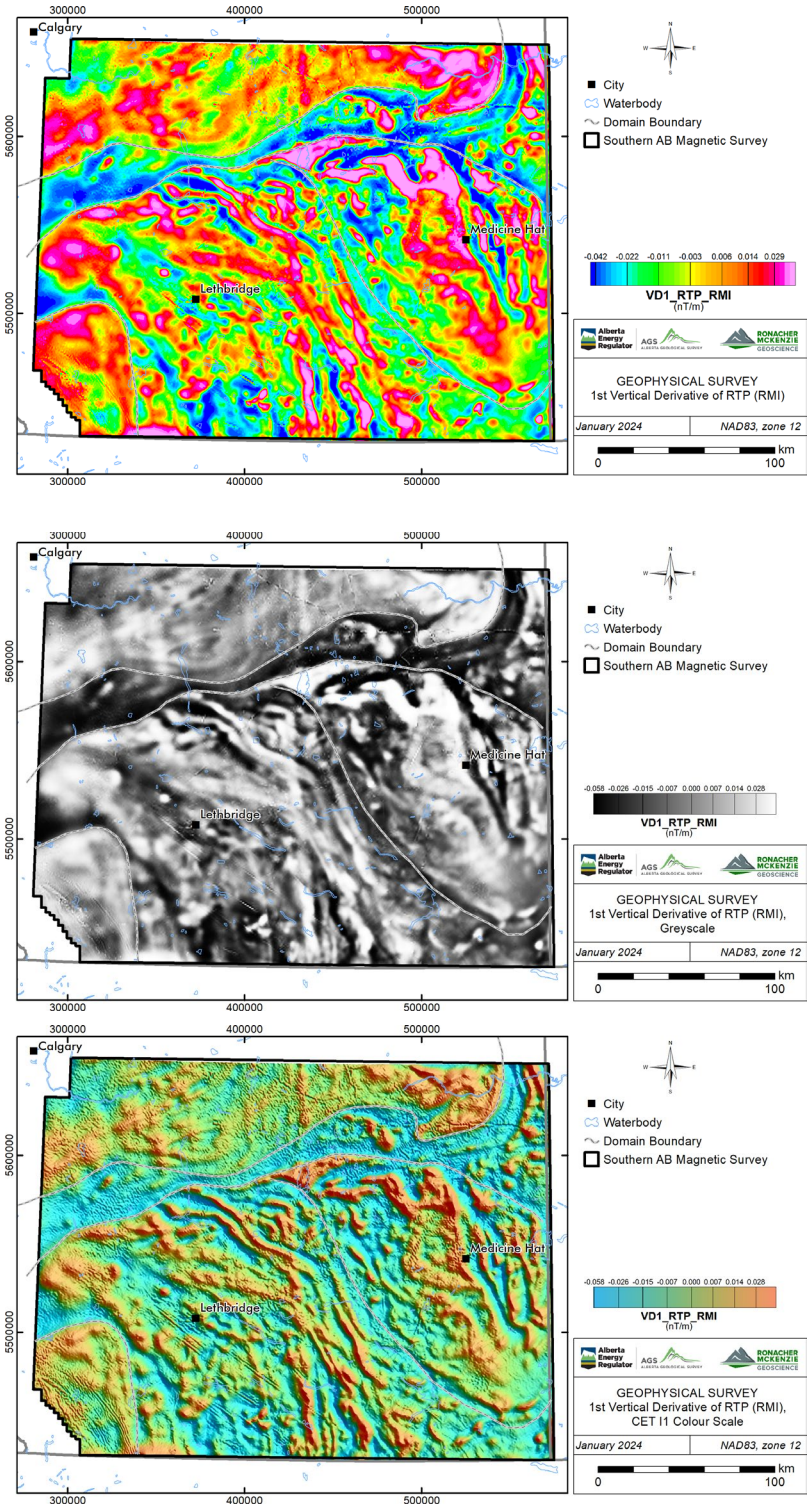

Figure 5-13. 1st vertical derivative (RTP) displayed with standard rainbow (top), greyscale (centre), and CET i1 isoluminant (bottom) colour distributions.

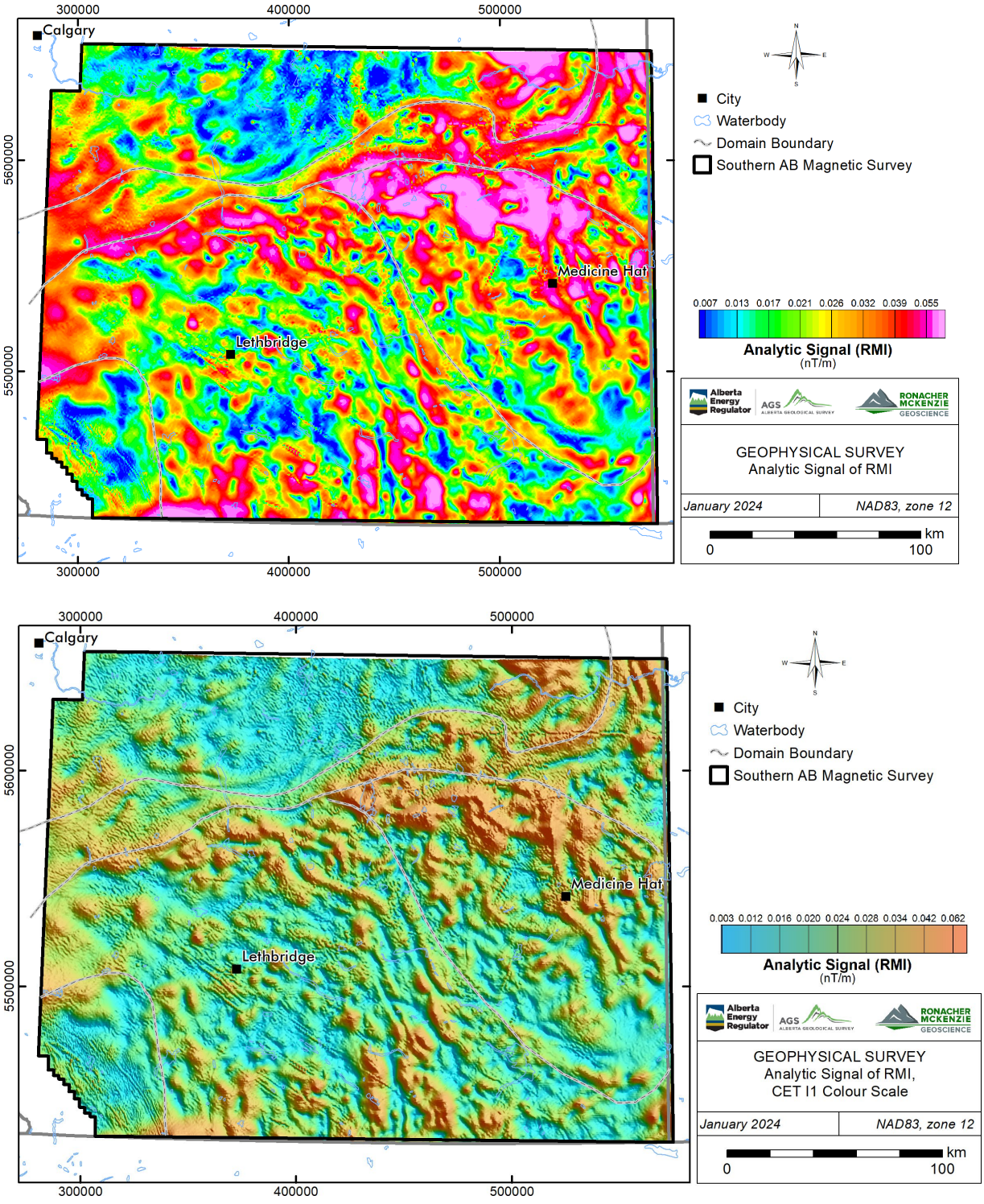

Figure 5-14. RMI, Analytic Signal, displayed with standard rainbow (top) and CET i1 isoluminant (bottom) colour distributions.

5.3 Automatic Structure Detection

RMG collaborated with Fathom Geophysics to perform automatic structure detection and to generate additional magnetic products to assist with the geological interpretation of the magnetic basement in southern Alberta. Automatic structure detection was applied to the gridded magnetic data and the processing included application of standard filters as well as application of Fathom Geophysics' structure detection and radial symmetry filters. The methodology and results of this work are presented in Appendix 2 – Automatic Detection – Fathom Geophysics Report. The final products are in the digital appendix.

The additional filter and image processing products created by Fathom Geophysics are listed in Table 5-3. Grid and image digital files are also attached to this report. An example of an image processing product, a ternary image of 1VD, tilt angle, and horizontal gradient magnitude ("HGM"), is shown in Figure 5-15.

Automatic structure detection filter is a linear feature detection algorithm used to highlight ridges, valleys or edges in gridded data. Automated structure detection is a multi-scale phase congruency algorithm in which features are highlighted either in areas of low or high magnetic contrast, irrespective of amplitude. The method also allows inference of the estimated depth of structures between 0.5 and 1 times the filter wavelength, assuming shorter wavelengths are related to shallow structures and longer wavelengths are related to deeper structures (which may not always be the case). Structure detection products are listed in Table 5-4.

Radial symmetry is a filtering process that identifies equant discrete features in the data. The algorithm seeks locations around which data values either decrease or increase in all directions. These features may be related to stocks, batholiths, cupolas, alteration haloes, kimberlites, diatremes, steep-plunging mineral lenses, and breccia pipes, although all radial features used in interpretation are correlated manually with other data. Radial symmetry products were calculated using wavelengths from 500-2000 m, starting from a number of different residuals. Radial symmetry products are listed in Table 5-5.

Table 5-3. Additional filter and image products.

Product	Abbreviation	Description
Filter Products		
Automatic Gain Control (standard deviation = 30)	AGC30	Evens anomaly amplitudes to make subtle features more visible, longer wavelengths are suppressed.
Pseudogravity	PGrav	Useful for highlighting large scale features.
Pseudogravity residual	PGravRes	Difference between 0-2000 m upward continued pseudogravity. Longest wavelength features suppressed to highlight intermediate scale features.
Horizontal gradient of PGravRes	PGravResHGM	Highlights edges of intermediate scale features.
Small-scale residual	Res500_2000	Differential upward continuation residual, 500-2000 m. Highlights sources at 250-1000 m depth.

Product	Abbreviation	Description
Medium-scale residual	Res2000_5000	Differential upward continuation residual, 2000-5000 m. Highlights sources at 1000-2500 m depth.
Large-scale residual	Res5000_10000	Differential upward continuation residual, 5000-10000 m. Highlights sources at 2500-5000 m depth.
Vertical derivative minus horizontal derivative	VDMHGM	Accentuates contrast in 1st vertical derivative, aids in highlighting shallow features.
Vertical integral	VINT	Vertical integral of total field.
Analytic signal of vertical integral.	VIAS	Produces a result with similar amplitudes and wavelengths to total field, with reduced effects of magnetization direction and remanence.
Image Products		
Ternary of directional derivatives	X_Y_Z	Ternary images (CMY+RGB) of 1st X, Y, and vertical derivatives.
Ternary of 1VD, Tilt, HGM	1VD_Tilt_HGM	Ternary images (CMY+RGB) of 1VD, tilt angle, horizontal gradient.
Ternary of residuals	SmRes_MedRes_LgRes	Ternary images (CMY+RGB) of small, medium, large-scale residuals.
Ternary of RTP, VIAS, Asig	RTP_vias_asig	Ternary images (CMY+RGB) of RTP, analytic signal of vertical integral, and analytic signal. Helps identify remanent zones.
Ternary of pseudogravity	Prav_PGravRes_PGravRes HGM	Ternary images (CMY+RGB) of Pseudogravity, pseudogravity residual, and horizontal gradient of pseudogravity residual.

Table 5-4. Structure detection products.

Product	Abbreviation	Description
Fabric Orientation (RTP and AGC)	Fabric_Orientation	Reflects the orientation of long-wavelength features.
Total Structure (RTP and AGC)	StructX_Total	Total structure detected. X = filter wavelength (100 to 3200 m).
Oriented Structural Domains	StructX_OriDom_Th	Total structure (X = filter wavelength), thresholded into orientation domains.
Vectorized Structure	StructX_Total_Vec	Vectorized total structure (X = filter wavelength).
Belt-parallel structure	StructX_Para	Structure parallel to major belts (X = filter length).
Vectorized belt-parallel structure	StructX_Para_Vec	Vectorized structure parallel to major belts (X = filter length).
Belt-crossing structure	StructX_Cross	Structure crossing major belts (X = filter length).
Vectorized belt-crossing structure	StructX_Cross_Vec	Vectorized structure crossing major belts (X = filter length).

Table 5-5. Radial Symmetry products

Product	Code	Description
Radial Symmetry Highs	Res_X_Y_RSymZ_mi_Lows	Magnitude-independent radial symmetry at wavelength Z from X to Y residual, lows. Also vectorized.
Radial Symmetry Lows	Res_X_Y_RSymZ_mi_Highs	Magnitude-independent radial symmetry at wavelength Z from X to Y residual, highs. Also vectorized.
Radial Symmetry Highs and Lows	Res_X_Y_RSymZ_mi_Highs_and_Lows	Magnitude-independent radial symmetry at wavelength Z from X to Y residual, highs and lows. Also vectorized.

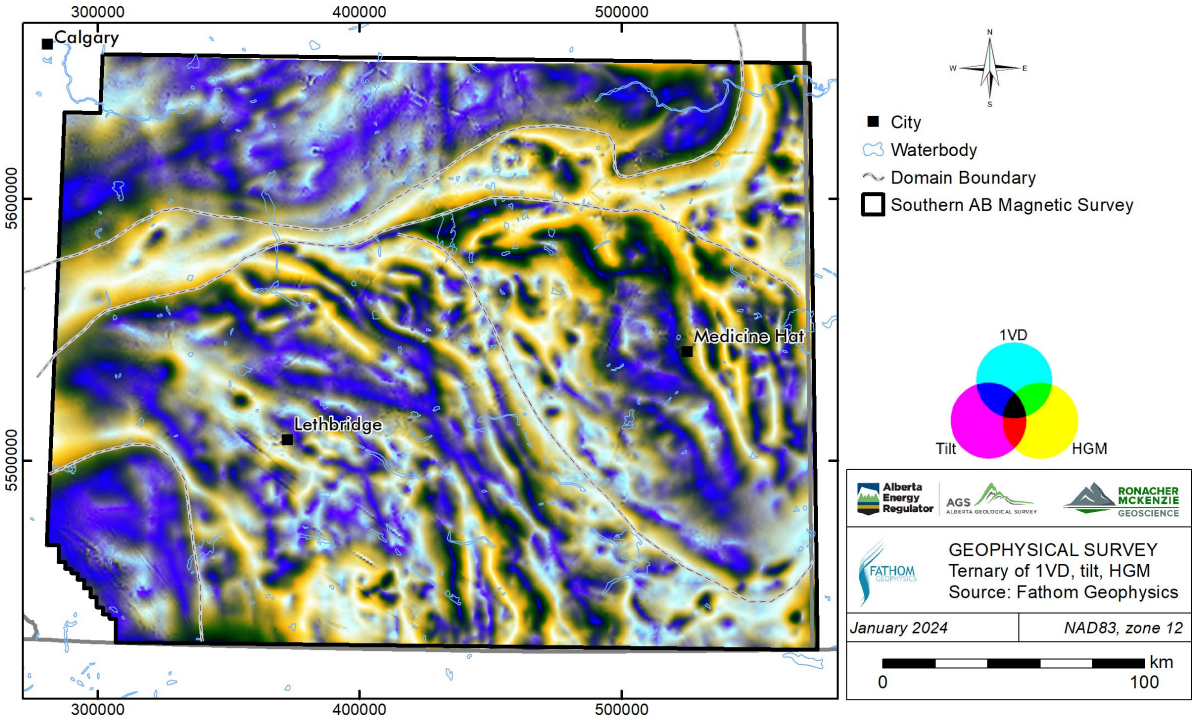

Figure 5-15. CMY ternary image displaying the 1VD, tilt angle, and HGM results from the RTP.

6.0 METHODOLOGY

6.1 Overview

The aeromagnetic and ternary products (Chapter 5) allow for new observations to be made and added to existing studies. Subsequent integration of specific elements allows for fresh insights on the subsurface in the region, which can steer structural interpretations, tectonic models, and subsurface exploration activities.

- The 2022 southern Alberta aeromagnetic survey includes coverage over part of the foothills area, which enables comparisons of aeromagnetic responses at shallow crustal levels between the foothills and the Southern Plains.

- The images are a 2D representation of a 3D structure. Ternary images (for example Figure 5-9, and Figure 5-15) filter out many of the small anomalies and provide a visualization of the subsurface that enables 3D conceptualization of the crust at deeper levels.

- The structure detection products (Section 5.3, Table 5-4) reveal many subtle local features, as well as regionally pervasive trends.

6.2 Workflow

The analysis follows the methodology developed by Isles and Rankin (2013), where the interpretation of aeromagnetic data process is broken down in three main stages: observations, integration, and interpretation. This method is also employed in the associated reports (Lopez et al., 2024; Lopez et al., in progress).

The observation stage is focused on observing features directly from the aeromagnetic images. The interpreter records linear trends and discontinuities as form line features, and magnetic rock units from the anomalies that they cause as polygons. Observations are drawn following linear magnetic highs and gradient trends from several magnetic derivative products (e.g. RTP 1VD). Form lines may represent either stratigraphic or structural trends, and line breaks or juxtapositions may represent a structural element (e.g., fault, shear zone, unconformity or intrusive contact). This stage also includes the definition of domains that outline magnetic characteristics of different regions based on combined form line and magnetic rock unit observations.

The integration stage combines observations with existing geological and other types of data. This stage includes identification and definition of structural elements, magnetic rock units, and changes or disruptions in domains with coherent structural or form line trends. Cross-referencing of the observations with other geophysical datasets, including gravity (NRCan), Lithoprobe seismic (reports), the automatic detection results (Appendix 2) and with the structural lineament compilations (Pană et al., 2021) were done in this stage.

The interpretation stage involves the revision or creation of a structural framework that includes inferences of structural and lithotectonic history. This is the final step in generating an integrated geologic and geophysical

interpretation of an area to present a final geological interpretation map. The compilation of the domains and structure layers is the basis of the structural framework interpretation.

6.3 Challenges

There are several challenges relating to southern Alberta and its magnetic survey that impact the methodology and the results. Subsurface uncertainties will remain and different tectonic models are possible. At local scale, some of these uncertainties can be addressed by integration with proprietary seismic and well data.

- The sedimentary rock units have very little magnetic response at the regional scale (Lyatsky et al., 2005), making it difficult to observe features, such as brittle fracture networks, within the sedimentary sequence.

- The non-magnetic sedimentary layers overlying the basement attenuates the signal from the basement rocks, reducing the resolution of the image. This hinders the detailed interpretation of brittle faults, shear zone architecture and small intrusions (Section 7.4). This impact can be observed in the Canadian Shield, where the magnetic images in the area overlain by the Athabasca basin show a marked reduction in resolution when compared to nearby areas where crystalline basement is exposed (Lopez et al., 2024).

- The lack of exposed crystalline basement hampers the calibration of interpreted intrusions, basement lineaments, and the kinematic interpretation of shear zones.

- Lithoprobe deep seismic lines reveal that crustal structures are shallowly to moderately dipping (e.g. Eaton et al., 1999; Lemieux, 1999; Lemieux et al., 2000), which hampers the detection of discrete lineaments.

- Adding to the point above, magnetic anomalies are overlying each other (Figure 5-1 to Figure 5-15). A 3D depth calibration for the magnetic anomalies remains absent, even though a rudimentary depth assessment of the anomalies can tentatively be put forward based on visual interpretation of the wavelength (shallow vs. deep), differential upward continuation grids (Figure 5-10, Figure 5-11) or depth estimation using exponential filters (Appendix 2).

- The depth of the Precambrian interpreted from well data may be different from the top of the crystalline basement. The database (Appendix 1 and reference therein) does not mention the type of lithology associated with the Top Precambrian structure. For example, the calcsilicate in the CPOG Princess well (#7 in Table 4-1, Figure 4-3) might represent Precambrian stratigraphy (e.g. Purcell Supergroup) instead of crystalline basement. Furthermore, the top of the crystalline basement can be different from the depth of the magnetic anomaly (see also Appendix 2).

7.0 INTERPRETATION AND RESULTS

7.1 Cultural Artefacts

Southern Alberta is a populated region, including widely distributed petroleum industry infrastructure and large towns and cities, such as Lethbridge and Medicine Hat. The survey contractor applied filtering and manual editing to attenuate the effects of culture in the data, but cultural artefacts are still present throughout the survey area. The following cultural features were evaluated against the aeromagnetic images: (1) municipal areas, (2) railways, (3) pipelines, and (4) petroleum related infrastructure. As these features are all near surface, expected signatures include small wavelength anomalies and/or distortion of larger magnetic anomalies.

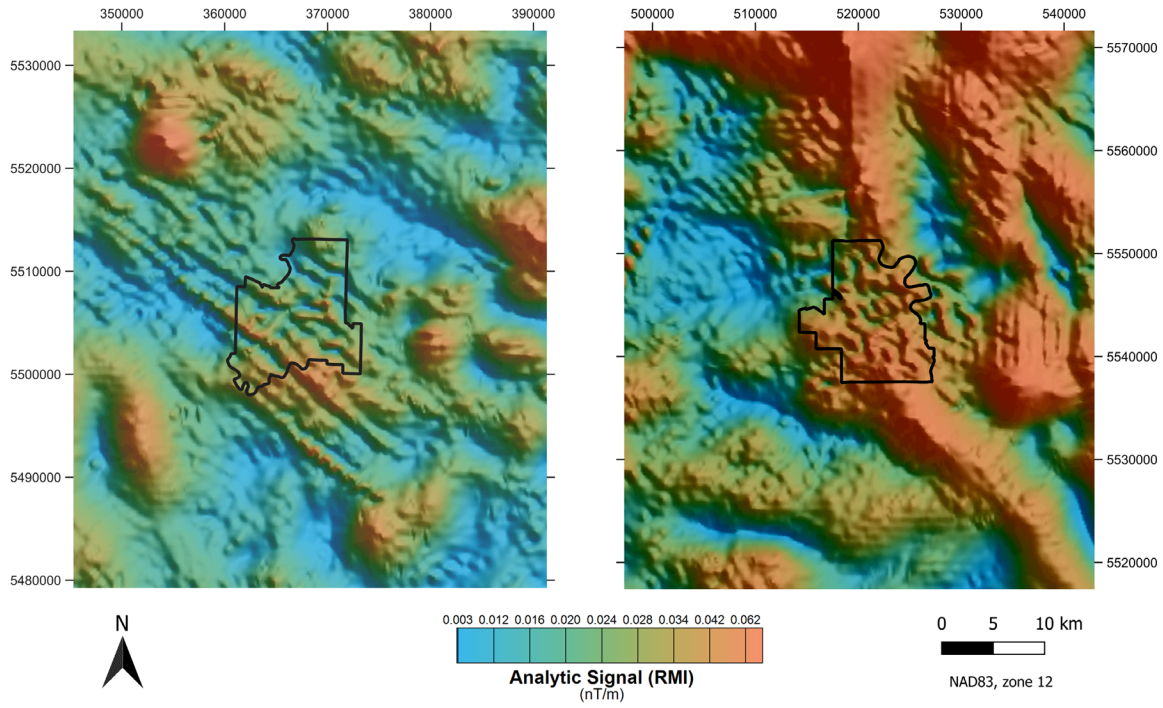

Figure 7-1. Illustration showing impacts of city footprints on the magnetic images. Lethbridge (left) and Medicine Hat (right).

Firstly, in and around municipal areas, the aeromagnetic images should be used with some caution (Figure 7-1). For the city of Lethbridge, the cultural impact appears minimal as both short and long wavelength anomalies appear continuous across. In contrast, for the city of Medicine Hat, the appearance of a strong, broad magnetic anomaly is different between the city footprint and the area outside of it, suggesting a higher impact of this area on the acquisition or imaging of the deeper magnetic anomaly.

Secondly, the regional railroad network does not show on any of the aeromagnetic images. The impact of this cultural component is considered negligible.

Thirdly, there are many pipelines of different sizes and material compositions. The regional trunklines of the NGTL-system (NOVA Gas Transmission Ltd) have a clear impact on the magnetic data (Figure 7-2). The interference pattern shows as a line along which small and large wavelengths anomalies are distorted. Smaller, local pipelines can also have an impact on the aeromagnetic images, especially when several pipelines are co-located (Figure 7-2 left side). Overall, the impact of smaller pipeline grids on the aeromagnetic image appears lower.

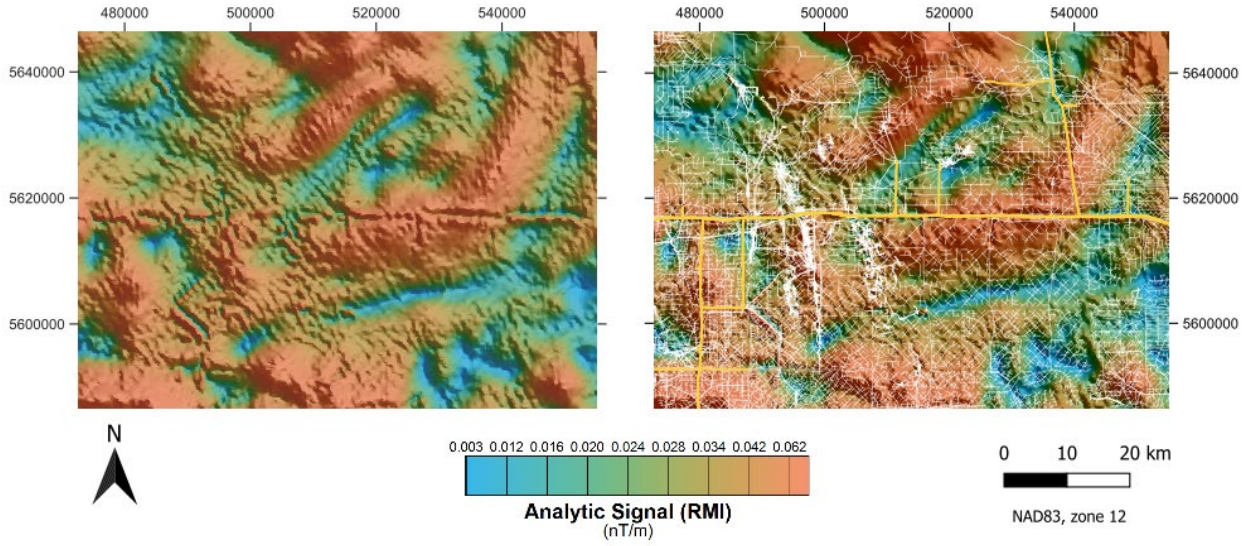

Figure 7-2. Illustration of the impact of pipelines on aeromagnetic images. Regional NGTL trunklines (orange) and other pipelines (white).

Regionally, the density of pipelines increases from southwest to northeast. In areas where few cultural elements are present, many wiggly, small wavelength, low intensity anomalies are visible on the magnetic images. For these rhythmic patterns, a geological reason should be sought. In areas where many smaller pipelines are present and where wiggly anomalies are present (Figure 7-2, top left), distinguishing between cultural and geologic can be difficult; local calibration should be employed.

Finally, there are numerous small anomalies, up to 1 km^2 in size, on different magnetic images across the survey area (e.g. Figure 5-5). In other regions, such anomalies may be interpreted as small intrusions (Lopez et al., 2024). In the study area, many of these are cultural in nature; for example, a gathering station, a processing plant, or a recycling plant (Figure 7-3). However, some small anomalies are not overlain by any cultural feature (Figure 7-4); for these, a geological explanation should be sought.

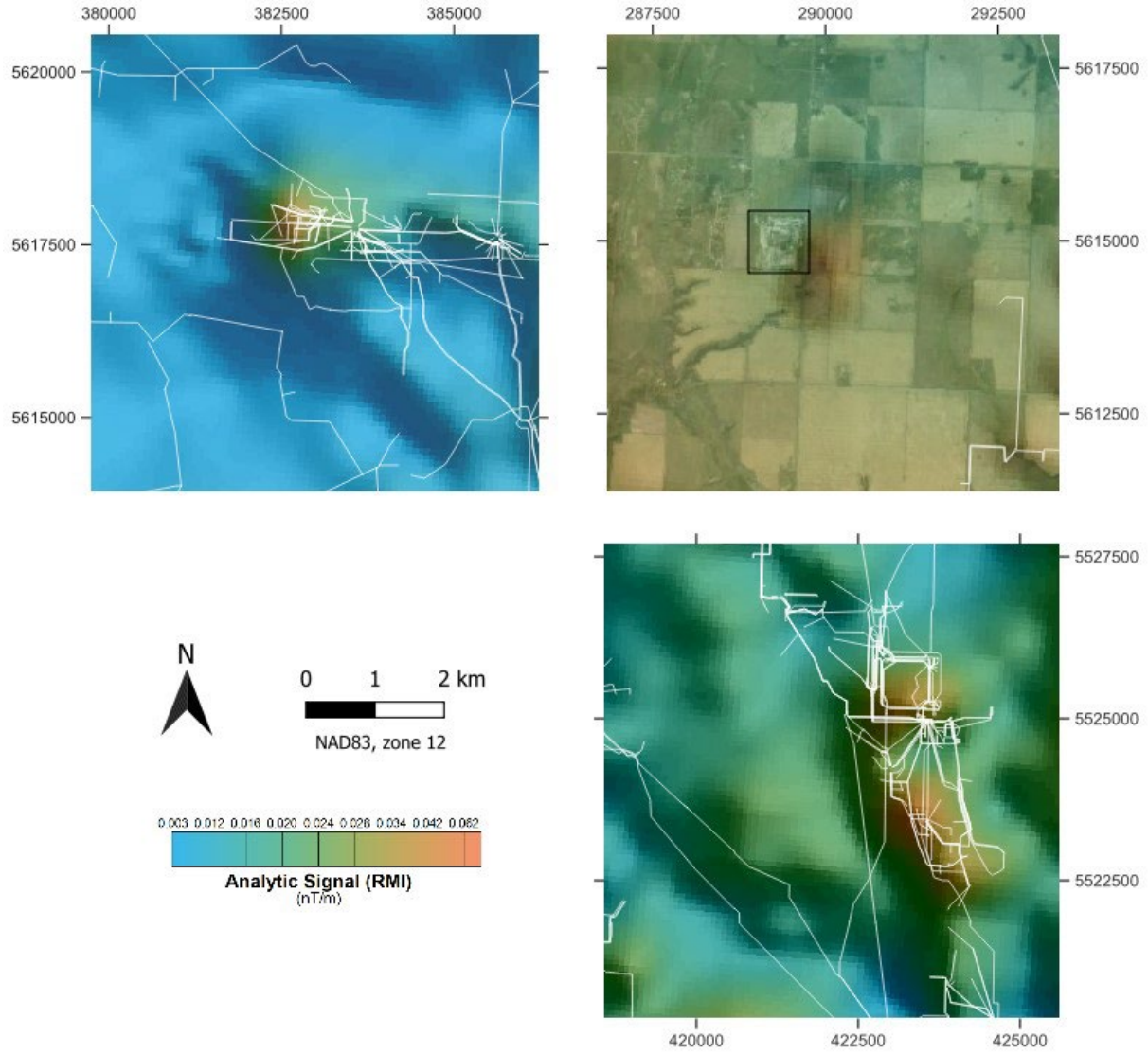

Figure 7-3. Illustration of cultural artefacts on aeromagnetic images (Analytic Signal). Well pads, gathering station and pipeline infrastructure in Vulcan County (top left). A recycling plant (black square) south of Okotoks; satellite image at 50% transparency (top right). Well pads, gathering stations and pipeline infrastructure near Taber (bottom right).

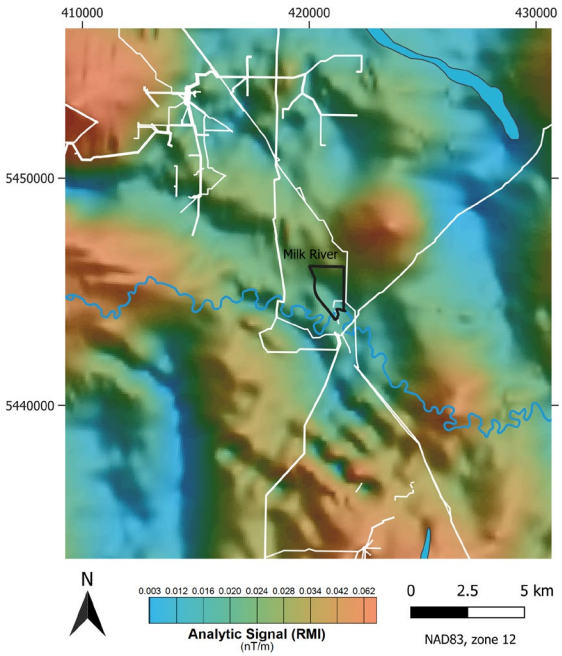

Figure 7-4. Illustration of small positive anomalies in the Milk River area that can be cultural or geologic in origin. Pipelines (white), rivers and lakes (blue).

In summary, there are numerous interference patterns on the aeromagnetic images, many of which are cultural in nature, but some represent geological feature(s). There is no one-size-fits-all solution to filter the artefacts out of the aeromagnetic products. It is recommended that smaller magnetic anomalies are carefully evaluated on a project basis.

7.2 Domain Boundaries

Using the new aeromagnetic products, adjustments to the published domain boundaries are made and have been included on all magnetic images (Figure 5-1 through Figure 5-15).

1. The boundary between the Vulcan domain and the Medicine Hat block is modified by taking out a prominent bulge that was present in the center of the area. The magnetic signature in this bulge resembles the character of the Medicine Hat Block (e.g. Figure 5-13).

2. The Medicine Hat Block is subdivided into three subdomains, each represented by a different geophysical character. The boundaries may not necessarily follow a distinct magnetic lineament and there is lateral uncertainty on the locations of these boundaries due to the potentially shallowly dipping nature of these domain contacts.

    a. MHB_west (Cardston): a small domain that mainly underlies the foothills area. A homogeneous, high magnetic response (Figure 5-2, Figure 5-7), and with a high gravity response (THD).

b. MHB_central (Lethbridge): a central domain characterized by a low-to-moderate magnetic response (Figure 5-2), ample NNW and NW trending magnetic fabrics at various intensities that occasionally appear to be overlapping (Figure 5-3, Figure 5-6), and a variable moderate-to-low gravity response (THD).

c. MHB_east (Medicine Hat): an eastern domain characterized by a dominant magnetic high on the RMI-image (Figure 5-2), it has a variable gravity response (Figure 5-6), and a variable magnetic response on the tilt derivative (Figure 5-7). Locally, north-trending fabrics that deviate into west-trending fabrics are visible.

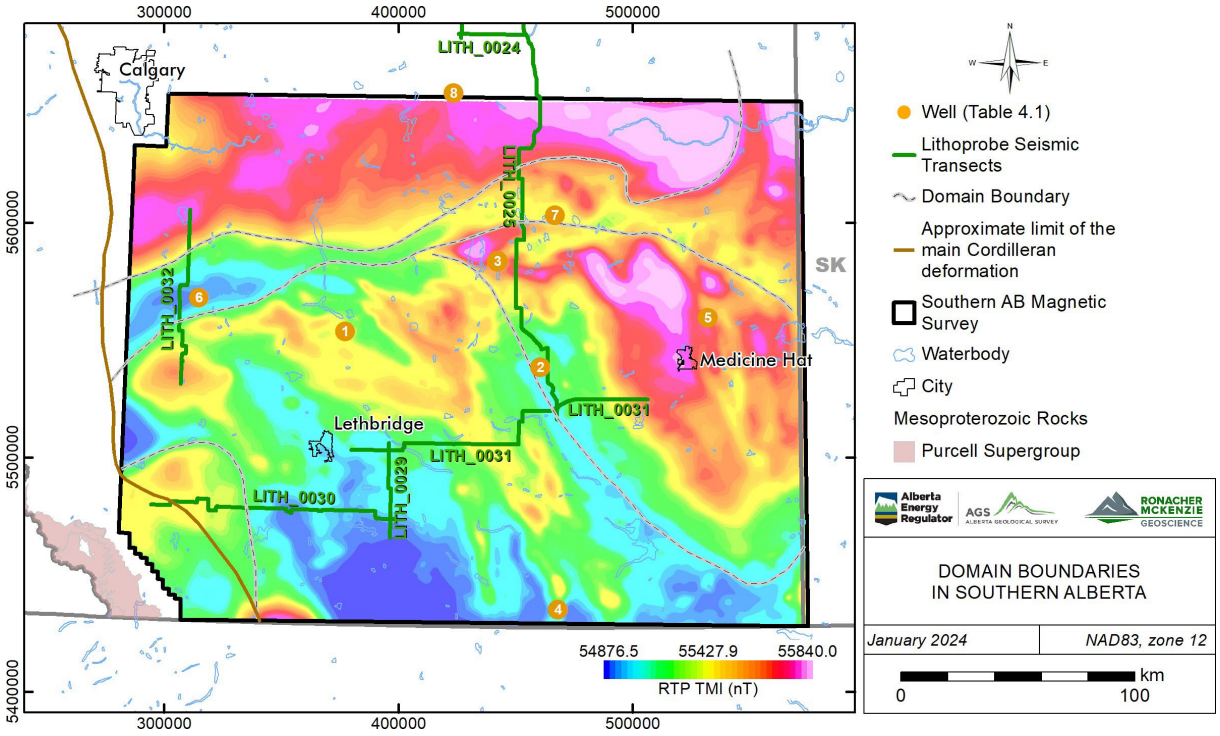

Figure 7-5. Interpreted domain boundaries in southern Alberta (2022 SAB_TMI background). Lithoprobe Seismic Transects were obtained from the Alberta Geological Survey interactive web application (accessed January 2024).

Dividing the Medicine Hat block into subdomains provides an improved structural foundation for the tectonic history of the region.

Firstly, the introduction of a MHB_west subdomain with a northern boundary that is disconnected from the Vulcan domain, emphasizes a spatial correlation between: (1) the MHB_west block, (2) the distribution of Mesoproterozoic rocks of the WCSB in the foothills, being spatially restricted to the region south of the Crowsnest Pass and Blairmore, and (3) the pronounced deviation of the structural trends in the foothills from NW-trending structures to North-trending structures (Figure 7-5; Pană and Elgr, 2013). Basement structures commonly influence overlying structures throughout their geological history; therefore, a genetic correlation between these elements is implied.

Secondly, the division into three subdomains strengthens the crustal architecture of the Medicine Hat block suggested by Lemieux et al., (2000). The NW trending magnetic fabric in the MHB_central domain closely correlates with the imbricated fabric in the middle-to-upper crust interpreted on Lithoprobe seismic sections. Furthermore, the boundary between the MHB_central and MHB_east domains correlates with an inferred basement lineament that is defined by oxygen isotope compositions (Burwash et al., 2000; Pană et al., 2021).

Thirdly, many publications show a widening of the Vulcan domain in the center of the area, around N-S oriented Lithoprobe Line 25 and a Precambrian control well (#7 on Figure 4-3; e.g. Ross et al, 1989; Pilkington et al., 2000). A curvilinear magnetic fabric in this area resembles the fabric of the Medicine Hat block, and some of the magnetic lineaments appear to continue intermittently into the Medicine Hat Block. This half-moon fabric is interpreted to be a continuation of a crustal body in the MCH_east domain that crosses the Vulcan Low at a middle crustal level. This interpretation supports a published interpretation on Lithoprobe Line 25 (Figure 4 in Eaton et al., 1999), on which a zone of south-dipping reflections with strong seismic reflectivity underlies the Vulcan domain and deepens towards the south into the Medicine Hat domains.

The current study has not addressed the definition of the Eyehill block (Villeneuve et al., 1993), or its boundaries with the Medicine Hat and Vulcan domains. Furthermore, the study does not address the presence of the unique Paleoarchean basement sample (3.3 Ga) in a domain dominated by NeoArchean basement samples (2.5-2.7 Ga; Table 4-1). Further integration with geophysical products (magnetic and gravity) on a regional scale is required to address these discrepancies.

7.3 Intrusions

The magnetic expression of the known Eocene intrusions that were discussed in Section 4.4 is subdued and isolated. Only two bodies (Black Butte, Coulee 29) have a local expression on the aeromagnetic images that correspond with their reported dimensions and orientation (Figure 7-6; Rukhlov and Pawlowicz, 2012). The Black Butte intrusive body also has a distinct expression on LiDAR imagery, which correspond to its reported relief of about 30m. Several reasons may exist why these known intrusions do not show on the aeromagnetic images: (1) they are too small to be measured at the resolution of the survey; (2) they may not be regionally continuous; or (3) they do not contain enough magnetic minerals to be detected.

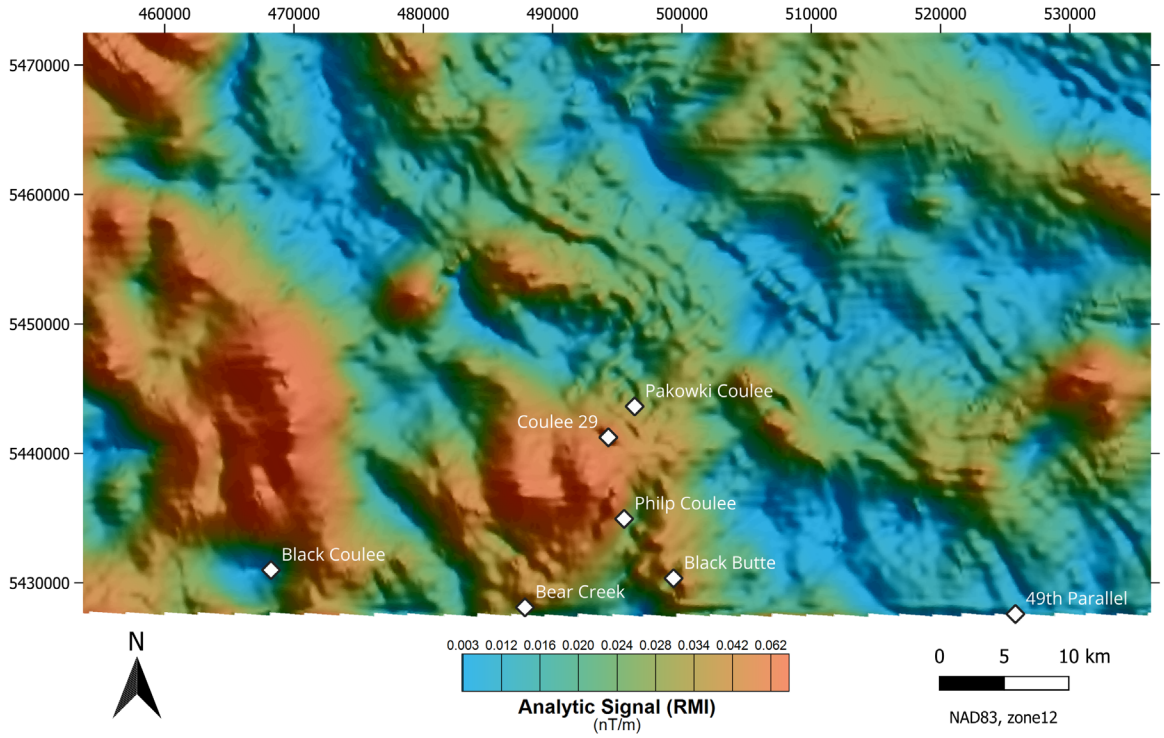

Figure 7-6. Seven documented Eocene intrusions (white dots; Rukhlov and Pawlowicz, 2012) overlying an Analytic Signal image highlighting their subdued magnetic response and lack of regional continuity.

Intrusion detection using a combination of manual and automatic processes was conducted to identify smaller rounded intrusive bodies in the project area. This workflow was successfully applied to the Canadian Shield area (Lopez et al., 2024).

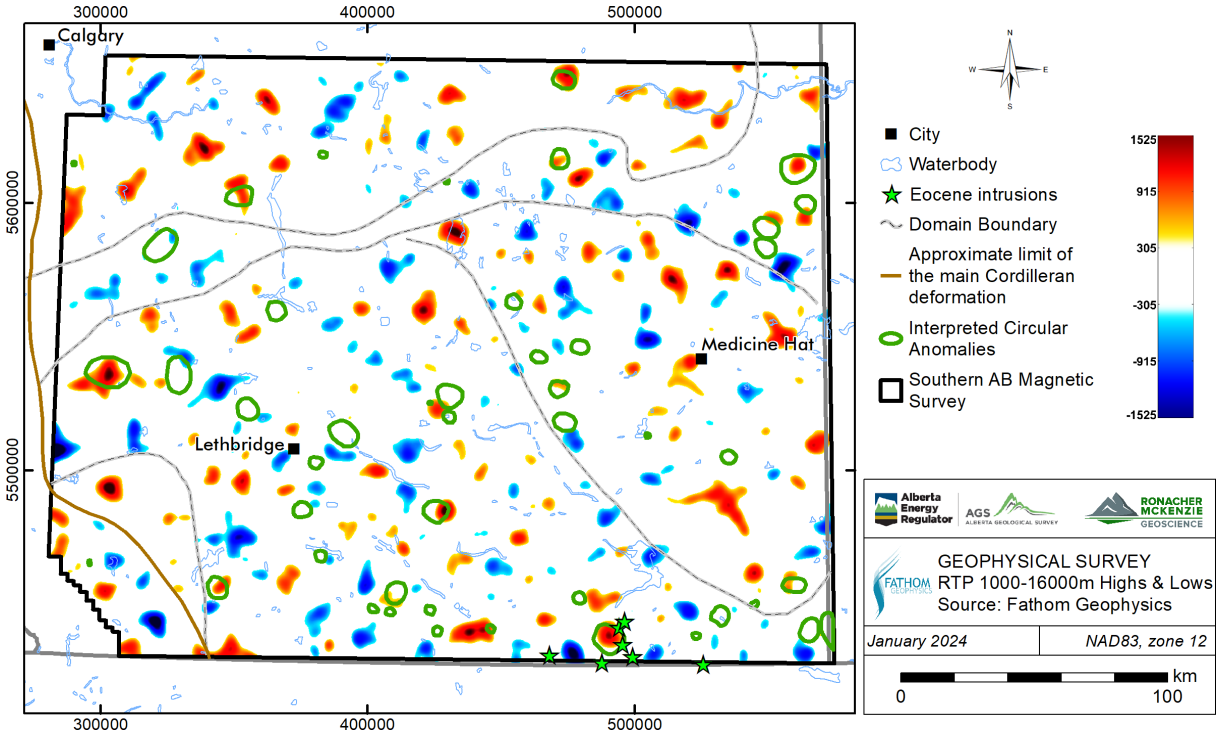

Figure 7-7. Compilation of outcrops of Eocene intrusions (Rukhlov and Pawlowicz, 2012), manual observations of circular geometry, and automated 4000m magnitude-independent radial symmetry results for the RTP data (positive and negative anomalies; Appendix 2).

Many small diameter anomalies, ranging up to 1 km in diameter, can be observed on the aeromagnetic images; Figure 7-7 shows the results of both manual and automated observations. Interpreting these anomalies as intrusive bodies is speculative at best given the uncertainties related to cultural interference (Section 7.1), the paucity of outcrop control, the lack of sample control from well data (e.g. Table 4-1), and the subdued expression of the Eocene intrusive bodies. No further interpretation attempt has been made, with one exception: there is a positive magnetic anomaly of ca. 10 km in diameter near five clustered minettes (Figure 7-7). Given the spatial correlation, this feature is potentially an intrusive body related to the minettes.

7.4 Lineaments, Faults and Shear Zones

Numerous lineaments were inventoried using diverse magnetic images. Overall, the lineaments and trends correlate well with the subsurface lineament compilation (Pană et al., 2021). It is noted that the regionally important Bow Island Arch does not have a distinct signature on any of the images.

When comparing the published faults in the WCSB, which is a subset of the subsurface lineament compilation, against the magnetic images, the following conclusions can be drawn:

1. Many faults in the sedimentary stack do not have a distinct signature on the magnetic images.

2. For the few faults that do show a spatial correlation with the magnetic data, the responses on the magnetic images are equivocal: some faults follow an anomaly, some faults truncate an anomaly, and some faults form a zone across which the magnetic response is showing a dimmed response.

3. Some of the published faults were not observed on the magnetic images but were picked up by Fathom Geophysics' automatic structure detection filters; for example, local faults in the MHB_east domain, and the NE-SW trending lineament adjacent to the Monarch Fault zone (Pană et al., 2021; and references therein).

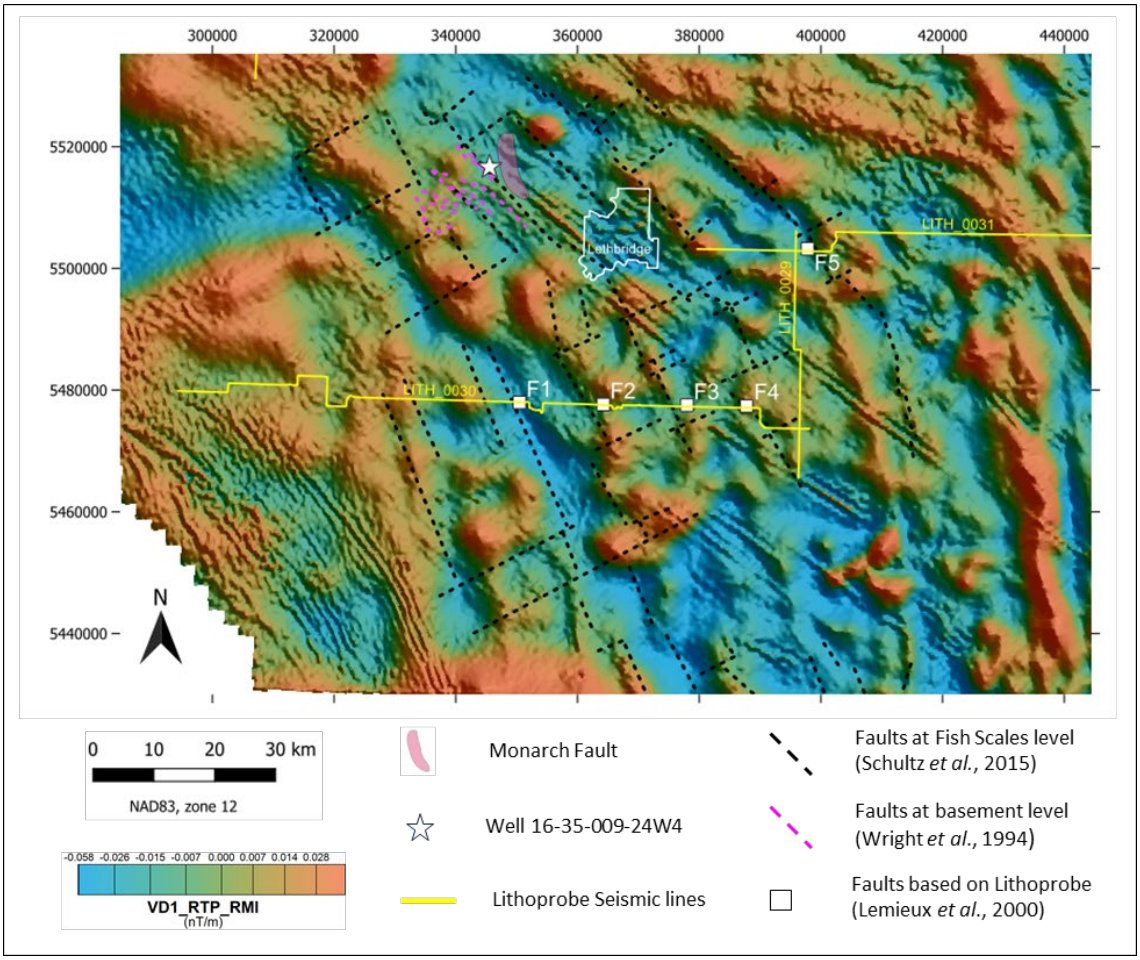

Figure 7-8. Integration of geological datasets illustrating correlations between magnetic responses and documented faults in the basement and the overburden.

For the following three faults, an integration between magnetic observations, lineament interpretation and published fault is discussed, highlighting that faults and shear zones carry expressions on the magnetic image that are different from each other.

Firstly, a legacy 2D seismic section close to well 16-35-009-24W4 from the Fort MacLeod area shows two normal faults about 3 km apart (Figures 3.15 and 3.16 in Wright et al., 1994). Both faults strike NW-SE and have

been mapped to extend over 5 km along-strike. The west-dipping faults offset an interpreted Precambrian horizon at ca. 3 km depth with normal offset of about 0.5 s two-way travel time (TWT).

These faults also penetrate the Upper Cretaceous at a depth of 1.2-1.4 km. The strike of the fault is also NW-SE and west-side-down normal offset can be interpreted. The fault nearest to well 16-35-009-24W4 has an offset in the range of 0.2 km (Schultz et al., 2015).

There are short-wavelength NW-SE trending lineaments spatially associated with these two faults. Since these magnetic features are interpreted as being near-surface (Section 7.7), they most likely do not represent the basement faults. There is no distinct magnetic signature with a broader wavelength aligned with these features that could represent a deeper-seated lineament. Interestingly, the main fault perfectly overlies a high probability trend on the belt-parallel structure detection results for the RTP data (500 m and 1000 m).

The Monarch Fault zone is exposed ca. 3 km to the east of the Fort MacLeod faults (Figure 7-8). The strike of the basement fault in which the Monarch fault is said to be rooted, is unknown, but assumed to trend NNW. There is no NNW-SSE trending magnetic anomaly or boundary in any of the magnetic images.

Secondly, Fault F1 on Lithoprobe Line 30 is a steeply-dipping, inverted basement fault (Lemieux, 1999; Figure 7-8). The mapped offset on the fault at basement level is 0.1 s TWT and the strike of the fault at basement level is not reported. Fault F1 also penetrates the Cretaceous Fish Scales marker horizon (1.4 km depth), where it also has a mapped offset of 0.1 s TWT (Hope et al., 1999). The strike of the fault at the Fish Scales marker is NNW and is interpreted to extend over 25 km (Figure 7-8).

On several aeromagnetic images, a distinct NNW-trending boundary can be observed that spatially correlates with the F1 Fault. On the TMI image, the lineament appears as a low magnetic response. It is accentuated on most ternary images and it has been identified by the automated structure detection filters.

Finally, Fault F5 on Lithoprobe Line 31 is a steeply dipping normal fault (west-side-down) that truncates a significant part of the Phanerozoic layer (Lemieux, 1999; Figure 7-8). Mapped offset on the fault at basement level is 0.1 s TWT, and the strike of the fault at basement level is unknown. Fault F5 also penetrates the Fish Scales marker at 0.7 km depth where it has an estimated offset of 0.2 km (Schultz et al., 2015). The fault is interpreted to extend over 150 km. The strike of the fault at the Fish Scales marker at the Lithoprobe seismic line is NNW. To the north, the fault deviates counterclockwise towards a NW trend; to the south, the fault deviates clockwise towards a N-trend.

This pattern is similar to the curved magnetic fabric in this central area (Figure 7-8). To the north, the fault traces a distinct magnetic anomaly; towards the south, this anomaly cannot be confidently tracked after about 5 km. It appears that the magnetic signature of the fault changes along strike.

In conclusion, not all basement rooted faults are the same; some can be traced on the magnetic images, others cannot. Even along strike, variation in magnetic signature may be present. Establishing a magnetic signature associated with basement rooted shear zones is a challenge that requires local integration and calibration with

other geological datasets. Magnetic and gravity images do provide regional trends (e.g. Lyatsky et al., 2005; Schultz et al., 2015), but the resolution of these products is too coarse to be predictive at higher resolution.

7.5 Depth to Basement

Fathom Geophysics generated a depth to basement surface (Appendix 2), which corresponds with the regional pattern observed in well depth data (Figure 7-9; Appendix 1). Basement in the west is deeper, where it is suppressed by the Cordilleran fold-and-thrust belt. The basement becomes shallower towards the south, towards the Kevin Sunburst dome. The map also highlights a difference in basement depth on either side of the Vulcan domain, with the Matzhiwin high being deeper than the Medicine Hat blocks. Last, some of the Lithoprobe basement faults (Section 7.4) are also apparent on the map.

Where the regional trend is supported by geological data, the absolute values of the surface and the details in the map should be taken with some caution. In areas where well control on the Precambrian basement is available, differences of a few hundred meters can be observed. Furthermore, there is ample topographic variation on the surface itself. Some areas have an underestimated depth to the basement. These are areas where the original data contains high frequencies (Appendix 2). Some areas have an overestimated value for the depth to basement. This could be an indication of non-magnetic Precambrian basement overlying magnetic basement, which may reflect the presence of Mesoproterozoic subbasins underlying the region. One example may be the calcsilicate sample attributed to Precambrian basement the CPOG Princess well (#7 in Table 4-1).

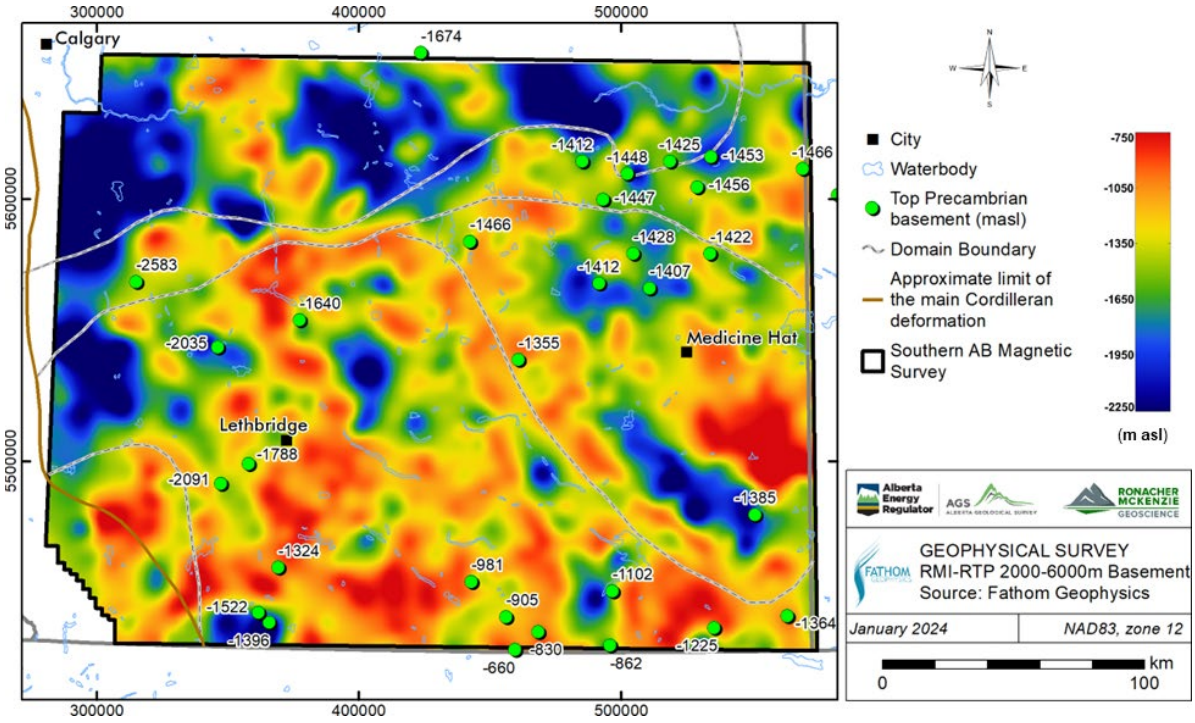

Figure 7-9. Magnetic basement elevation map.

Integration with depth-converted seismic sections should improve the quality of the map and the tectonic interpretation of the area.

7.6 The Foothills

The area west of the Cordilleran deformation front contains numerous small wavelength anomalies that are laterally continuous and subparallel (Figure 7-10). There is little to no cultural interference in the foothills region, hence these features are considered to be geological in nature. They can be grouped into areas with similar magnetic response, notably on the Analytic Signal and VD1 images. When comparing the patterns with the geological map, a spatial correlation between geologic formations and the magnetic signatures is apparent (Figure 7-10). These groups of small wavelength anomalies obscure deeper-seated and broader magnetic anomalies, which become more apparent on the ternary images (e.g. Figure 5-9).

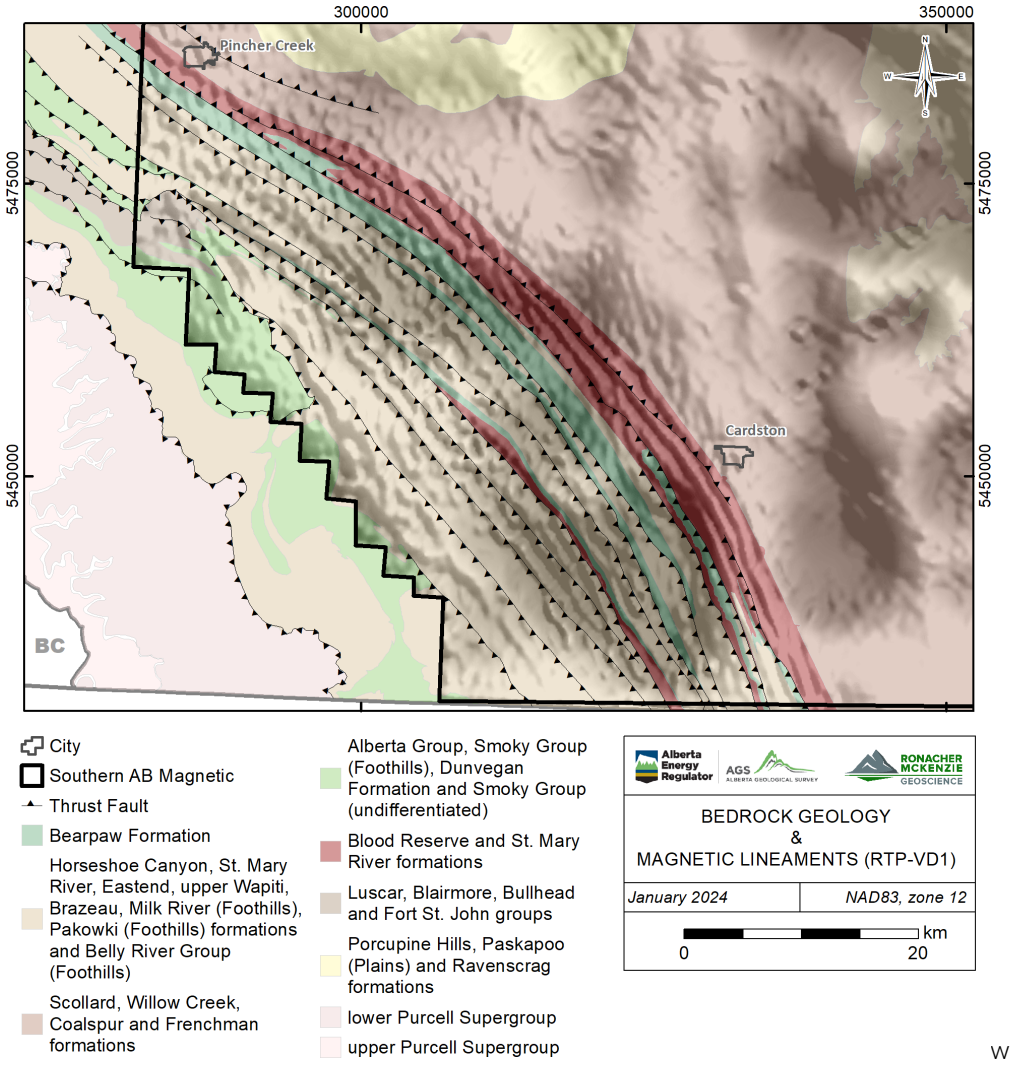

Figure 7-10. Aeromagnetic image of the foothills region overlain by the regional bedrock geology (Prior et al., 2013)

The foothills area comprises structurally emplaced Upper Cretaceous clastic sedimentary rocks that were deposited in non-marine, fluvial to shallow marine environments. The sedimentary layers are moderately to steeply dipping. The imaged magnetic response could be related either to the thrust faults or to stratigraphic boundaries. The latter is more likely, given the correlations observed in Figure 7-10.

These are important interpretations, because it establishes that stratigraphy and possibly faults in the WCSB can exert a control on magnetic data and its derived products. This in turn may help to support geological integration studies in select locations across the WCSB.

7.7 Lethbridge Lineaments: NW-SE Trending Short-Wavelength Anomalies

The presence of a series of linear, northwest-striking, short-wavelength anomalies, up to 30 km long, between the towns of Lethbridge and Milk River, herein termed the Lethbridge lineaments, has been systematically observed and documented (e.g. Ross et al., 1997). These distinct anomalies are also present in the current survey (Figure 7-11). Based on their short wavelength, these are expected to have a shallow point of origin within the sedimentary column; modeling by Ross et al., (1997) suggests about 250 m or less. These regional lineaments do not appear on satellite or LiDAR imagery.

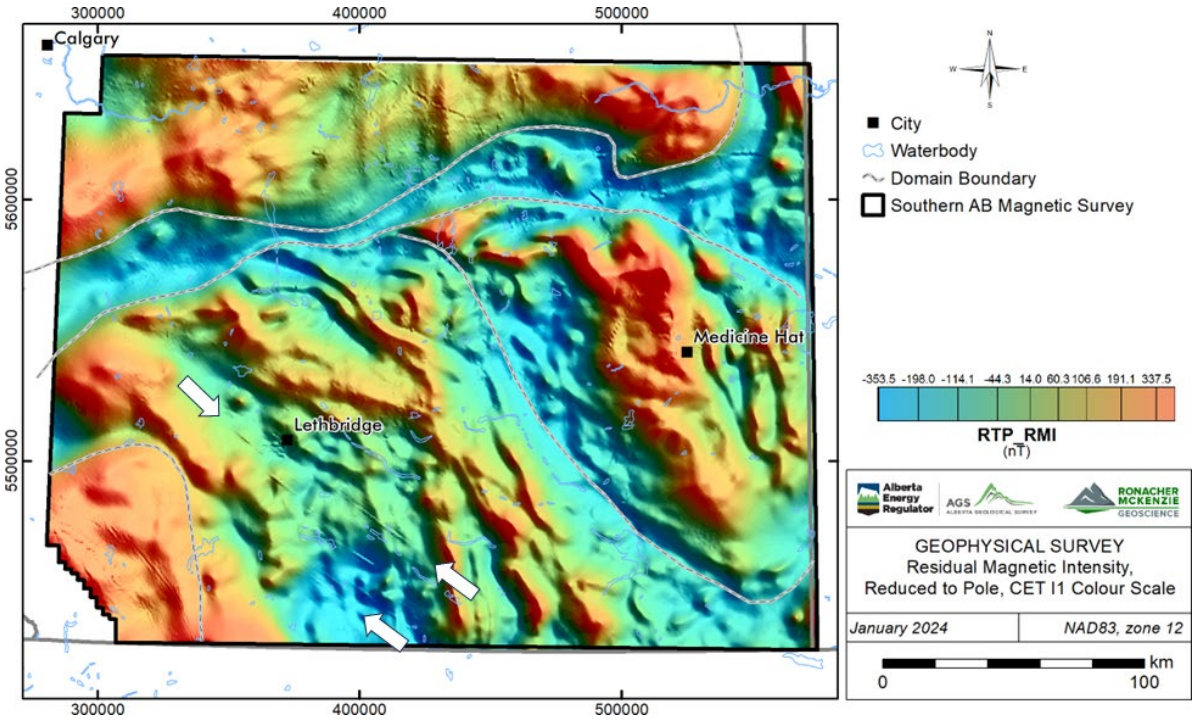

Figure 7-11. Regional extent of distinct NW-SE trending short-wavelength anomalies (white arrows).

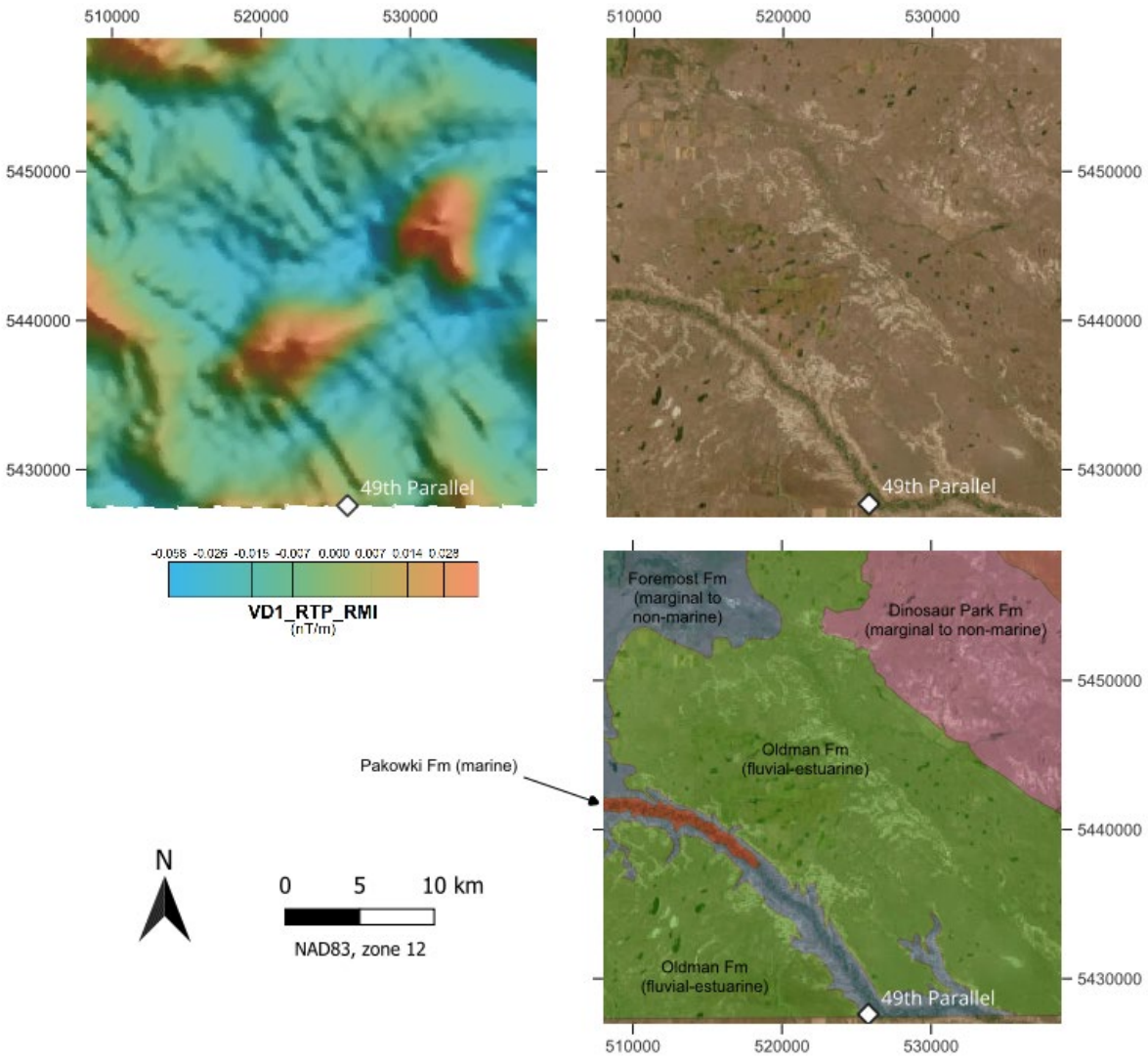

Figure 7-12. Small wavelength magnetic anomalies near the ENE-trending 49th parallel minette (top left). Integration with satellite image (top right; 1.2 m resolution World Imagery) and bedrock geology (bottom right; Prior et al, 2013) supports that the lineament is stratigraphic in nature.

The commonly accepted theory is that the Lethbridge lineaments represent Eocene dykes (Ross et al., 1997), but this has not yet been proven. The resolution of the new magnetic images allows for more small wavelength anomalies to be observed and integrated with geologic datasets. This study emphasizes that other geological hypotheses should also be considered:

- There is no magnetic expression associated with the Eocene intrusions (Section 7.3; Figure 7-6).
- There is no conclusive evidence for the presence of dykes in the well data (e.g. Ross et al., 1997).

- Some of the Palaeozoic faults spatially coincide with the Lethbridge lineaments (Section 7.4).
- Sub-parallel, short wavelength and laterally continuous magnetic anomalies also occur in the Foothills area (Section 7.6; Figure 7-10), where they are interpreted to be stratigraphic in nature.
- An extended (>10 km) short wavelength magnetic lineament in line with the Lethbridge lineaments is interpreted to be stratigraphic in nature (Figure 7-12).

In conclusion, several of the Lethbridge lineaments are stratigraphic or structural in nature. This may be important for CCS-opportunities, mineral exploration or geothermal exploitation in the region.

7.8 Petroleum Accumulations

In northern Alberta correlation between petroleum accumulations and basement lineaments has been established (Eaton et al., 1995; Lyatsky et al., 2005). In the Southern Plains, five stratigraphic levels with petroleum accumulations have been documented (Mossop and Shetsen, 1994), which include the Carboniferous Banff/Bakken and the Cretaceous Mannville plays. A first-pass evaluation between oil and gas field outlines, magnetic image (VD1) and lineament interpretation (GIS) show that about a dozen petroleum accumulations have a correlation in location and/or in shape (Figure 7-13). Of note is also the southern boundary of the Medicine Hat gas field in the Colorado Group (Chapter 20 in Mossop and Shetsen, 1994), which show a spatial correlation with NE-trending lineaments observed on magnetic images.

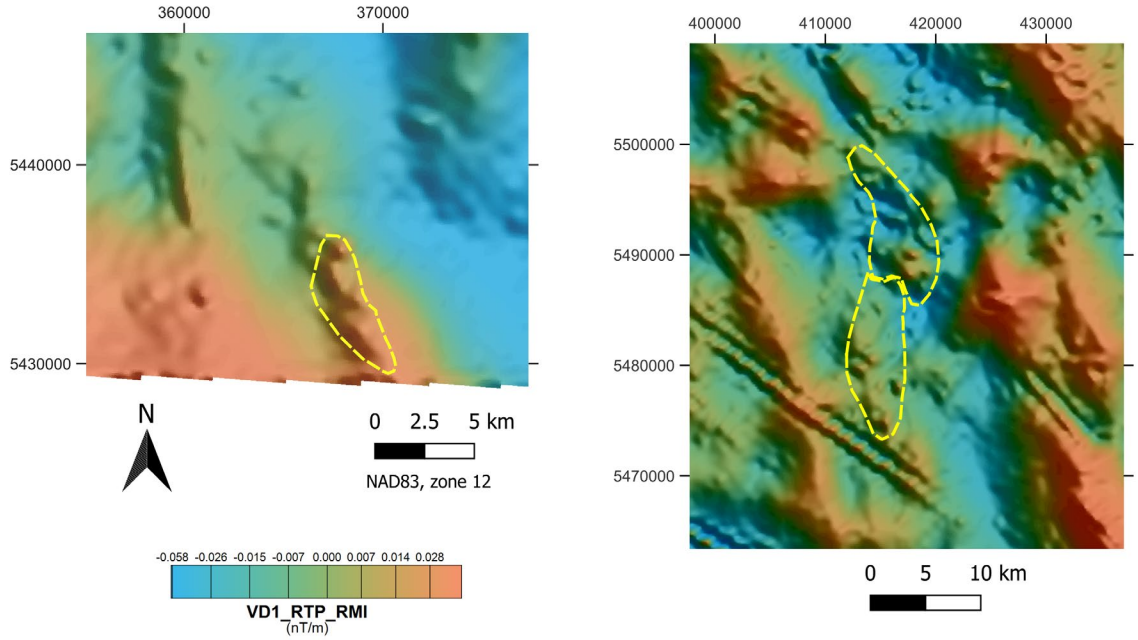

Figure 7-13. Correlation between magnetic anomalies and oil fields (yellow outlines; Mossop and Shetsen, 1994). Examples from Carboniferous Banff/Bakken (left), Cretaceous Lower Mannville (right).

Integration with local datasets, especially seismic images and well data can improve the correlation. Moreover, it can improve the depth ranges of magnetic lineaments, which in turn can benefit the regional interpretation of the aeromagnetic dataset and its products.

7.9 Helium

In recent years, regional interest in the exploration for and the development of helium sources has increased visibly. Helium is considered a critical resource for medical technology, high-tech manufacturing, space industry and national defense. In southern Alberta, the helium exploration industry is still developing.

Produced helium is labelled as 'grey' or 'green' (Hayes, 2023). Grey helium is co-produced with hydrocarbons, and is considered a by-product. Green helium is extracted from gas streams composed largely of inert gases, often in association with nitrogen, and is considered a primary target. Green helium is a product of the natural radioactive decay of heavy radioactive elements, such as thorium and uranium; elements that are common in felsic intrusive rocks, which in turn are commonly present in crystalline basement. Helium can both diffuse (vertically) through the subsurface or be transported in fluids via permeable networks.

A helium accumulation may not necessarily overlie a radioactive source. Geological models that describe the generation, migration and trapping of green helium follow a similar workflow as petroleum accumulations and require: (1) the presence of felsic plutons, (2) the presence of fracture and/or fault systems that serve as migration pathways, and (3) the extent of the Helium accumulation.

For southern Alberta, there are uncertainties on the presence of felsic intrusive bodies in the basement (Section 7.3) and brittle faults cannot be consistently interpreted on aeromagnetic images (Section 7.4). Therefore, establishing fluid pathways for Helium exploitation in this region using aeromagnetic data alone is unreliable and requires local integration with other subsurface datasets.

7.10 Astroblemes

Astroblemes are the (eroded) remnants of a meteorite impact crater. Two such unique structures have been confidently recognized: the Bow City and Eagle Butte structures (Prior et al., 2013).

The Late Cretaceous Bow City astrobleme (Glombick et al., 2014) is located 100 km southeast of Calgary. The structure is about 8 km in diameter with a semicircular uplifted central region. The structure does not have a surface expression, but it can be interpreted from LiDAR images. Some of the magnetic images show a circular anomaly that is spatially associated with the Bow City structure (Figure 7-14). This small but prominent feature may represent the central uprise of the Dinosaur Park Formation (Glombick et al., 2014).

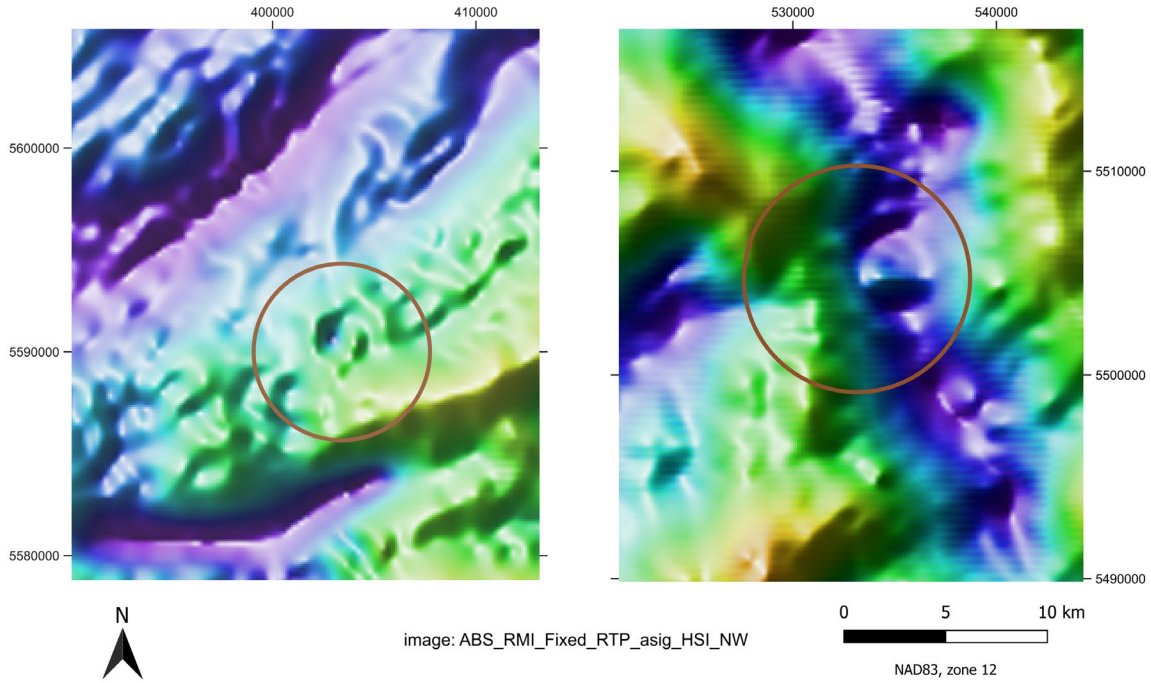

Figure 7-14. Spatial correlation between circular structures on magnetic images and astroblemes. Bow City (left) and Eagle Butte (right). Brown circles are astrobleme locations (Prior et al., 2013).

The latest Cretaceous Eagle Butte astrobleme (Sawatsky, 1976) is located ca. 40 km south of Medicine Hat. The circular structure does not have a distinct surface expression and does not show on LiDAR images. The structure is interpreted to be quite complex, characterized by many listric faults (Hanova et al., 2005). A faint circular magnetic signature of about 4 km diameter can be observed on several magnetic images (Figure 7-14). This feature is interpreted to be the Eagle Butte structure, supporting the conclusions by Ugalde et al., (2008), who observed a circular feature on the TMI-image of a legacy aeromagnetic survey.

Available seismic interpretations show that both impact structures are restricted to the upper half of the sedimentary layer and do not affect the basement (Hanova et al., 2005; Glombick et al., 2014). Correlation with both astroblemes shows that a magnetic signature, albeit weak, is present in the sedimentary section. This means that the 2022-2023 magnetic survey and its products can be quite helpful in delineating local features within the 'non-magnetic' sedimentary sequence.

7.11 Unknown Lineament

There is an intriguing magnetic trend across the center of the area that remains geologically unexplained. This NS trend is visible in the Matzhiwin high as a broad wavelength magnetic anomaly and several subsidiary lineaments at lower amplitude (Figure 7-15). These features are also picked up on a diverse array of structure

detection products. The anomaly is not observed in the Vulcan domain but does show, slightly offset to the west, in the MHB_central block as a magnetic high. This distinct trend can also be observed on aeromagnetic images in previous reports (McKenzie et al., 2021) and on select gravity products (first vertical derivative).

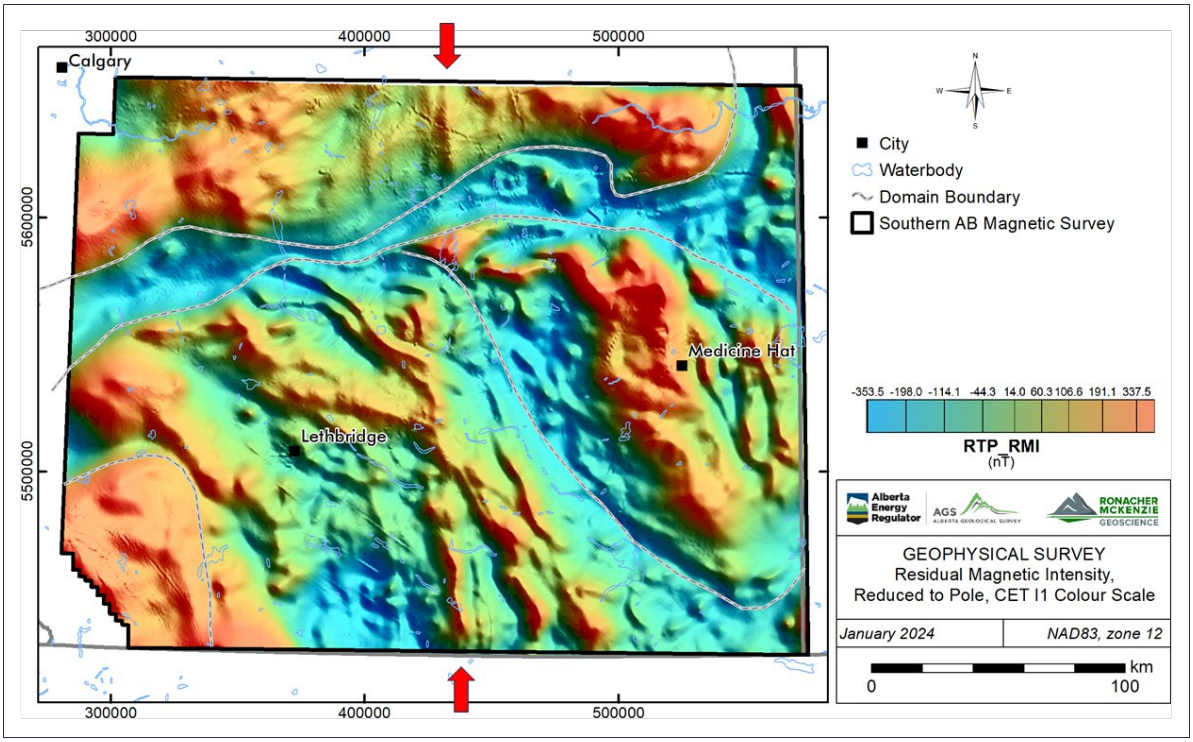

Figure 7-15. Central NS trending lineament.

This NS trend has not been annotated or interpreted before. In absence of additional control, a geological interpretation is speculative at best.

8.0 CONCLUSIONS

The magnetic images and the automatic structure and intrusion detection products derived from the 2022-2023 aeromagnetic survey provide new and detailed insights into the basement and its overlying sedimentary rocks in southern Alberta. Care was taken to recognise cultural artefacts (predominantly pipelines) during the interpretation stage.

The regional objectives (Section 2.1) were addressed by integrating our observations with public domain knowledge; the following conclusions can be made:

- Modifications to basement domains have been made, by editing the Vulcan domain boundary and by dividing the Medicine Hat block into three subdomains.
- The Southern Plains are underlain by an intricate 3D crustal architecture. Reduction of structural uncertainties and unravelling of its complex tectonic history requires continued integration with geological, well and seismic data.
- Faults in the basement and in the overburden are ambiguous in their appearance on magnetic images. Many published faults do not have distinct magnetic signatures. For the few faults that do show a spatial correlation, their responses on the magnetic images are equivocal.
- The Cordilleran fold-and-thrust belt contains a distinct small wavelength magnetic signature that can be correlated with its stratigraphy.
- The known Eocene intrusions do not carry a distinct magnetic signature.
- The regional presence of NW-SE trending small wavelength magnetic lineaments is persistent. These Lethbridge lineaments may not all be Eocene dykes as previously reported; some are demonstrated to be stratigraphic contacts or brittle faults.
- Diverse petroleum accumulations at different stratigraphic levels in southern Alberta have a spatial correlation with lineaments identified on the aeromagnetic images.
- The presence of intrusive bodies at depth is speculative at best, due to the lack of geological control on magnetic signatures. Coupled with the challenge of identifying brittle fault zones on magnetic images alone, integration with other geological datasets is needed to evaluate helium pathways.

9.0 REFERENCES

Alberta Geological Survey. 2023. "Alberta Aeromagnetic and Gravity Survey, Southern Alberta, Northern Alberta and Gap + Shield Surveys." (https://geology-ags-aer.opendata.arcgis.com/pages/aeromag-gravity-survey).

Atkinson, N. and Utting, D.J. 2021. "Glacial Flowlines of Alberta, Canada." Alberta Energy Regulator / Alberta Geological Survey, AER/AGS Map 622, scale 1:1,000,000. (https://ags.aer.ca/publication/map-622).

Burwash, R.A., Chacko, T., Muehlenbachs, K. and Bouzidi, Y. 2000. "Oxygen isotope systematics of the Precambrian basement of Alberta: implications for Paleoproterozoic and Phanerozoic tectonics in northwestern Alberta." Canadian Journal of Earth Sciences, vol. 37, p. 1611-1628.

Burwash, R.A., McGregor, C.R., Wilson, J.A., and O'Connell, S.C. 1994. "Chapter 5: Precambrian Basement." In *Geological Atlas of the Western Canada Sedimentary Basin*, by G.D. Mossop and I. Shetsen (comp.), p. 48-56. Canadian Society of Petroleum Geologists and Alberta Research Council. (https://ags.aer.ca/reports/atlas-western-canada-sedimentary-basin).

Eaton, D.W., Milkereit, B., Ross, G.M., Kanasewich, E.R., Geis, W., Edwards, D.J., Kelch, L. and Varsek, J. 1995. "Lithoprobe basin-scale profiling in central Alberta: influence of basement on the sedimentary cover." Bulletin of Canadian Petroleum Geology, v. 43, p. 65-77.

Eaton, D.W., Ross, G.M. and Clowes, R.M. 1999. "Seismic-reflection and potential-field studies of the Vulcan structure, western Canada: a Paleoproterozoic Pyrenees?" Journal of Geophysical Research, v. 104, no. B10, p. 23,255-23,269.

Glombick, P., Schmitt, D.R., Xie, W., Bown, T., Hathwawy, B, and Banks, C. 2014. "The Bow City structure, southern Alberta, Canada: The deep roots of a complex impact structure?" Meteoritics & Planetary Science, vol. 49, Issue 5, p. 872–895.

Hanova, J., Lawton, D.C., Visser, J., Hildebrand, A.R., and Ferriere, L. 2005. "3D structural interpretation of the Eagle Butte impact structure, Alberta, Canada." Paper presented at 36th Annual Lunar and Planetary Science Conference, 2 pages.

Hayes, B. 2023. "Helium in Alberta – Bringing a Critical Commodity On Stream." Abstract for the Geoconvention, Calgary Canada, May 15-17, 2023, 5 pages.

Hoffmann, P.F. 1988. "United plates of America, the birth of a craton, Early Proterozoic assembly and growth of Laurentia." Annual Review of Earth and Planetary Science Letters, v. 16, p. 543–603.

Hope, J., Eaton, D.W., and Ross, G.M. 1999. "Lithoprobe seismic transect of the Alberta Basin: Compilation and overview." Bulletin of Canadian Petroleum Geology, v. 47, no. 4, p. 331-345.

Isles, D. J., and L. R. Rankin. 2013. *Geological interpretation of aeromagnetic data.* Australian Society of Exploration Geophysicists, 365 pages.

Kovesi, P. 2015. *Good Colour Maps: How to Design Them.* Accompanying Document, Crawley, Western Australia: Centre for Exploration Targeting, The University of Western Australia. (https://colorcet.com/).

Lemieux, S. 1999. "Seismic reflection expression and tectonic significance of Late Cretaceous extensional faulting of the Western Canada Sedimentary Basin in southern Alberta." Bulletin of Canadian Petroleum Geology, v. 47, no. 4, p. 375-390.

Lemieux, S., Ross, G.M., and Cook, F.A. 2000. "Crustal geometry and tectonic evolution of the Archean crystalline basement beneath the southern Alberta Plains, from new seismic reflection and potential-field studies." Canadian Journal of Earth Sciences, v. 37, p. 1473-1491.

Lopez, G., McGill, D. and McKenzie, J. 2024. "Geological Interpretation of the 2021 Aeromagnetic Data - Canadian Shield, Alberta." Prepared For the Alberta Geological Survey, 113 pages.

Lopez, G., McGill, D., Brem, A., and McKenzie, J. in progress. "Geological Interpretation of the 2022-2023 Aeromagnetic Data - Northern Alberta, Canada."

Lyatsky, H.V., Pană, D.I., and Grobe, M. 2005. "Basement structure in central and southern Alberta; insights from gravity and magnetic maps." Alberta Energies and Utilities Board/Alberta Geological Survey, Special Report 72, 83 pages. (https://ags.aer.ca/publication/spe-072).

McKenzie, J., Ronacher, E., and Farahani, F. 2021. "Interpretation of Geophysical Data, Alberta Geological Survey: He and Li project." 36 pages. (https://ags.aer.ca/publication/dig-2021-0020).

Mossop, G.D. and Shetsen, I. 1994. "Geological Atlas of the Western Canada Sedimentary Basin." *Alberta Geological Survey.* Canadian Society of Petroleum Geologists and Alberta Research Council. Accessed October 30, 2023. (https://ags.aer.ca/reports/atlas-western-canada-sedimentary-basin).

Nieuwenhuis, G., Unsworth, M.J., Pană, D.I., Craven, J., and Bertrand, E. 2014. "Three-dimensional resistivity structure of Southern Alberta, Canada: implications for Precambrian tectonics." Geophysical Journal International, v. 197, p. 838-859.

Pană, D.I., and Elgr, R. 2013. "Geology of the Alberta Rocky Mountains and Foothills." Energy Resources Conservation Board/Alberta Geological Survey, ERCB/AGS, Map 560, scale 1:500,000. (https://ags.aer.ca/publication/map-560).

Pană, D.I., Elgr, R., Waters, E.J.,Warren, J.A., Lopez, G.P., and Pawlowicz, J.G. 2021. "Structural elements in the Alberta Plains." Alberta Energy Regulator/Alberta Geological Survey, AER/AGS Open File Report 2021-01, 33 pages. (https://ags.aer.ca/publication/ofr-2021-01).

Pilkington, M., Miles, W.F., Ross, G.M. and Roest, W.R. 2000. "Potential-field signatures of buried Precambrian basement in the Western Canada Sedimentary Basin." Canadian Journal of Earth Sciences, v. 37, p. 1453-1471.

Prior, G.J., Hathaway, B., Glombick, P., Pană, D.I., Banks, C.J., Hay, D.C., Schneider, C.L., Grobe, M., Elgr, R., and Weiss, J.A. 2013. "Bedrock geology of Alberta." Alberta Energy Regulator / Alberta Geological Survey, AER/AGS Map 600, scale 1:1,000,000. (https://ags.aer.ca/publication/dig-2013-0018).

Ross, G.M., Broome, J., and Miles, W. 1994. "Chapter 4: Potential fields and basement structure." In *Geological Atlas of the Western Canada Sedimentary Basin*, by G.D. Mossop and I. Shetsen (comp.), p. 41–47. Canadian Society of Petroleum Geologists and Alberta Research Council. (https://ags.aer.ca/reports/atlas-western-canada-sedimentary-basin).

Ross, G.M., Mariano, J., Dumont, R., Kjarsgaard, B.A., and Teskey, D. 1997. "Was Eocene magmatism widespread in the subsurface of southern Alberta? Evidence from new aeromagnetic anomaly data." Geological Survey of Canada, Bulletin 500, p. 235-247.

Ross, G.M., Villeneuve, M.E., Parrish, R.R., and Bowring, S.A. 1989. "Tectonic Subdivision and U/Pb geochronology of the Precambrian basement of the Alberta Basin, Western Canada." Geological Survey of Canada, Open File 2103. Map 1:1 000 000. Scanned reproduction of the original map. (https://doi.org/10.4095/130739).

Rukhlov, A.S. and Pawlowicz, J.G. 2012. "Eocene potassic magmatism of the Milk River Area, southern Alberta (NTS 72E) and Sweet Grass Hills, northern Montana: overview and new data on mineralogy geochemistry, petrology and economic potential." Energy Resources Conservation Board/AGS Open File Report 2012-01, 88 pages. (https://ags.aer.ca/publication/ofr-2012-01).

Sawaktzky, H. 1976. "Two probable Late Cretaceous astroblemes in western Canada - Eagle Butte, Alberta and Dumas, Saskatchewan." Geophysics, v. 41, p. 1261 - 1271.

Schultz, R., Mei, S., Pană, D.I., Stern, V., Gu, Y.J., Kim, A. and Eaton, D. 2015. "The Cardston Earthquake Swarm and Hydraulic Fracturing of the Exshaw Formation (Alberta Bakken Play)." Bulletin of the Seismological Society of America, v. 105, no. 6, p. 2871-2884.

Ugalde, H.A., Underhay, S.L., Morris, W.A. and Markham, K. 2008. "Evidence for Basement Fault Reactivation in Southern Alberta: An Integrated Topography and Airborne Magnetics Approach." CSEG Recorder, January 2008 p. 32-38.

Villeneuve, M.E., Ross, G.M., Thériault, R.J., Miles, W., Parrish, R.R., and Broome, J. 1993. "Tectonic subdivision and U-Pb geochronology of the crystalline basement of the Alberta Basin, western Canada." Geological Survey of Canada Bulletin 447, 95 pages.

Warren, M.J. and Cooper, M. 2017. "Deformation history in the southern Alberta foreland basin and petroleum system implications." Abstract for the Geoconvention, Calgary Canada, May 15-19, 2017, 1 page.

Wright, G.N., McMechan, M.E., Potter, D.E.G., and Holter, M.E. 1994. "Chapter 3: Structure and Architecture." In *Geological Atlas of the Western Canada Sedimentary Basin*, by (comp.) G.D. Mossop and I. Shetsen, p. 25-40. Canadian Society of Petroleum Geologists and Alberta Research Council. (https://ags.aer.ca/reports/atlas-western-canada-sedimentary-basin).

Appendix 1 – Top Precambrian basement from well data

Surface Location	Longitude	Latitude	ID	KB (m asl)	TD (m)	sMV (m)	Top Pcb (m)	Top Pcb (m asl)
01-31-013-20W4	-112.716	50.124	1	896	2564	1234	2535	-1639
12-14-012-12W4	-111.547	49.999	2	758	2128	916	2113	-1355
05-01-017-14W4	-111.811	50.403	3	752	2219	1013	2217	-1465
16-29-001-11W4	-111.433	49.068	4	983	1819	765	1813	-830
12-19-014-04W4	-110.550	50.188	5	740	-	-	-	-
04-12-015-27W4	-113.594	50.239	6	1011	3608	2170	3594	-2583
10-04-019-11W4	-111.467	50.581	7	773	2210	1006	-	-
11-18-024-15W4	-112.089	51.047	8	752	2433	1085	2425	-1673
12-32-001-04W4	-110.514	49.082	-	914	2147	975	2139	-1224
10-07-001-08W4	-111.059	49.022	-	1083	2021	902	1944	-861
06-04-001-12W4	-111.555	49.005	-	1159	-	-	1818	-659
16-35-001-22W4	-112.837	49.086	-	1248	2900	1503	2643	-1396
03-18-002-01W4	-110.132	49.119	-	888	2268	1071	2252	-1364
06-18-002-12W4	-111.602	49.118	-	926	1843	757	1831	-905
05-16-002-22W4	-112.895	49.120	-	1319	2865	1696	2841	-1522
07-17-003-08W4	-111.045	49.208	-	913	2035	863	2014	-1101
07-26-003-14W4	-111.785	49.237	-	939	1929	796	1920	-981
14-05-004-21W4	-112.798	49.275	-	1194	2555	1348	2518	-1324
04-13-006-03W4	-110.294	49.467	-	1110	2501	1248	2494	-1384
05-18-007-23W4	-113.111	49.557	-	1016	3119	1828	3107	-2090
02-07-008-22W4	-112.967	49.627	-	949	2739	1480	2736	-1787
08-25-012-24W4	-113.147	50.024	-	959	3003	1675	2993	-2035
12-12-015-07W4	-110.849	50.246	-	717	2152	903	2124	-1407
11-13-015-09W4	-111.119	50.262	-	757	2186	947	2168	-1412
11-20-016-04W4	-110.522	50.363	-	754	2176	889	2175	-1422
11-20-016-07W4	-110.934	50.364	-	775	2208	988	2202	-1427
06-30-018-08W4	-111.097	50.550	-	800	2266	1016	2246	-1447
06-36-019-01W4	-110.020	50.650	-	747	2231	902	2213	-1466
07-11-019-05W4	-110.590	50.592	-	661	-	-	2116	-1455

Surface Location	Longitude	Latitude	ID	KB (m asl)	TD (m)	sMV (m)	Top Pcb (m)	Top Pcb (m asl)
06-30-019-07W4	-110.966	50.637	-	807	2269	1033	2255	-1448
08-17-020-04W4	-110.514	50.694	-	740	2205	966	2193	-1453
05-11-020-06W4	-110.737	50.679	-	793	2231	1049	2218	-1425
08-08-020-09W4	-111.209	50.680	-	776	2210	1003	2188	-1412
n/a	-109.834	50.559	-	768	2268	944	2262	-1493

Location of wells with Top Precambrian penetrations in southern Alberta (Figure 4-3). The ID refers to the wells that have a lithological and geochronological control (Table 4-1; Ross et al., 1989; Villeneuve et al., 1993).

Abbreviations: KB = Kelly Bushing; m asl = elevation Above Sea Level; TD = Total Depth of well; sMV = sub-Mannville unconformity; Top Pcb = Top Precambrian.

Source: https://ags.aer.ca/atlas-the-western-canada-sedimentary-basin/atlas-well-control-data; accessed November 2023 (Mossop and Shetsen, 1994).

Appendix 2 – Automatic detection - Fathom Geophysics Report

Processing of magnetic data over the Alberta South project area, Canada for Ronacher McKenzie Geoscience

January 2024

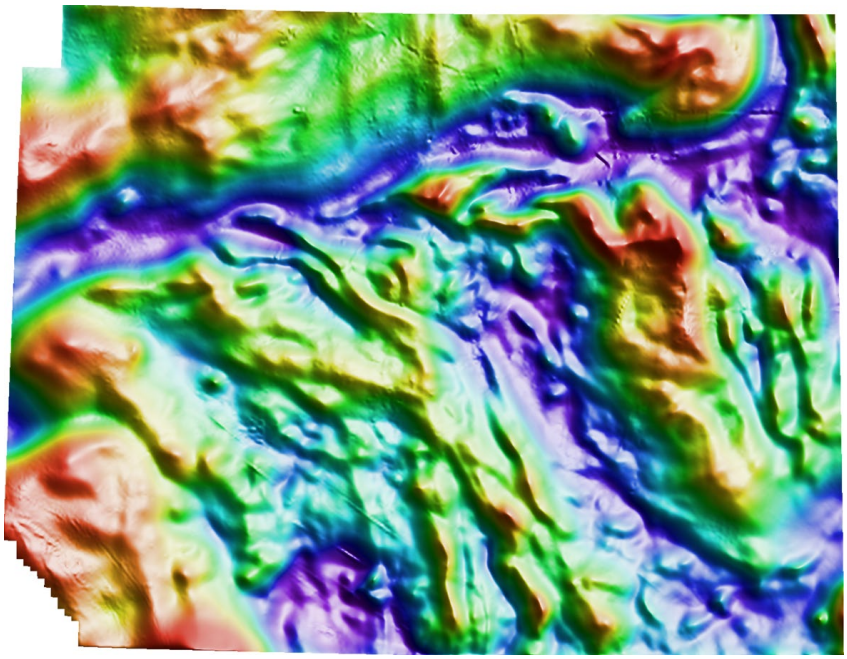

by Dan Core†, Eric Core, and Lisa Lombardi
Fathom Geophysics

†Corresponding author: dan@fathomgeophysics.com

Introduction

The project area for this work is the Alberta South magnetic survey from the Alberta Geological Survey (AGS) (**Figure 1**). The goal of this work is to process the magnetic data to generate products that can assist with interpretation of structure and lithology based on the magnetic data.

The magnetic data are from a survey flown between 20 October 2022 and 4 March 2023 by EON Geosciences Inc on behalf of the Alberta Energy Regulator. Gridded data provided with the survey were good quality and were supplied to us with coordinates in WGS84 UTM Zone 12N (**Figure 2**)**.** All outputs of our work use this coordinate system. Survey data have 800m line-spacing. All gridded products use a cell size of 200m.

The processing completed includes application of a suite of standard filters and depth-to-magnetic source processing as well as application of Fathom Geophysics' structure detection and radial symmetry filters.

Processing summary

Reduction to the pole (RTP)

RTP processing produces a magnetic field that is equivalent to what would be generated if the data were collected at the magnetic north pole. This shifts magnetic highs to be directly over their sources and creates symmetric anomalies over the top of symmetric magnetic sources. The RTP filter for these data uses an inclination of 72.6° and a declination of 12.6° (**Figure 3**).

Note that in general RTP processing is not valid for remanent bodies unless the remanence is directly opposed to the present-day field. The dataset almost certainly contains some remanent bodies that will not be corrected properly using the RTP filter. However, it is worthwhile applying the filter because most of the anomalies in the area are normally magnetized or reversely magnetized with relatively few anomalies possessing an apparent magnetization direction at a high angle to the present-day field.

Magnetic standard filtering

The RTP grid was filtered with a suite of standard geophysical filters including the analytic signal and vertical derivative. These grids were imaged using our in-house software to produce shaded images with the sunlight coming from the northeast or northwest (NE or NW in the filename). Unshaded images were also produced so that the geographic location of pertinent features in the data can be readily defined (because shaded images can 'fool the eye' in this respect).

Processing summary — Magnetic data

Magnetic standard filtering (continued)

Figures 4 to 22 show images of most of the standard filtering results supplied. Standard filtering results have been included in this report because of their capacity to help the reader who might be new to the delivered processing results files to quickly grasp the project area's overall magnetic susceptibility changes/contrasts.

Magnetic total structure detection

Structure detection was applied to highlight edges in the RTP magnetic data and the AGC of the RTP data. Edges in potential field data are locales that are more likely to be faults, contacts or other structures. The structure detection algorithm and processing are described in more detail in **Appendix 1**.

Representative images of the total structure detection filtering are shown in **Figures 23 and 24** for the RTP data and **Figures 25 and 26** for the AGC of the RTP. Further results files were delivered in addition to those visualized within this report, and we urge the reader to explore the entire series of results files to ensure full familiarity with the results of total structure detection processing and their possible exploration ramifications.

Total-structure detection filtering was applied to the RTP grid at minimum wavelengths of 500m, 1000m, 2000m, 4000m, and 8000m. The RTP-derived total-structure detection results are good at depicting relatively long-wavelength features. Structure intersection images were supplied alongside structure images.

This filtering was also applied to the AGC grid at minimum wavelengths of 500m, 1000m, 2000m, 4000m, and 8000m. The AGC-derived total-structure detection results are good at depicting relatively detailed features as well as highlighting features in quiet parts of the dataset. Structure intersection images were supplied alongside structure images.

The RTP shows large-scale ENE-trending features in the northern part of the dataset. South of a large ENE-trending feature, the orientations change and are dominated by NW to NNW-trending features. Some NS-trending features appear to cut across both trends.

The AGC results show similar results to the RTP overall. However, they do a better job of highlighting detailed features. The AGC results are also good for seeing different structural domains, particularly in the southern part of the project area.

Processing summary — Magnetic data (continued)

Magnetic total structure detection (continued)

The intersection maps show where structures of different orientations are collocated. Areas with a high density of intersections are likely to be more structurally complex and therefore may be more likely to host mineralization.

Magnetic belt-parallel and belt-crossing structure detection

In many heavily deformed belts, the fabric-parallel and fabric-crossing structures can be different structure types and may have different timing. The fabric-parallel features tend to be contacts or belt-parallel shear zones. The cross structures are usually not contacts and are more likely to be faults. Any sense of motion is possible on the cross structures. If clear lateral offset of the units is present, the faults are likely strike-slip faults. Normal and reverse faults are often represented by a change in amplitude or frequency content of the magnetic data.

The first step in extracting fabric-parallel and fabric-crossing structures is to extract the fabric orientation. The RTP data is very smooth making it difficult to determine the orientations of individual units. Therefore, the AGC was used for determining the fabric orientation. (**Figure 27**). The results are dominated by NW to NNW-trending features in the southern part of the project area. The north has ENE-trending features as well as features with NE to NNE trends.

Representative images of the results of parallel and cross structure detection are shown in **Figures 28 and 29** for the RTP data and **Figures 30 and 31** for the AGC of the RTP data. The wavelengths that were run are the same as for the total structure except that no 8000m scale was run for either the RTP or AGC data. The structure results at that scale lack a strong fabric. At longer wavelengths, the original fabric orientation maps are smoothed so that larger-scale structures do not get broken up by rapid changes in the fabric orientation.

The fabric-parallel structures should be useful for highlighting lithological contacts and fabric parallel shear zones. The AGC results appear to be useful for highlighting lithological boundaries. The fabric-crossing structures are likely to be faults. The RTP results are likely more useful for cross structures because there is a lower density of features meaning that the features that are present are more likely to be significant.

Further results files were delivered in addition to those visualized within this report, and we urge the reader to explore the entire series of results files to ensure full familiarity with the results of belt-parallel and belt-crossing structure detection processing and their possible exploration ramifications.

Processing summary — Magnetic data (continued)

Magnetic radial symmetry

The radial symmetry detection filter can highlight discrete, equant magnetic features with different radii. These features indicates areas that are more likely to host intrusive rocks or discrete alteration zones. Radial symmetry detection was completed on the RTP magnetic data. The radial symmetry algorithm is described in greater detail in **Appendix 2** of this report.

Representative images of the radial symmetry results are shown in **Figures 32**. Further results files were delivered in addition to those visualized within this report, and we urge the reader to explore the entire series of results files to ensure full familiarity with the results of radial symmetry analysis processing and their possible exploration ramifications.

Radial symmetry detection processing was applied to the RTP grid in magnitude-independent mode at minimum-radius runs of 2000m, 4000m, and 8000m. Radii smaller and larger than these did not appear to be useful on this dataset. Both magnetic highs and magnetic lows represent meaningful/useable results and therefore are presented in images.

Note that in order to obtain optimal results it was necessary to take a residual (i.e., carry out differential upward continuation) prior to running radial symmetry detection at a given minimum radius. It was found that a residual involving levels going from on quarter the minimum radius to four times the minimum radius enable the production of satisfactory radial symmetry detection results (e.g., for the 2000m radial symmetry detection run, a 500m-8000m residual was carried out first).

The results in **Figure 32** show that the central part of the area has a relatively low density of round features when compared to the edges of the dataset. The entire project area has significant cover over it making it impossible to highlight detailed radially symmetric features. Only large-scale features have been highlighted. Given the cover, some structural features such as domes or thickened areas can have the same appearance as an intrusive rock.

Reversely magnetized bodies will be highlighted as radially symmetric lows in this analysis. Any lows that correspond with highs in the analytic signal are likely to be reversely magnetized.

Processing summary — Magnetic data (continued)

Depth to magnetic source

Many algorithms can be used to estimate the depth to magnetic sources. Most are based on at least second order derivatives making them significantly influenced by any kind of noise in the data.

This dataset presents some significant challenges for these algorithms due to high frequency noise that occurs where cultural features are present in the data. These features are mostly due to oil and gas infrastructure in the area. While the airborne contractor took steps to mitigate the noise caused by these features, the effects were not completely removed.

To limit the impact of near-surface noise, a 2000-6000m residual was taken prior to the depth to source processing. This should focus the processing on sources with a depth from 1000-3000m, which is roughly the expected basement depth range in the area.

The method that was used for the depth to source is that of Cooper (2014). It involves looking at the derivative of the tilt angle to estimate the depth of contacts in the dataset. The resulting depths were then interpolated to generate a continuous distance to magnetic source grid. The average altitude of the aircraft was subtracted off to generate a depth to magnetic basement grid.

The results of the depth to magnetic source processing are shown in **Figure 33**. The smoother parts of the dataset show greater depth to source as is expected. The western and northern parts of the project area have greater depth to the magnetic basement than the rest of the area.

The average depths observed in the depth to source processing are similar to those observed in wells that have pierced the basement in parts of the area. However, there isn't a particularly good correlation between the magnetic processing results and the measured depths. This could be due to the presence of non-magnetic basement in some areas. Some issues may also be caused by high frequency artifacts in the dataset that were not completely removed by the prefiltering.

The depth to magnetic source grid was subtracted from the topography data to generate a top of magnetic basement surface (**Figure 34**)**.** The magnetic basement surface shows less variation than the depth to magnetic source. The main cause of this is the higher elevation observed in the western part of the project area.

**Cooper (2014) The automatic determination of the location, depth, and dip of contacts from aeromagnetic data. Geophysics, v79, pp J35-J41. https://library.seg.org/doi/10.1190/geo2013-0181.1*

File formats and image types delivered

The grids for this work have been delivered in ER Mapper ERS format. All images have been provided in GeoTIFF format with associated MapInfo TAB files and ESRI world files. Vectors have been delivered in ESRI shapefile format.

Structure detection results have been supplied as grids, images (GeoTIFF), and polylines (vectorization of the gridded results). The polylines have been attributed with the values from the structure detection grid and the orientation of the structure calculated based on the vectorized result.

Structure images were made in an unshaded fashion using a warm color bar (yellows through to reds) and a linear color stretch. Shaded structure images cycle through colors starting from purple and blue (lows) through to reds (highs) and were made with a histogram-equalized color stretch. Dominant orientation images use a wraparound colorbar palette that produces the same color for 0 and 180 with a rainbow distribution for colors in between. Those orientation images that have been thresholded display only significant features and are white in locales that essentially lack structure.

Radial symmetry ‘lows and highs’ images were made using a blue-and-red color bar possessing no intermediate colors. Highs-only images use the red side of that same color bar, and lows-only images use the blue side.

Several ternary images were also created for this work. These images are generated using three separate grids to represent the red-green-blue (RGB) or cyan-magenta-yellow (CMY) channels of the output image. RGB ternary images involve color addition, analogous to how different-colored light beams combine on a performance stage. When all three channels are present in full strength, pure white is the result. (Pure black indicates all three channels are absent.) CMY ternary images involve color subtraction, similar to colors resulting from the mixing of paint pigments. When all three channels are present in full strength, pure black is the result. (Pure white indicates all three channels are absent.) **Figure 17** explains in more detail how to interpret the full gamut of colors that can turn up in ternary images.

See also the list of abbreviations and acronyms supplied in this report to help decode the information contained within a given grid/image filename.

List of acronyms and abbreviations

ABS	Alberta South project area (appears in delivered file names)
agc	automatic gain control (appears in delivered file names)
agc30	AGC when standard deviation=30 (in file names)
asig	analytic signal (appears in delivered file names)
colorbar	numerical values associated with image's color range (in file names)
Cross	structures that are perpendicular or oblique to the magnetic stratigraphic fabric
CMY	cyan-magenta-yellow ternary (appears in delivered file names)
hgm	horizontal gradient magnitude (appears in delivered file names)
Highs	positive anomalies-only radial symmetry image (in file names)
HSI	hue, saturation and intensity (appears in delivered file names)
HTh	hysteresis thresholding was used during vectorization (in file names)
Int	structural intersections image (appears in delivered file names)
LgeRes	large-scale residual (appears in delivered file names)
lin	linear-stretch image (appears in delivered file names)
Lows	negative anomalies-only radial symmetry image (in file names)
LowsAndHighs	negative and positive anomalies radial symmetry image (in file names)
md	magnitude dependent radial symmetry result (in file names)
MedRes	medium-scale residual (appears in delivered file names)
Mi	magnitude independent radial symmetry result (in file names)
OriDom	dominant orientation image (appears in delivered file names)
Para	Structures that are parallel to the magnetic stratigraphic fabric
Pgrav	pseudogravity (appears in delivered file names)
PgravRes	residual of pseudogravity (appears in delivered file names)
PgravResHGM	HGM of residual of pseudogravity (appears in delivered file names)
res	residual (appears in delivered file names)
res25_100	25m-100m residual (appears in delivered file names)
RGB	red-green-blue ternary (appears in delivered file names)
RMI	residual magnetic intensity (appears in delivered file names)
RSym	radial symmetry image (appears in delivered file names)
RSym100	100m minimum radius radial symmetry image (in file names)
RTP	reduced-to-pole (appears in delivered file names)
SmRes	small-scale residual (appears in delivered file names)
Struct	structure image (appears in delivered file names)
Struct100	100m minimum wavelength structure image (in file names)
tern, ternary	ternary image (appears in delivered file names)
Thresh, thr, Th	image made via thresholding (appears in delivered file names)
tilt	tilt angle (appears in delivered file names)
TMI	total magnetic intensity (appears in delivered file names)
Total	total structure image (appears in delivered file names)
vd	vertical derivative (a.k.a. 1VD) (appears in delivered file names)

List of acronyms and abbreviations (continued)

vdmhgm	vertical derivative minus HGM (appears in delivered file names)
Vec	vectorized results file (appears in delivered file names)
vias	analytic signal of vertical integral (appears in delivered file names)
vint	vertical integral (appears in delivered file names)
X	directional derivative along X axis (appears in delivered file names)
Y	directional derivative along Y axis (appears in delivered file names)
Z	directional derivative along Z axis (i.e., vertical derivative) (in file names)

Project location map

Figure 1: Location map for this project showing the boundary of the survey area as a red outline.

Magnetic data-processing results images
▶ Residual magnetic intensity (RMI)

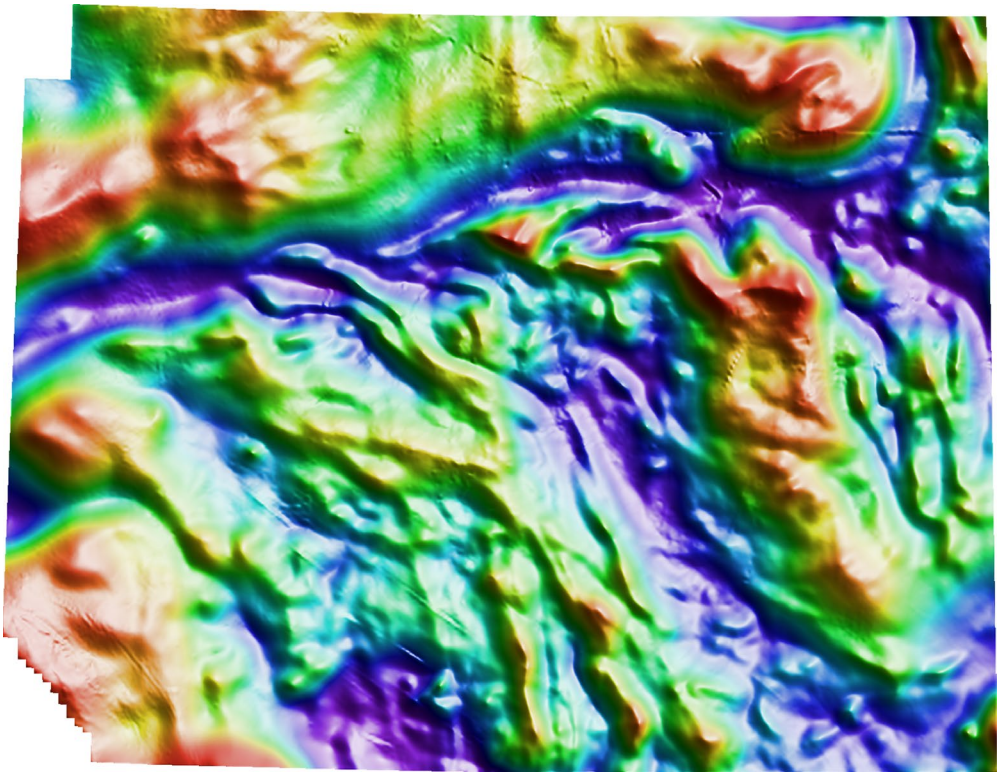

ABS_RMI_Fixed_HSI_NE

Figure 2: Residual magnetic intensity data for the project area. The indicative colorbar shown applies to all magnetic data-processing results images involving the HSI (hue, saturation, intensity) color display system.

Magnetic data-processing results images
▶ Reduction-to-pole (RTP)

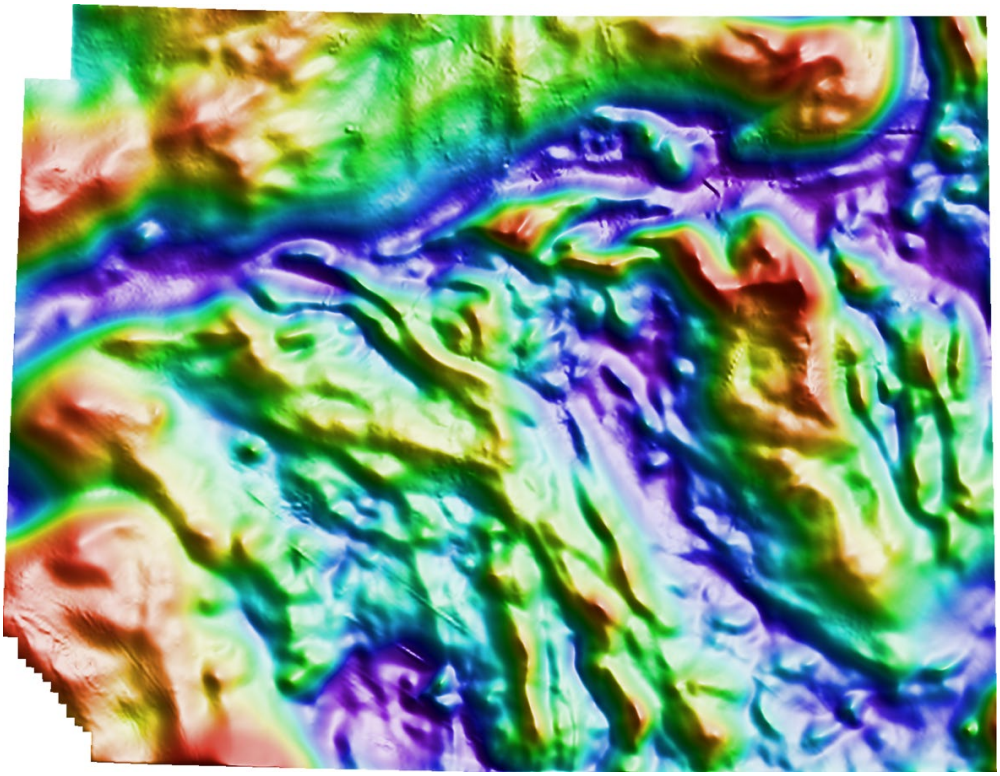

ABS_RMI_Fixed_RTP_HSI_NE

Figure 3: Reduced-to-the-pole magnetic data for the project area. The RTP filter attempts to produce the magnetic field that would be expected if the data were collected at the magnetic pole.

Magnetic data-processing results images (continued)
▶ Standard filtering — First vertical derivative

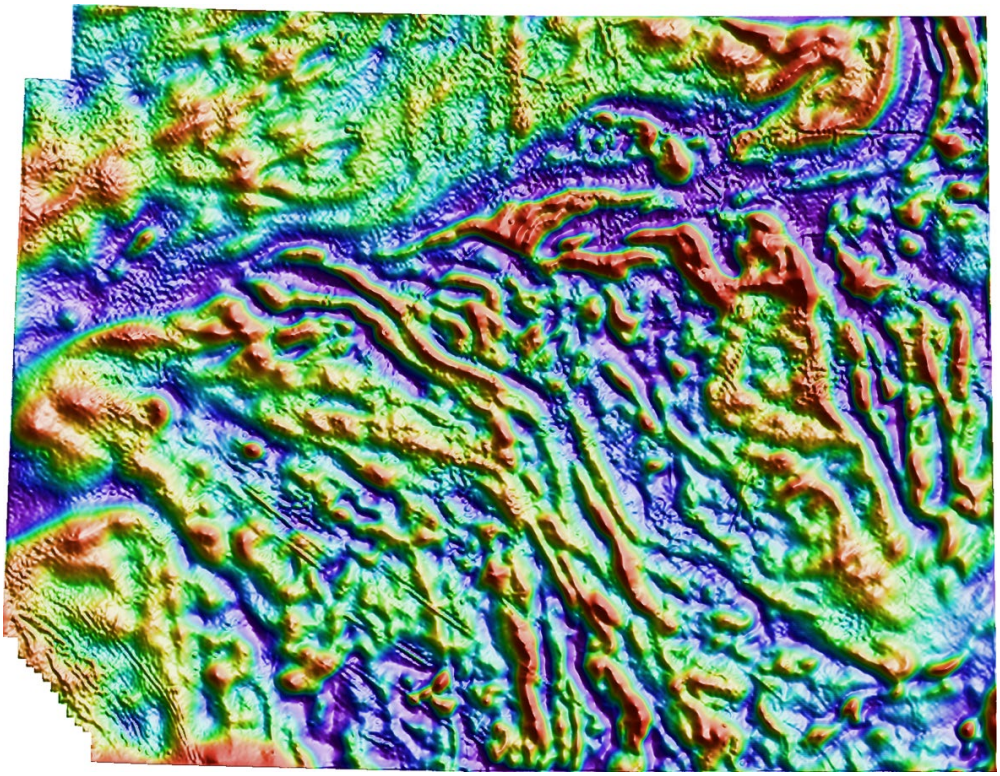

ABS_RMI_Fixed_RTP_vd_HSI_NE

Figure 4: The first vertical derivative (1VD) transform is the rate of change of the potential field in the vertical direction. Application of this filter has the effect of accentuating the shorter wavelength (higher frequency) components at the expense of longer wavelength (more regional) features.

Magnetic data-processing results images (continued)
▶ Standard filtering — Horizontal gradient magnitude

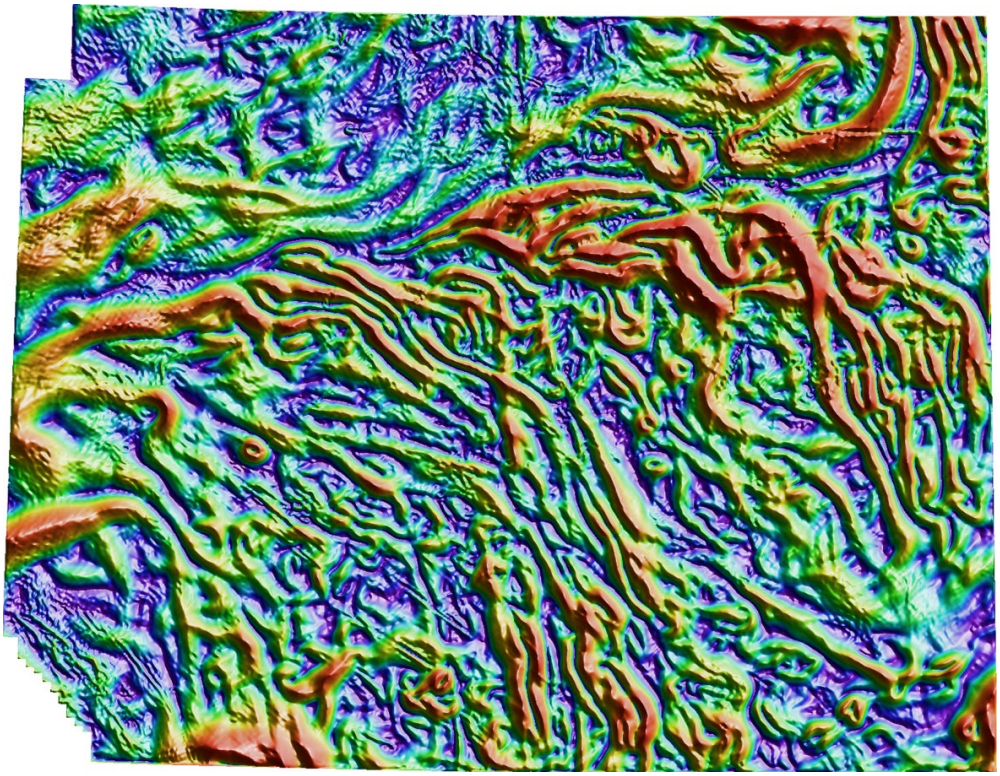

ABS_RMI_Fixed_RTP_hgm_HSI_NE

Figure 5: The horizontal gradient magnitude is calculated from the x- and y-derivatives of the data ($\sqrt{dx^2 + dy^2}$). This filter highlights the location of steep gradients in the data. Peaks in the HGM should occur at susceptibility contrasts in magnetic data and density contrasts in gravity data. These are likely to be locations of faults or contacts. Peaks will be offset in the down-dip direction for dipping bodies. The results are affected by remanent magnetization.

Magnetic data-processing results images (continued)
▶ Standard filtering — Vertical derivative minus HGM

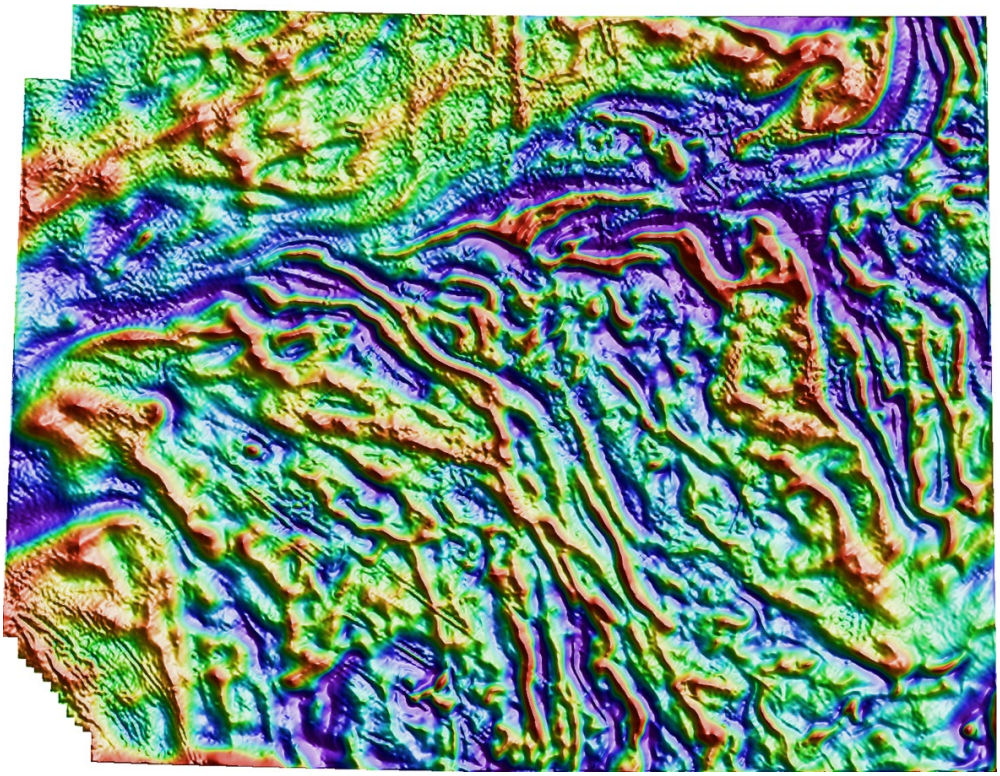

ABS_RMI_Fixed_RTP_vdmhgm_HSI_NE

Figure 6: The vertical derivative minus the HGM (VDMHGM) is a filter that accentuates the contrast in the first vertical derivative. This is useful for highlighting shallow sources in potential field data. It can also be useful when trying to pick the exact location to place a narrow magnetic unit or a narrow dense unit.

Magnetic data-processing results images (continued)
▶ Standard filtering — Tilt angle

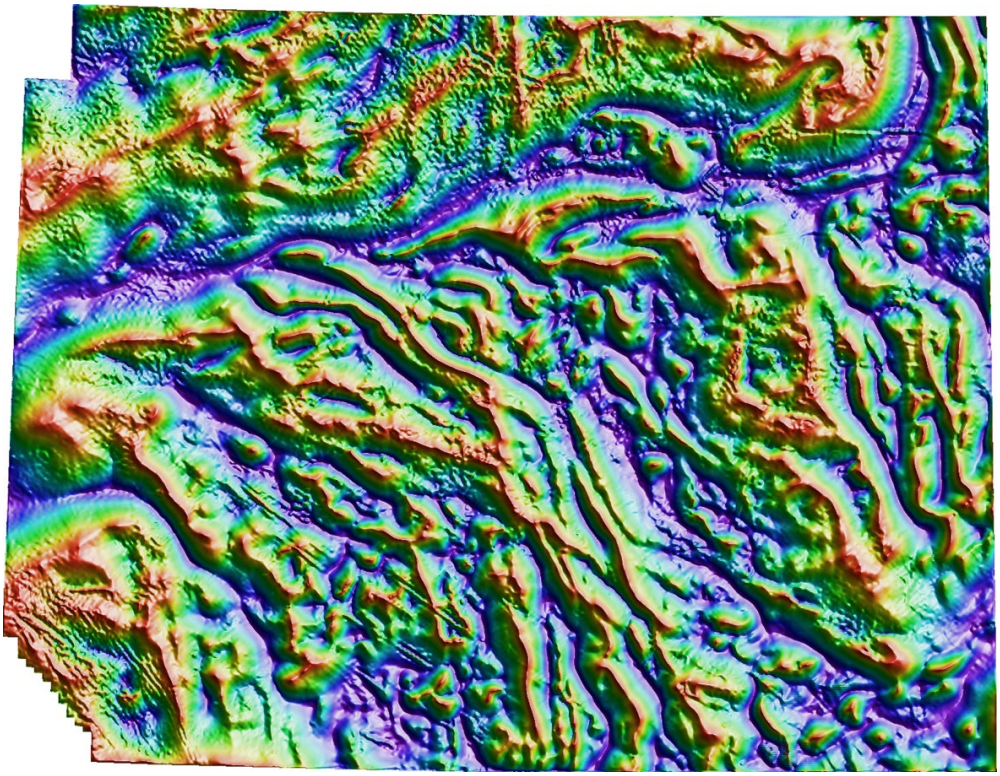

ABS_RMI_Fixed_RTP_tilt_HSI_NE

Figure 7: The tilt angle filter is the arctangent of the ratio of the vertical derivative to the horizontal gradient magnitude. This filter removes information about the amplitude of the signal, making the heights of peaks the same regardless of the susceptibility or density of the causative body. Structure and depth information are preserved. This makes it easier to see subtle features and some structures.

Magnetic data-processing results images (continued)
▶ Standard filtering — Analytic signal

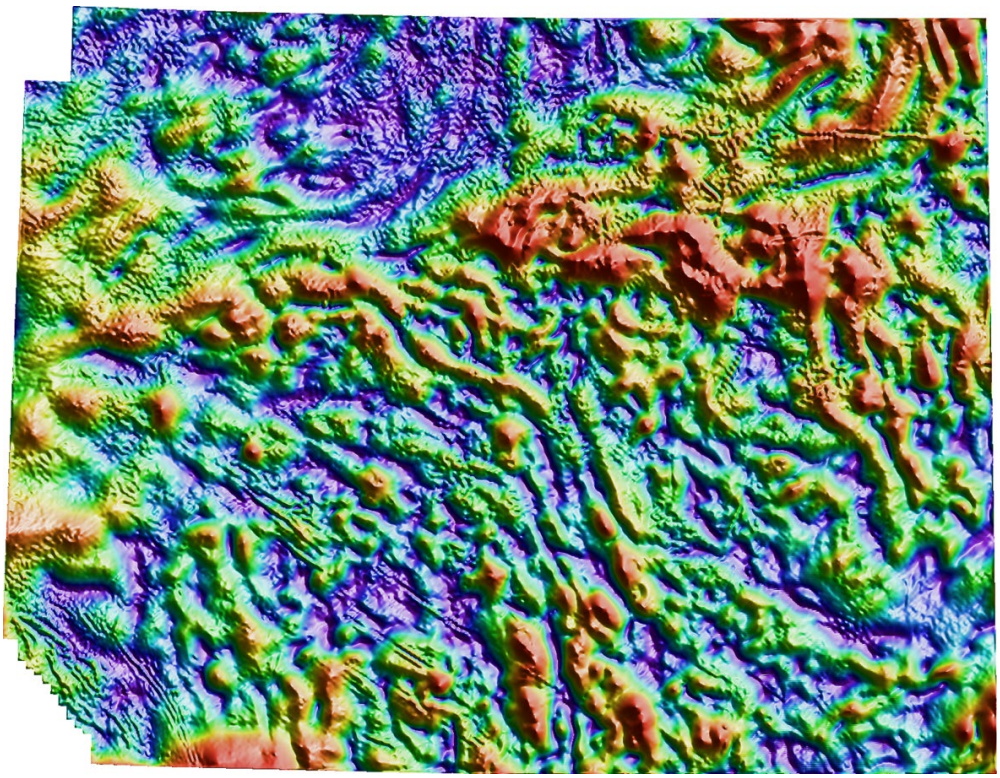

ABS_RMI_Fixed_RTP_asig_HSI_NE

Figure 8: Analytic signal of the RTP data. The analytic signal (also known as the total gradient magnitude) is calculated as $\sqrt{dx^2 + dy^2 + dz^2}$. This filter highlights the location of rapid changes in the data. Highs in the analytic signal correspond to high amplitudes in the vertical derivative (positive or negative) or high amplitudes in the horizontal gradient magnitude. Highs will occur over the top of small bodies with high susceptibility or high density contrast or at the edge of large-scale susceptibility or density contrast. Long-wavelength features are suppressed by this filter since it is based on derivative filters. This filter is relatively independent of magnetization direction and remanent magnetization.

Magnetic data-processing results images (continued)
▶ Standard filtering — Analytic signal of vertical integral

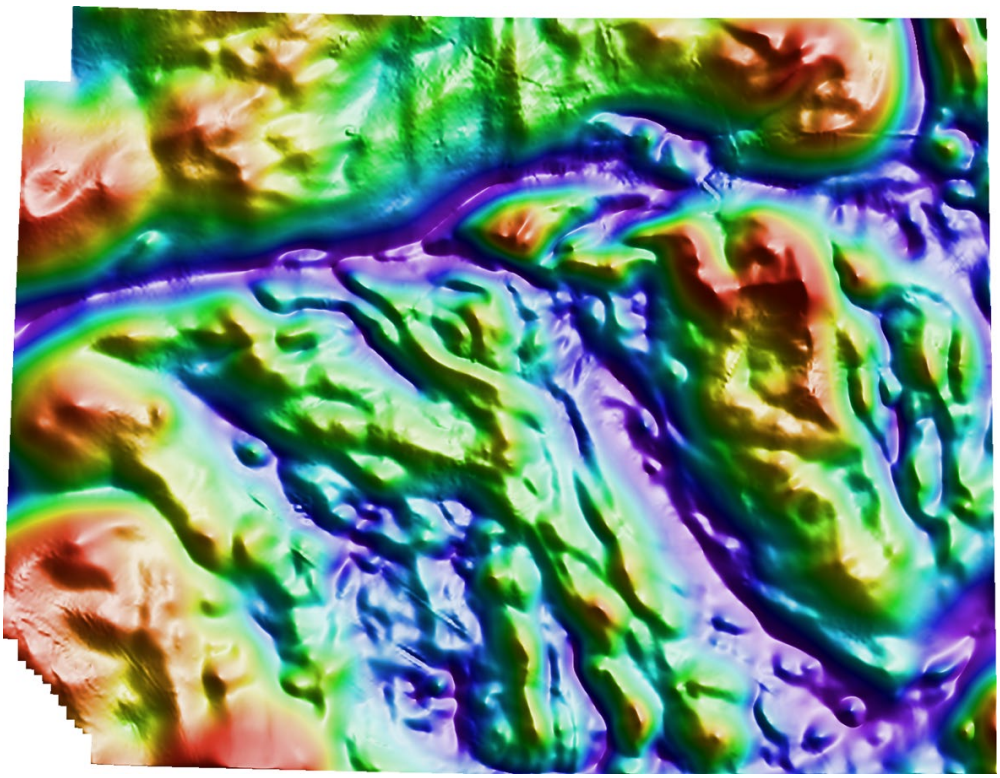

ABS_RMI_Fixed_RTP_vias_HSI_NE

Figure 9: The analytic signal filter was applied to the vertical integral of the magnetic data to produce this VIAS result. The analytic signal filter is described in the caption of **Figure 8**. Produces a grid with wavelength and amplitude characteristics that are similar to the RTP grid, but with reduced effects of remanent magnetization and magnetization direction.

Magnetic data-processing results images (continued)
▶ Standard filtering — Automatic gain control

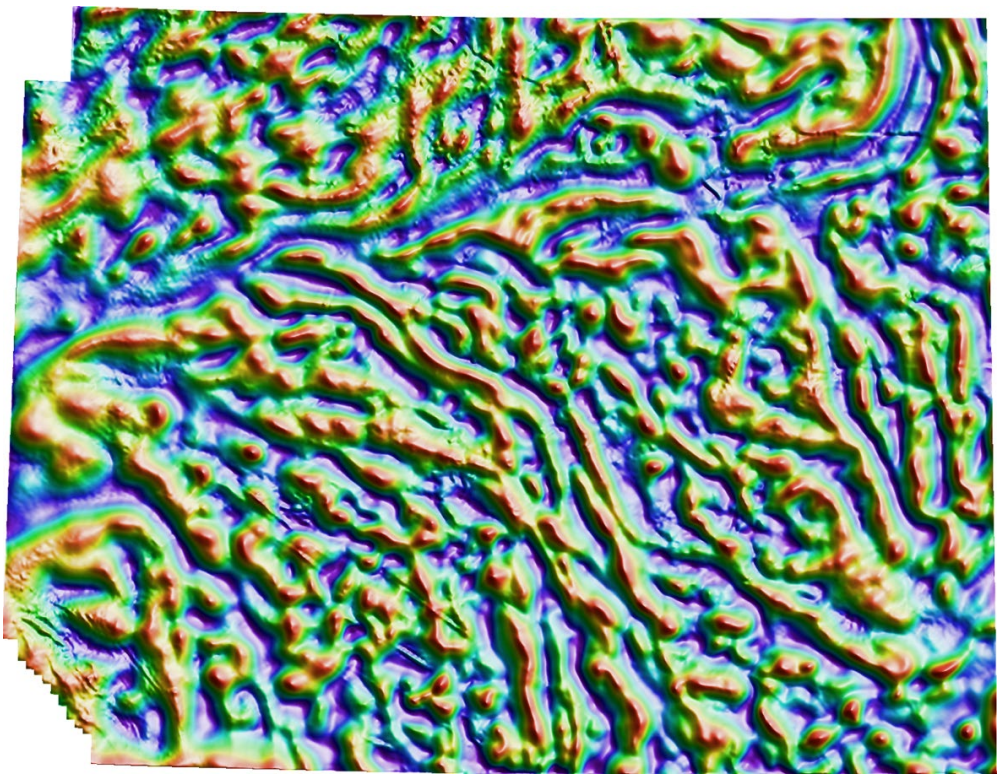

ABS_RMI_Fixed_RTP_AGC20_HSI_NE

Figure 10: The automatic gain control filter (AGC) is a means of evening out the amplitudes of anomalies. This makes more subtle features in the data visible. The filter also acts as a high-pass filter by suppressing the longer wavelengths.

Magnetic data-processing results images (continued)
▶ Standard filtering — Small-scale residual

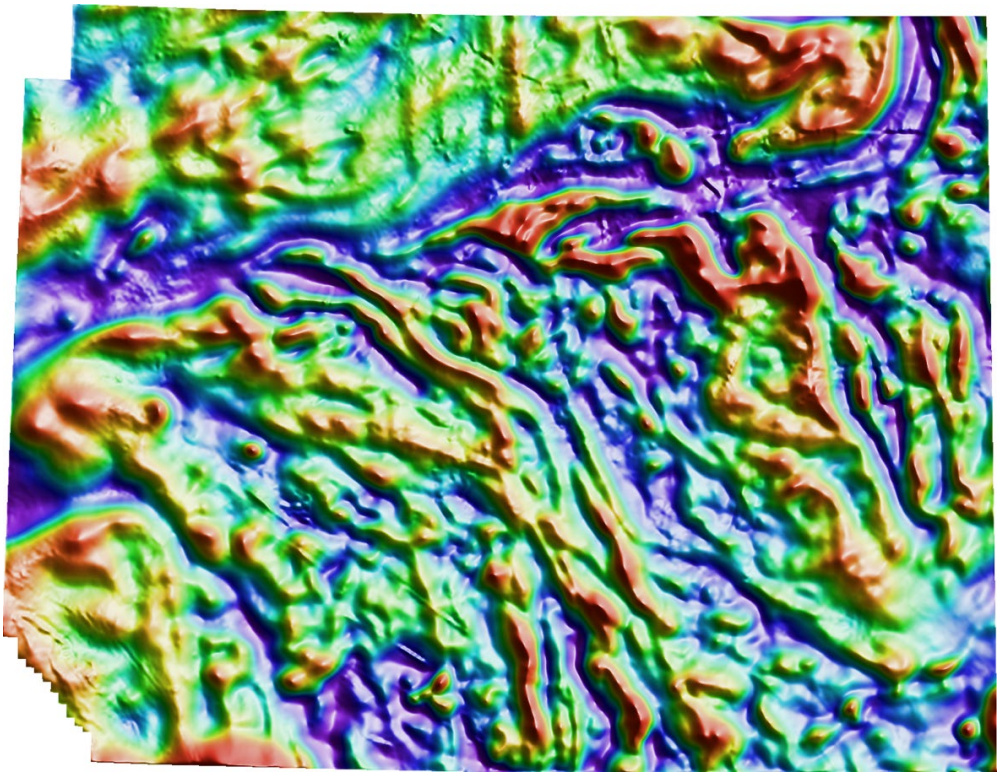

ABS_RMI_Fixed_RTP_res300_1500_HSI_NE

Figure 11: Differential upward continuation was applied to calculate the 300m-1500m residual of the RTP data in an attempt to separate sources from different depths (Jacobsen, 1987). The source depths should correspond to half of the upward continuation level. For this residual, that would be about 150m-750m depth.

Magnetic data-processing results images (continued)
▶ Standard filtering — Medium-scale residual

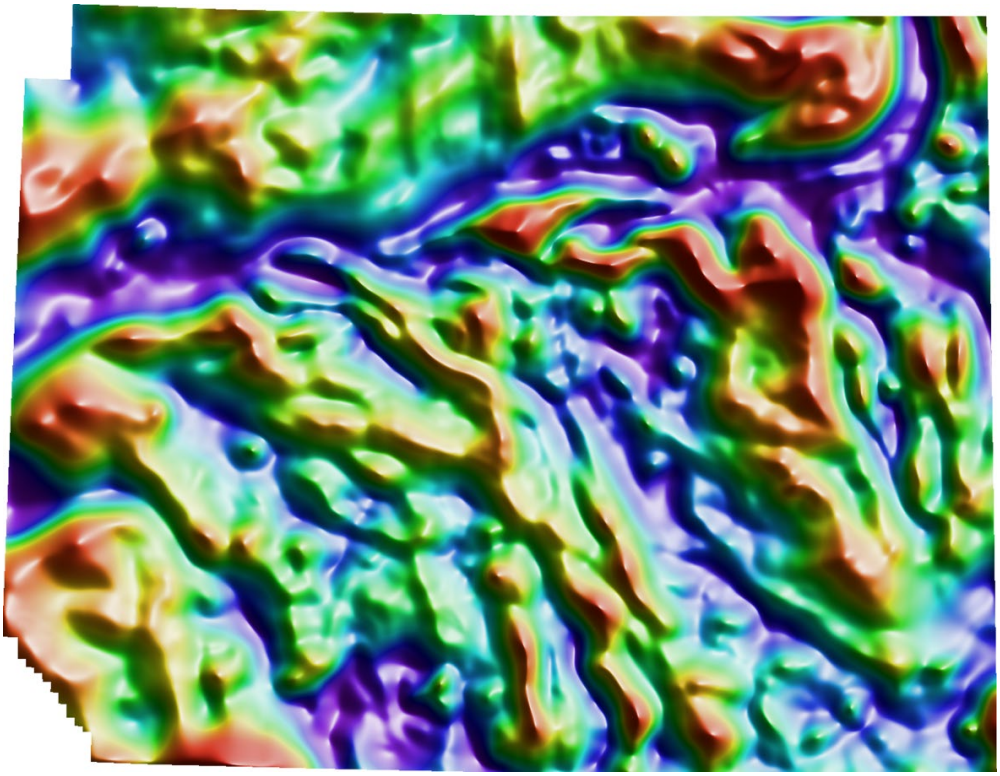

ABS_RMI_Fixed_RTP_res1500_6000_HSI_NE

Figure 12: Differential upward continuation was applied to calculate the 1500m-6000m residual of the RTP data in an attempt to separate sources from different depths (Jacobsen, 1987). The source depths should correspond to half of the upward continuation level. For this residual, that would be 750m-3000m depth.

Magnetic data-processing results images (continued)
▶ Standard filtering — Large-scale residual

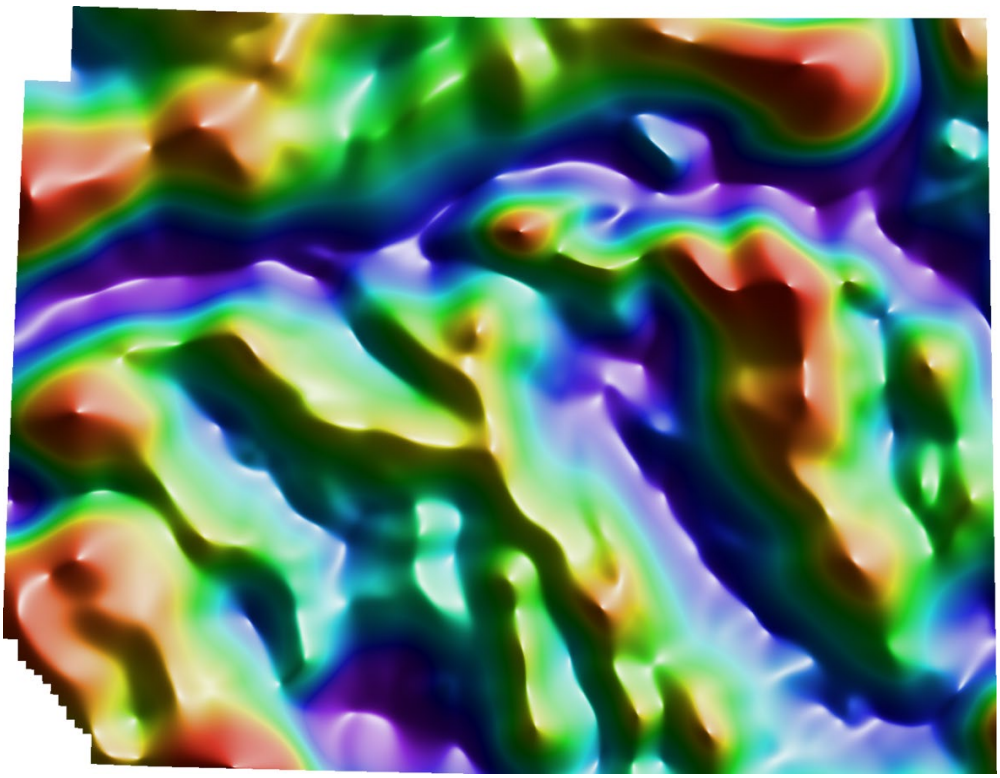

ABS_RMI_Fixed_RTP_res6000_15000_HSI_NE

Figure 13: Differential upward continuation was applied to calculate the 6000m-15000m residual of the RTP data in an attempt to separate sources from different depths (Jacobsen, 1987). The source depths should correspond to half of the upward continuation level. For this residual, that would be 3000m-7500m depth.

Magnetic data-processing results images (continued)
▶ Standard filtering — Pseudogravity

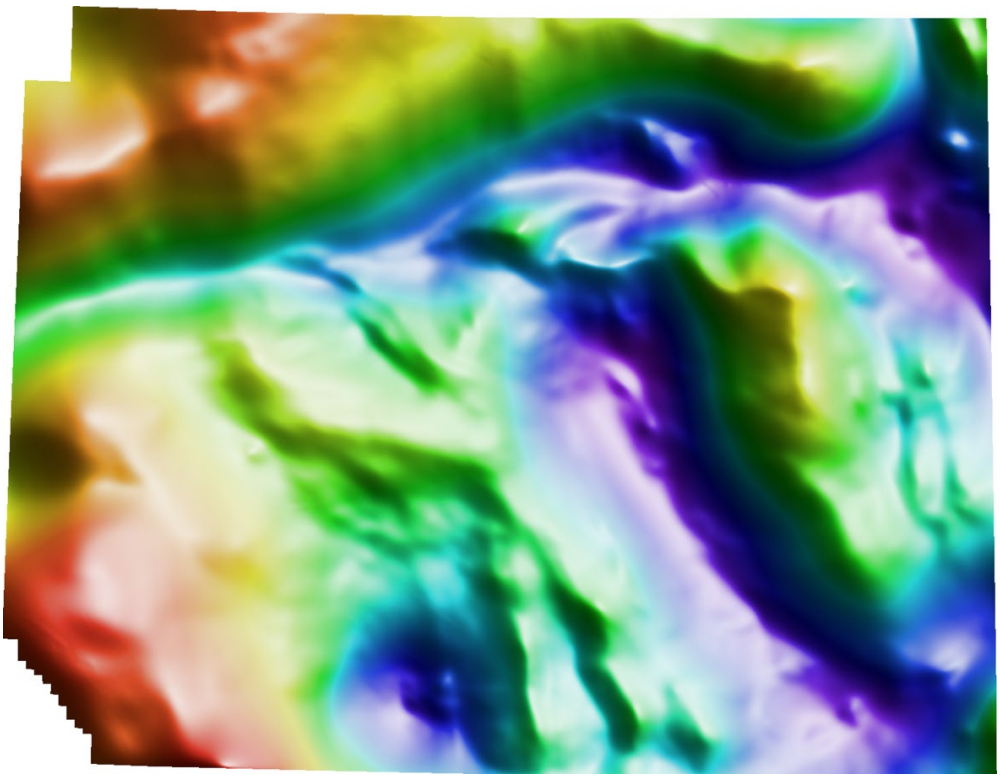

ABS_RMI_Fixed_RTP_PGrav_HSI_NE

Figure 14: Pseudogravity is generated by calculating the vertical integral of reduced-to-the-pole magnetic data and then using Poisson's relation (correlation between magnetic potential and gravitational potential) to scale the result. This generates a grid that is the expected gravity field if density were distributed in the same way as magnetic susceptibility in the project area. This is not a true gravity grid because it is highly unlikely that susceptibility and density are perfectly correlated. This filter enhances long-wavelength features and is good for highlighting large-scale features.

Magnetic data-processing results images (continued)
▶ Standard filtering — Pseudogravity residual

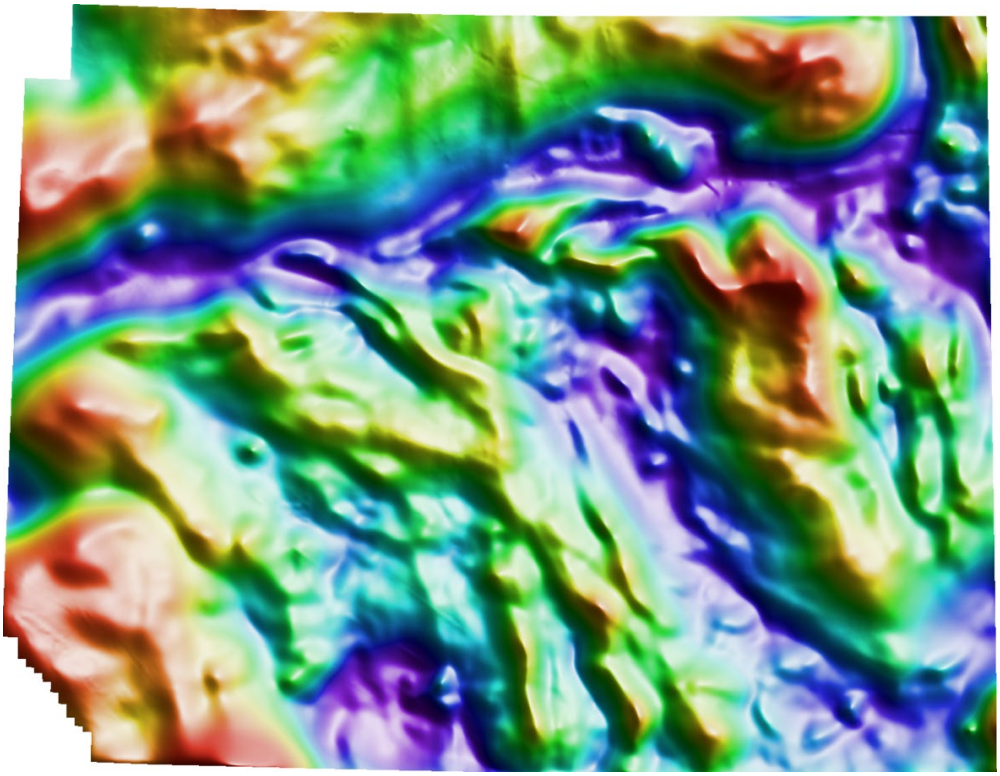

ABS_RMI_Fixed_RTP_PGravRes_HSI_NE

Figure 15: Differential upward continuation was applied to the pseudogravity grid to generate a 0-2000m residual. This removes the longest wavelength features to allow intermediate-scale features to be seen.

Magnetic data-processing results images (continued)
▶ Standard filtering — HGM of pseudogravity residual

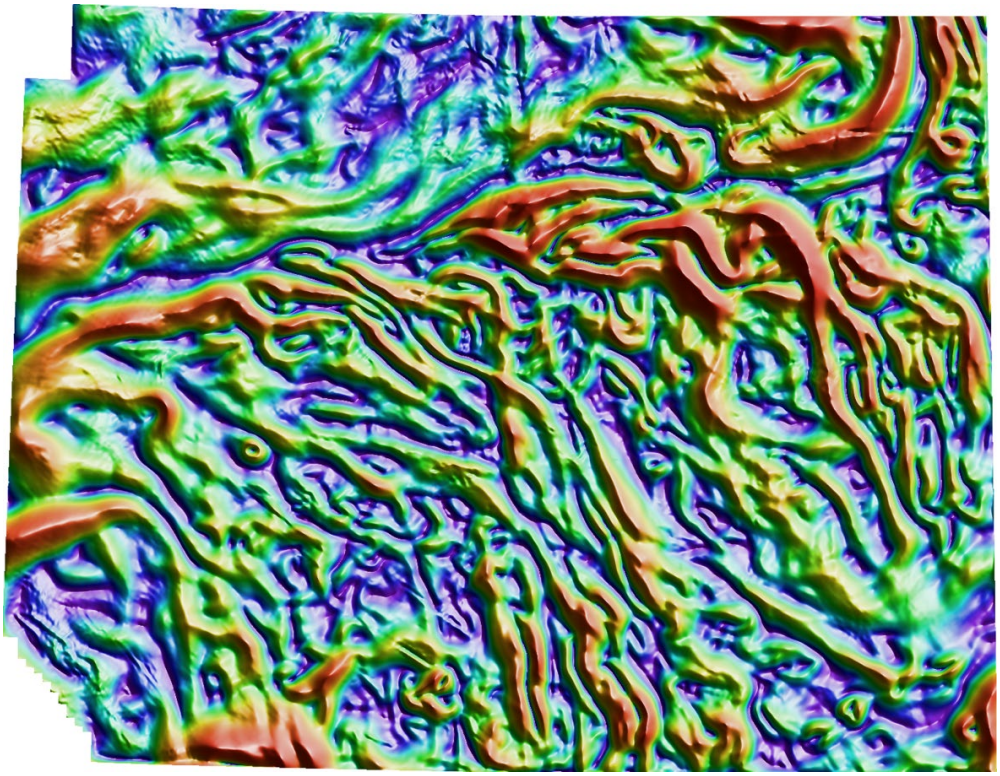

ABS_RMI_Fixed_RTP_PGravResHGM_HSI_NE

Figure 16 The horizontal gradient was calculated from the pseudogravity residual as described in the caption for **Figure 5**. The results highlight the edges of intermediate-scale features. However, this filter is affected by magnetization direction and remanent magnetization.

Magnetic data-processing results images (continued)
▶ Standard filtering images — Using ternary images

RGB

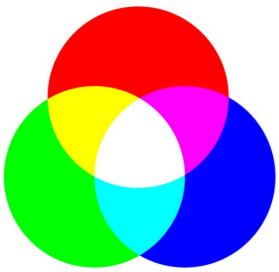

For RGB images:
Green + blue = cyan
Red + blue = magenta
Red + green = yellow
Red + green + blue = white
Low in red + green + blue = black

CMYK

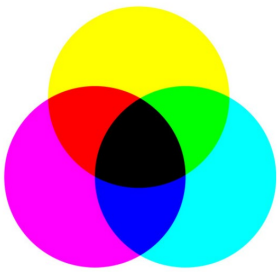

For CMY images:
Magenta + yellow = red
Cyan + yellow = green
Cyan + magenta = blue
Cyan + magenta + yellow = black
Low in red + green + blue = white

Figure 17: The information above shows how to interpret the colors in the RGB and CMY ternary images appearing in the next few figures, which are:

(i) Ternary of directional derivatives — This image encapsulates information about how steeply the gradient is changing in 3 orthogonal directions, namely the X and Y directions (within the plane of the image), and the Z direction (perpendicular to the plane of the image). All of this gradient information combines to help the observer intuitively identify the various major geological domains residing throughout the area of interest, and how these domains relate to each other.

(ii) Ternary of 1VD, tilt angle, and HGM — This image helps the observer intuitively understand where major structural features are situated, where breaks in the continuity of the magnetic 'fabric' occur, and how the textural character of the magnetic data changes from one locale to the next.

(iii) Ternary of residuals — Again, this image helps the observer intuitively understand where major structural features are situated, where breaks in the continuity of the magnetic 'fabric' occur, and how the textural character of the magnetic data changes from one locale to the next. However, features seen are generally coarser than those appearing in the ternary combining 1VD, tilt and HGM.

(iv) Ternary of RTP, VIAS, and analytic signal — This image helps the observer intuitively understand which subareas may be most affected by remanence (red locales in the CMY image).

(v) Ternary of pseudogravity results — This image combines three pseudogravity-related grids and produces an image that may assist the observer with intuitively grasping the geological affinity of features in the data.

Magnetic data-processing results images (continued)
▶ Standard filtering — Ternary of directional derivatives

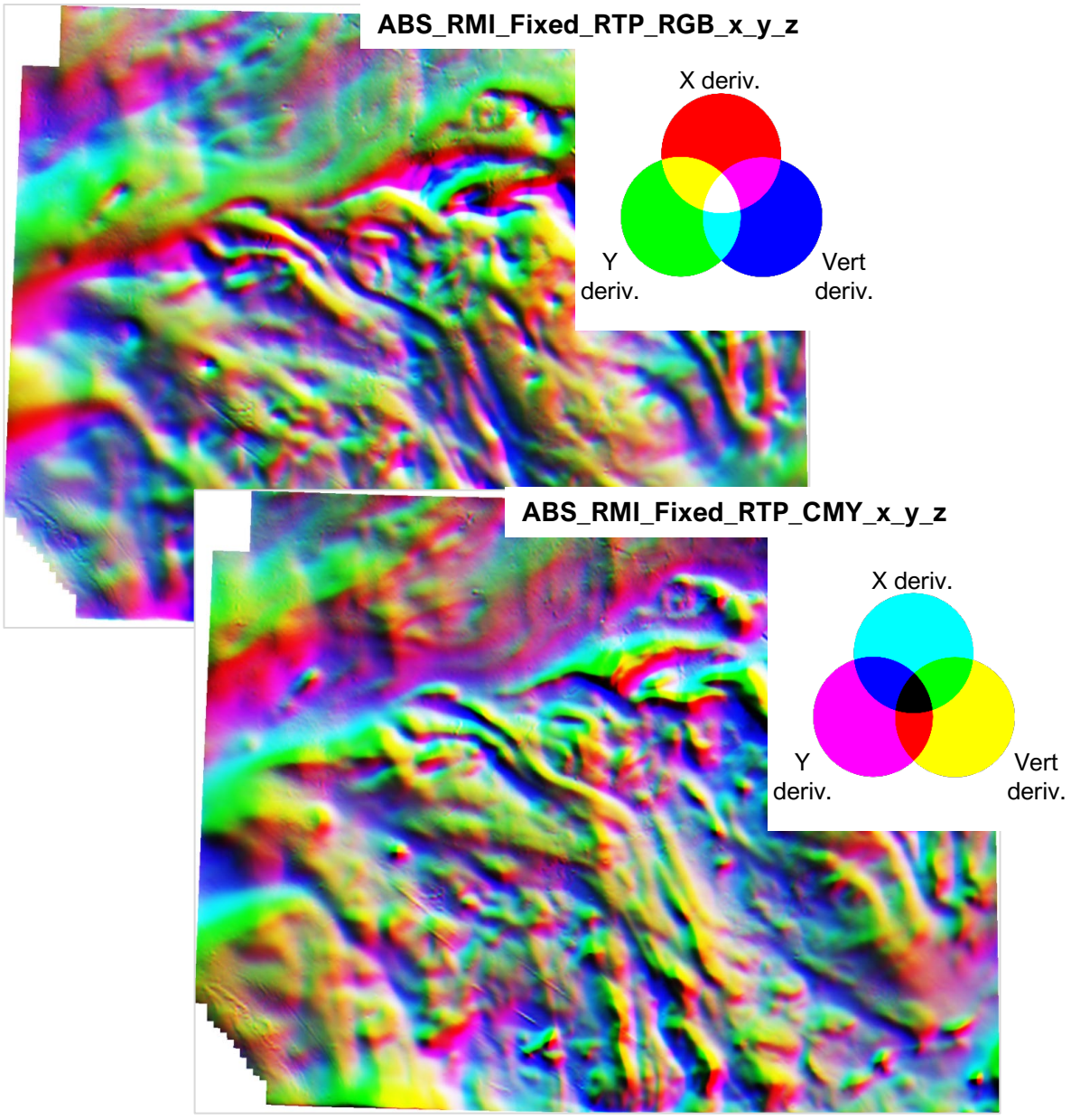

Figure 18: RGB and CMY ternary images co-displaying the X-gradient (R/C channels), Y-gradient (G/M channels), and Z-gradient (i.e., vertical derivative) (B/Y channels).

Magnetic data-processing results images (continued)
▶ Standard filtering — Ternary of 1VD, tilt, HGM

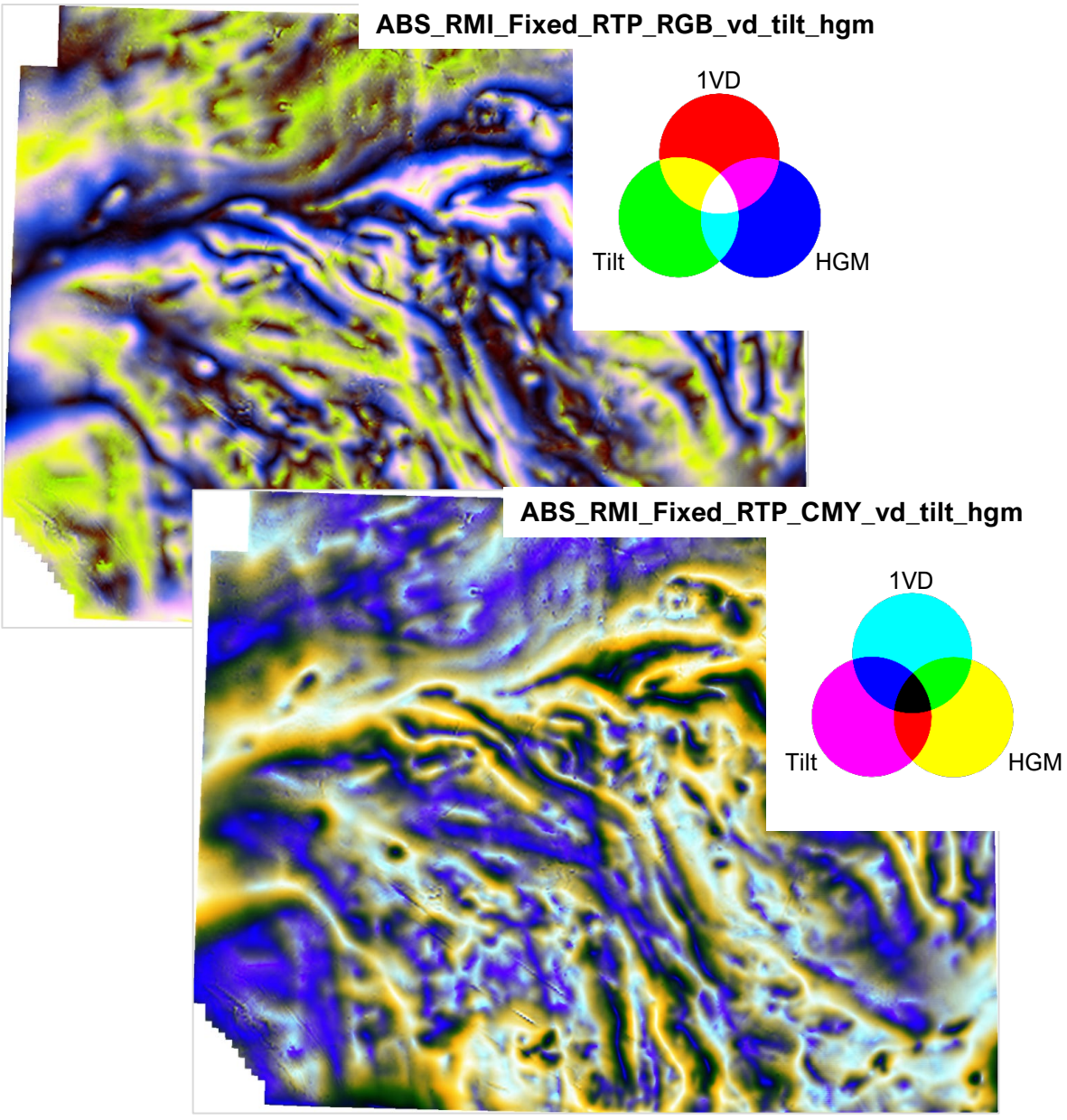

Figure 19: RGB and CMY ternary images co-displaying the vertical derivative (R/C channels), tilt angle (G/M channels), and HGM (B/Y channels).

Magnetic data-processing results images (continued)

▶ Standard filtering — Ternary of residuals

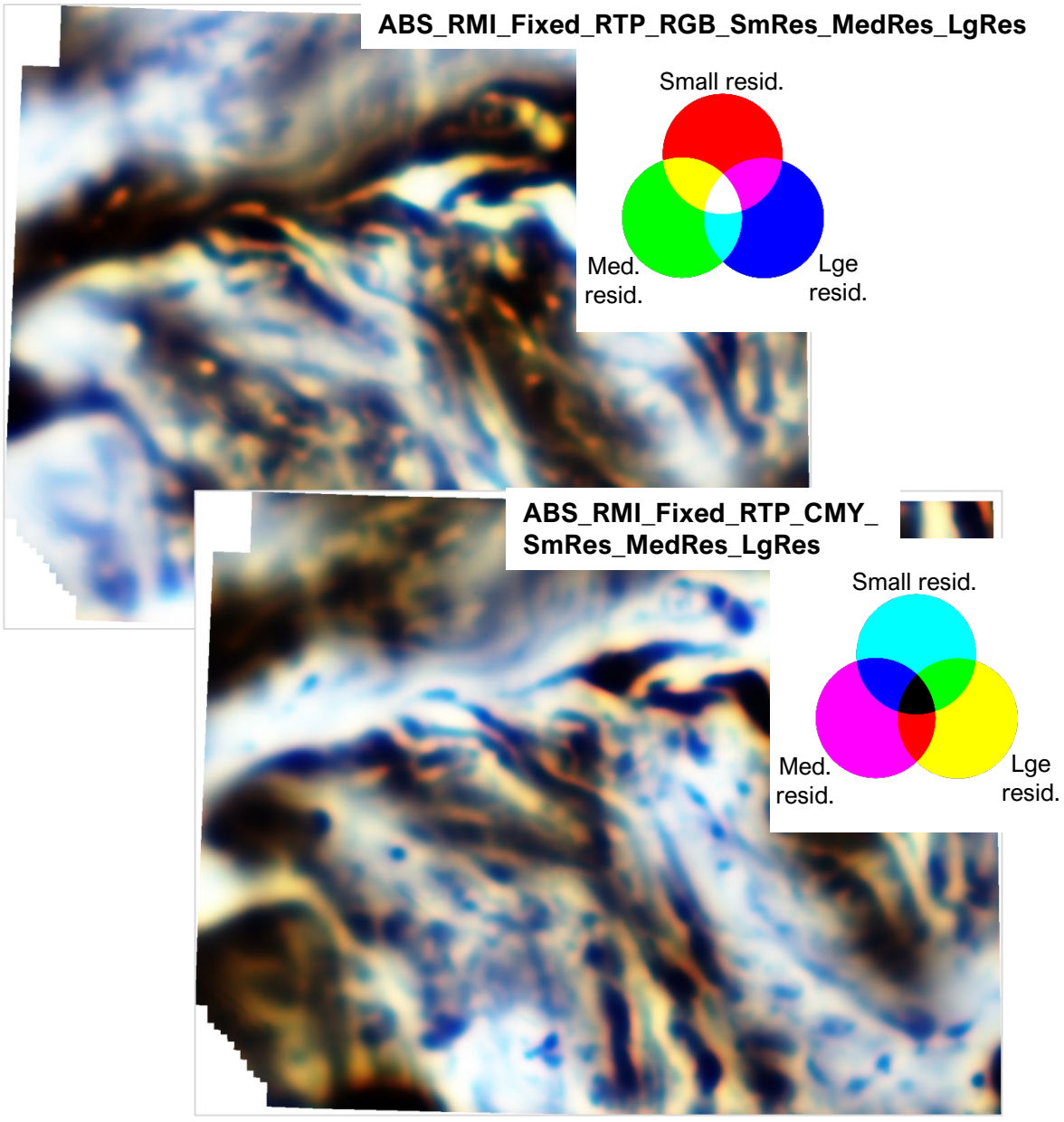

Figure 20: RGB and CMY ternary images co-displaying the small-scale (R/C channels), medium-scale (G/M channels), and large-scale residuals (B/Y channels).

Magnetic data-processing results images (continued)

▶ Standard filtering — Ternary of RTP, VIAS, Asig

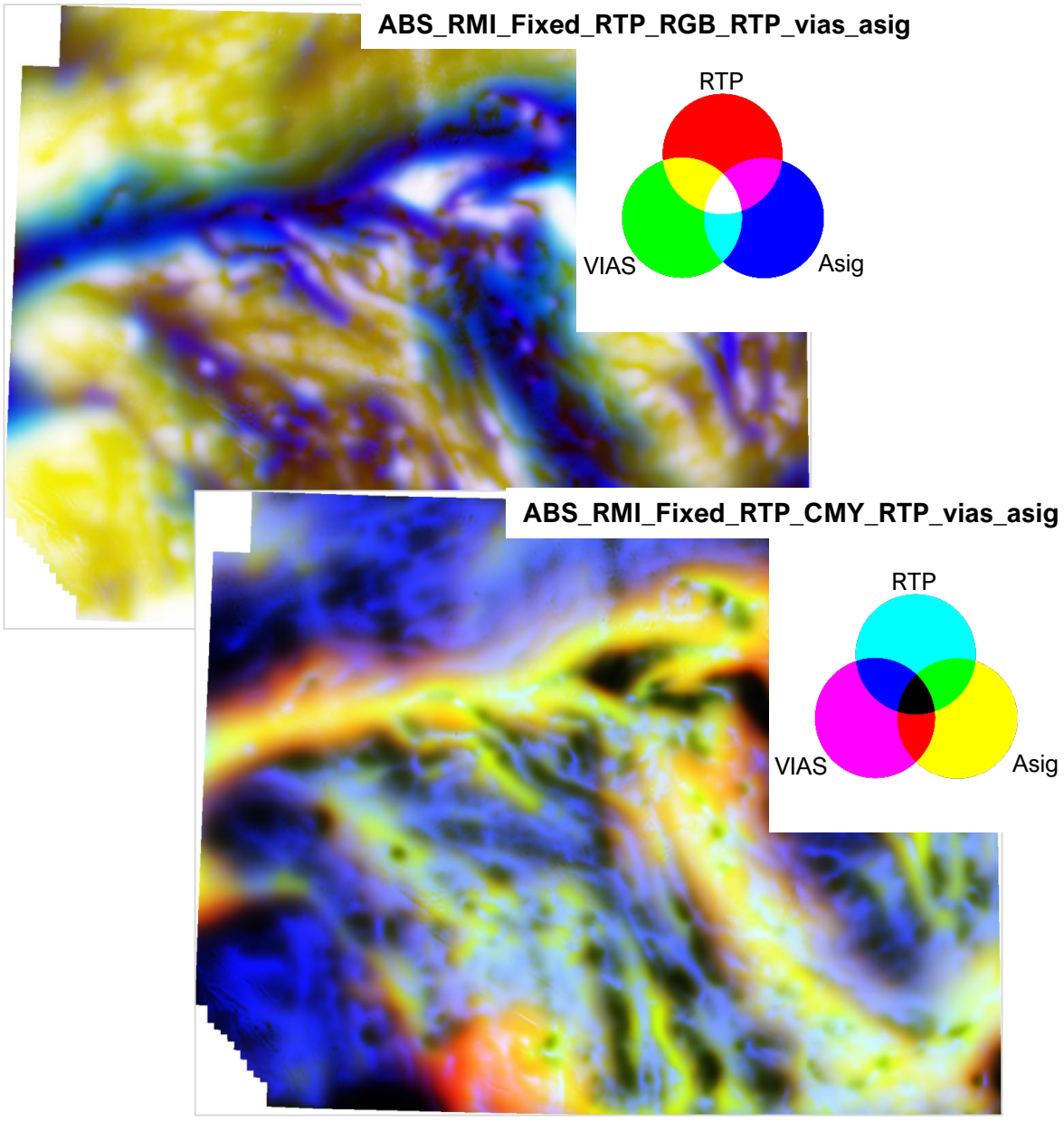

Figure 21: RGB and CMY ternary images co-displaying the RTP (R/C channels), VIAS (G/M channels), and analytic signal (B/Y channels).

Magnetic data-processing results images (continued)
▶ Standard filtering — Ternary of pseudogravity results

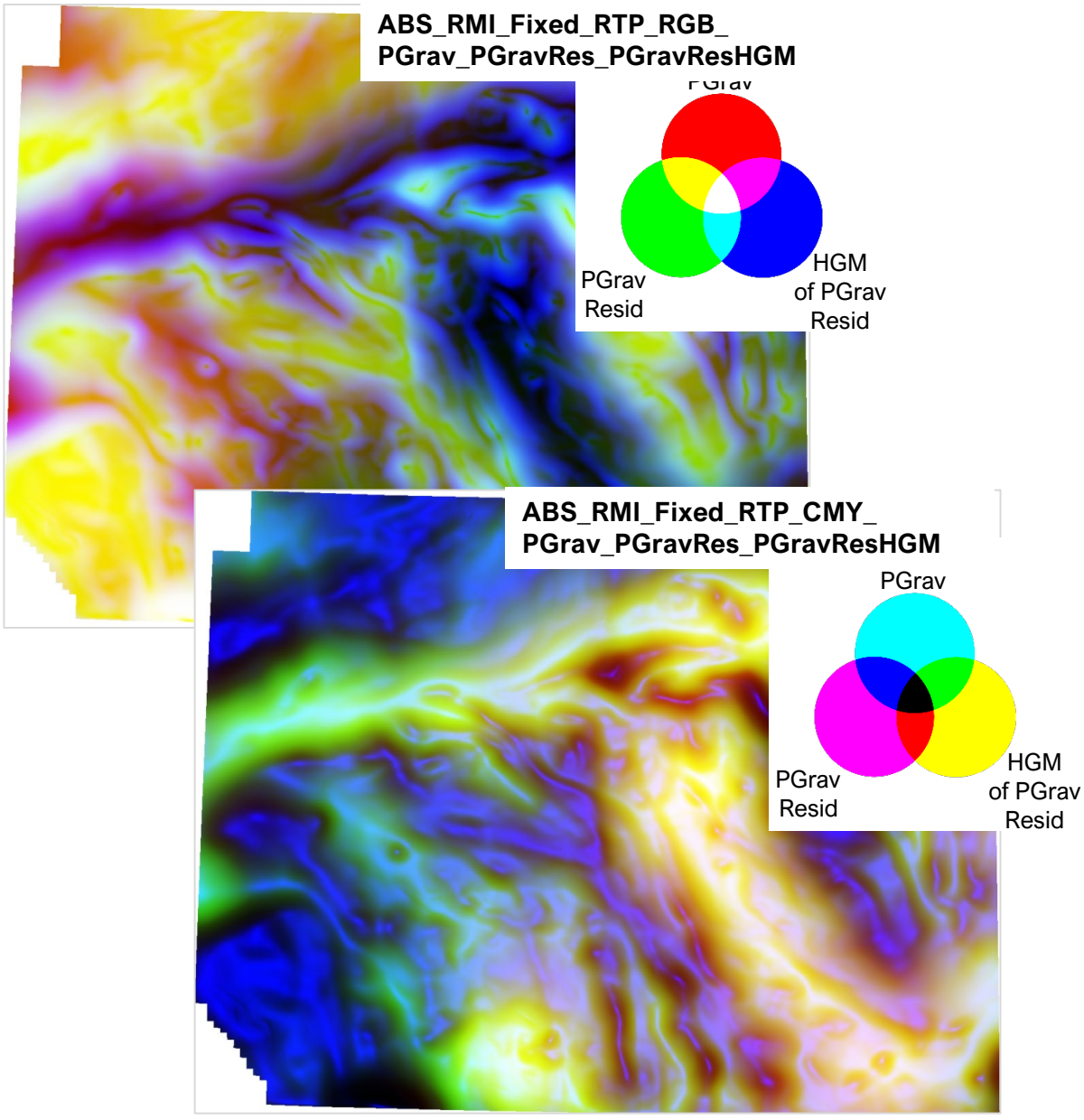

Figure 22: RGB and CMY ternary images co-displaying pseudograv (R/C channels), pseudograv residual (G/M channels), and HGM of pseudograv residual (B/Y channels).

Magnetic data-processing results images (continued)
▶ Total structure detection — Analysis of RTP

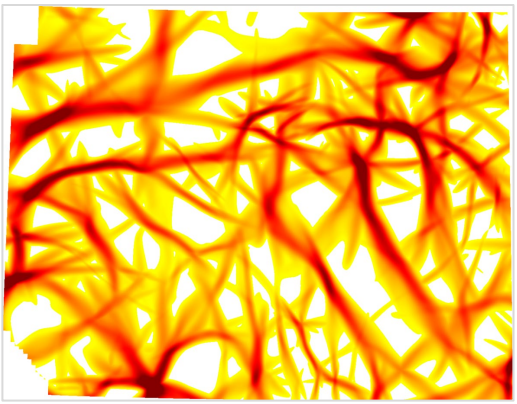

Figure 23: Representative image** showing 4000m structure detection results for the RTP data. TOP: Total structure detected. MIDDLE: Map of thresholded structural orientations. BOTTOM: Total structure in vectorized form (black lines with displayed thickness varying according to median value) over the project area's RTP image.

ABS_RMI_Fixed_RTP_Struct4000_Total

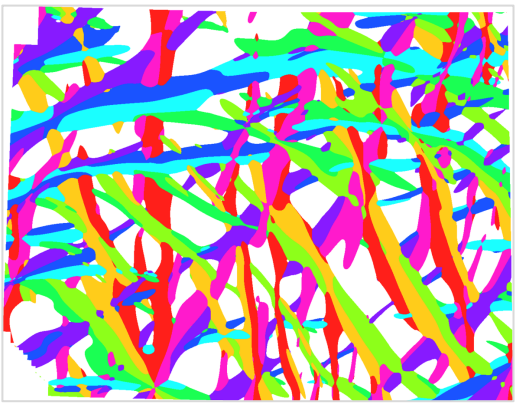

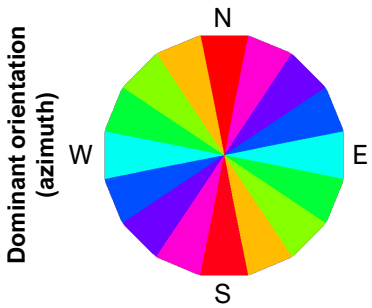

ABS_RMI_Fixed_RTP_Struct4000_OriDom_Th

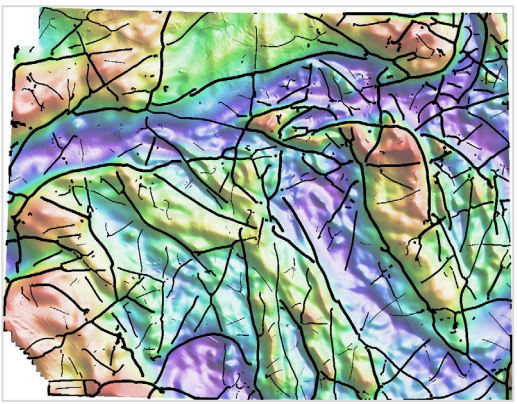

ABS_RMI_Fixed_RTP_Struct4000_Total_Vec

ABS_RMI_Fixed_RTP_HSI_NE

** *Further scales of results also delivered.*

Magnetic data-processing results images (continued)

▶ Total structure detection — Analysis of RTP

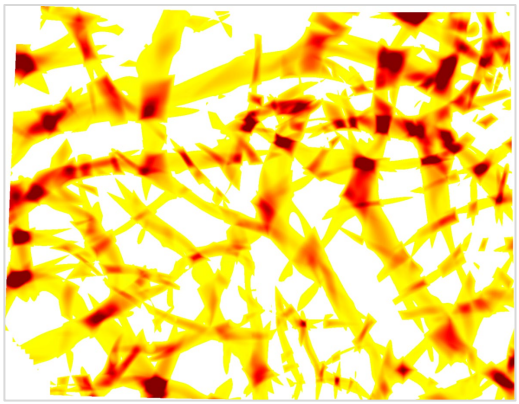

Figure 24: Representative image** showing 4000m structure detection results for the RTP data. TOP: Total structure intersections detected. MIDDLE: Intersections co-displayed with same-scale structures (line color and thickness varies according to structure's median value). BOTTOM: Intersections co-displayed with strong intersections (black-lined polygons) over gray RTP.

ABS_RMI_Fixed_RTP_Struct4000_Int

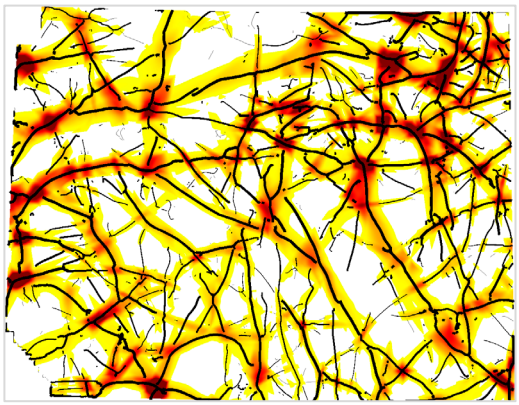

ABS_RMI_Fixed_RTP_Struct4000_Int

ABS_RMI_Fixed_RTP_Struct4000_Total_Vec

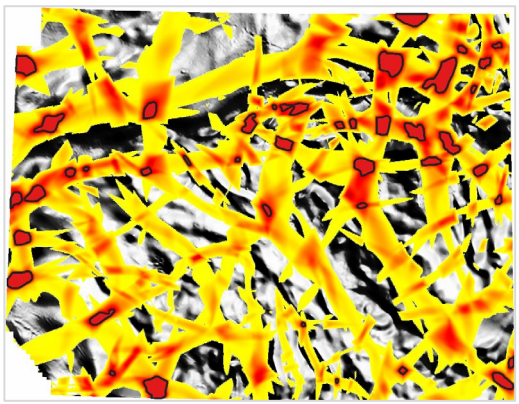

ABS_RMI_Fixed_RTP_Struct4000_Int

ABS_RMI_Fixed_RTP_Struct4000_Int_HTh_Vec

ABS_RMI_Fixed_RTP_HSI_NE (grayscale)

** *Further scales of results also delivered.*

Magnetic data-processing results images (continued)
▶ Total structure detection — Analysis of AGC

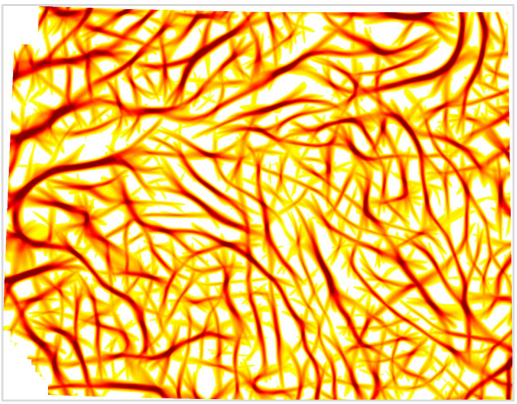

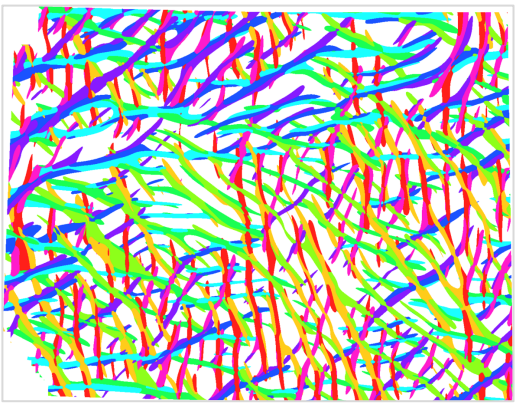

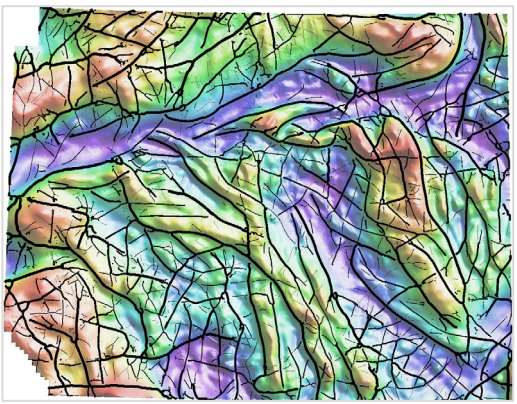

Figure 25: Representative image** showing 4000m structure detection results for the RTP's AGC. TOP: Total structure detected. MIDDLE: Map of thresholded structural orientations. BOTTOM: Total structure in vectorized form (black lines with displayed thickness varying according to median value) over the project area's RTP image.

ABS_RMI_Fixed_RTP_AGC20_Struct4000_Total

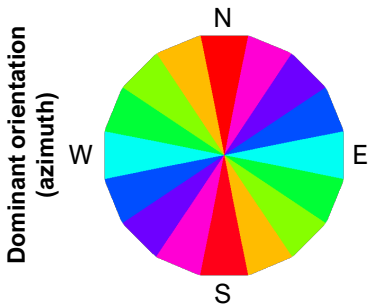

ABS_RMI_Fixed_RTP_AGC20_Struct4000_OriDom_Th

ABS_RMI_Fixed_RTP_AGC20_Struct4000_Total_Vec

ABS_RMI_Fixed_RTP_HSI_NE

** *Further scales of results also delivered.*

Magnetic data-processing results images (continued)
▶ Total structure detection — Analysis of AGC

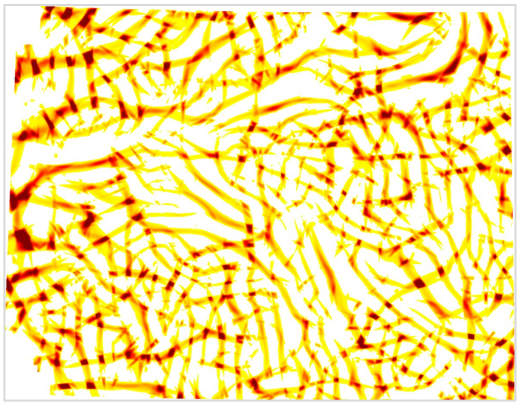

Figure 26: Representative image** showing 4000m structure detection results for the RTP's AGC. TOP: Total structure intersections detected. MIDDLE: Intersections co-displayed with same-scale structures (line color and thickness varies according to structure's median value). BOTTOM: Intersections co-displayed with strong intersections (black-lined polygons) over gray RTP.

ABS_RMI_Fixed_RTP_AGC20_Struct4000_Int

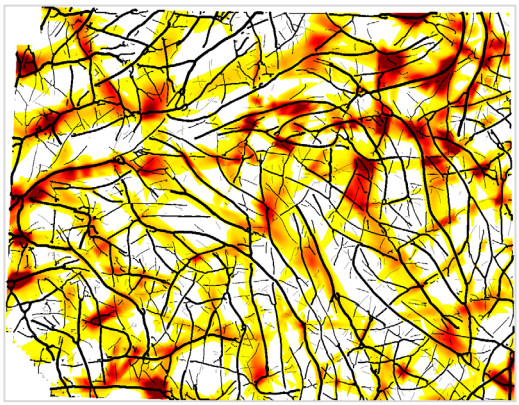

ABS_RMI_Fixed_RTP_Struct4000_Int

ABS_RMI_Fixed_RTP_AGC20_Struct4000_Total_Vec

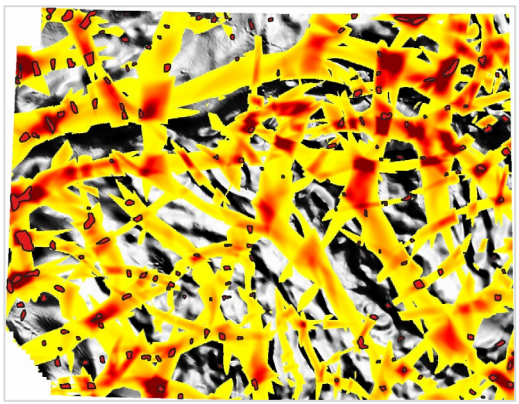

ABS_RMI_Fixed_RTP_Struct4000_Int

ABS_RMI_Fixed_RTP_AGC20_Struct4000_Int_HTh_Vec

ABS_RMI_Fixed_RTP_HSI_NE (grayscale)

** *Further scales of results also delivered.*

Magnetic data-processing results images (continued)
▶ Parallel/cross structure — AGC fabric orientation

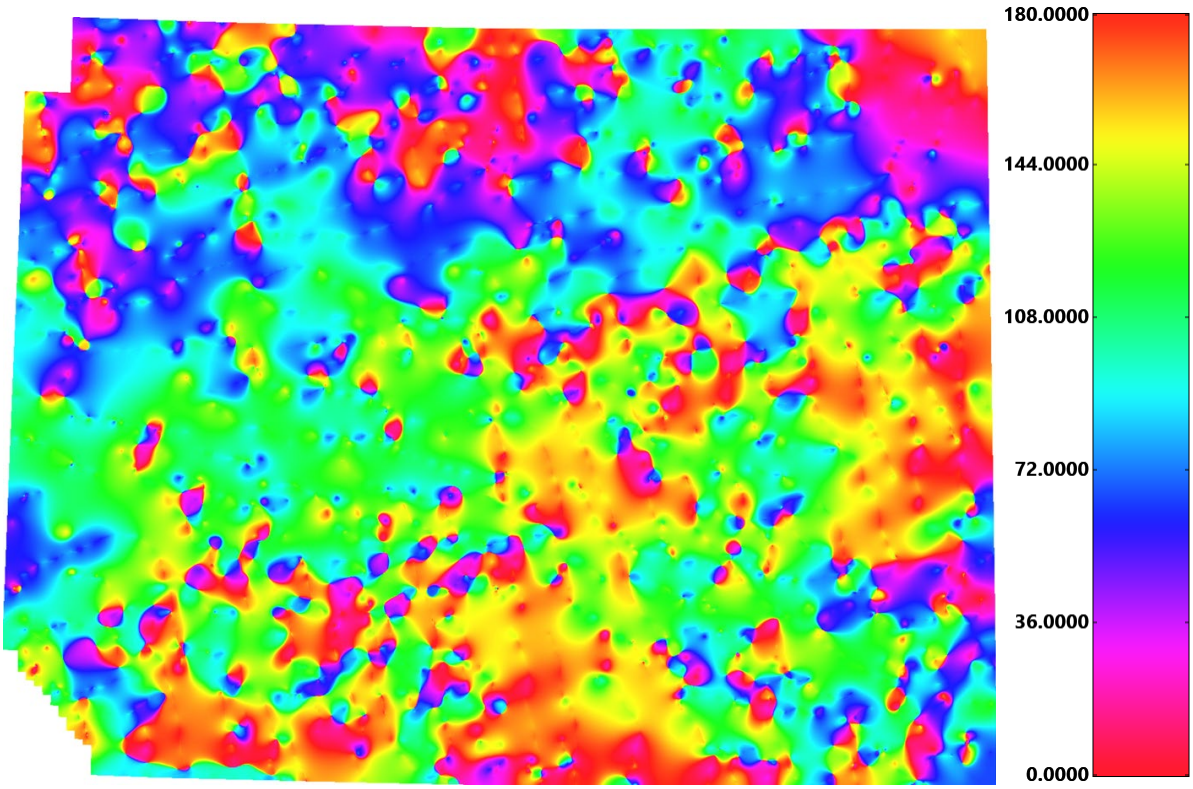

ABS_RMI_Fixed_RTP_AGC20_FabricOri

Figure 27: The orientation of magnetic units was determined by taking the AGC of the RTP magnetic data and applying an anisotropic diffusion filter to highlight linear features. Ridge lines were extracted from the enhanced grid and the orientation of the ridge lines was determine. The resulting orientations were interpolated and smoothed to generate the map shown above. The green areas are dominated by WNW to NW trends. The blue and cyan areas are dominated by ENE trends while the magenta indicates NNE trends. The reds and oranges indicate areas that are dominated by NNW to N-trending features.

Magnetic data-processing results images (continued)

▶ Parallel/cross structure — RTP

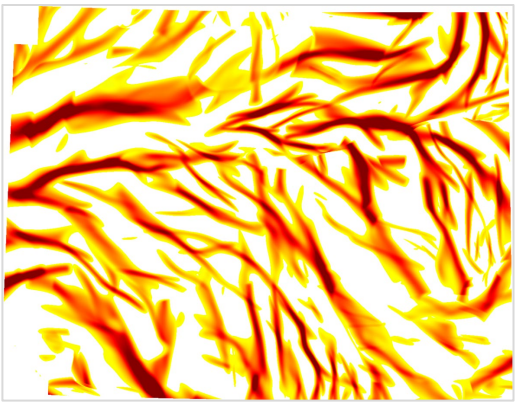

Figure 28: Representative image** showing 2000m belt-parallel structure detection results for the RTP data. TOP: Parallel structures detected. MIDDLE: The same results in vectorized form (displayed line thickness varies according to structure's median value). BOTTOM: Vectorized results co-displayed with the RTP image.

ABS_RMI_Fixed_RTP_Struct2000_Para

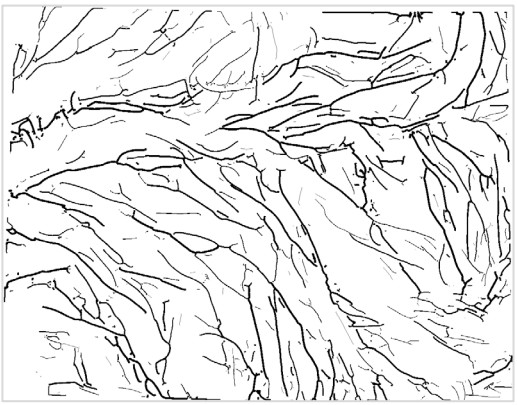

ABS_RMI_Fixed_RTP_Struct2000_Para_Vec

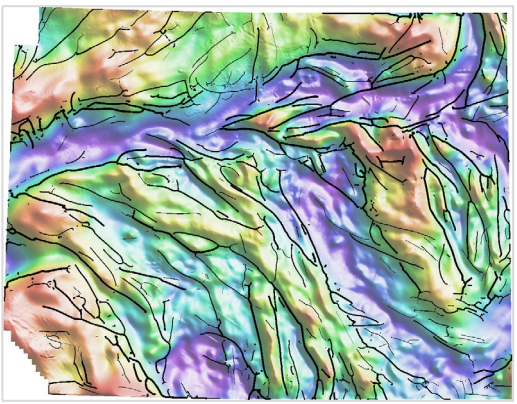

ABS_RMI_Fixed_RTP_Struct2000_Para_Vec

ABS_RMI_Fixed_RTP_HSI_NE

** *Further scales of results also delivered.*

Magnetic data-processing results images (continued)

▶ Parallel/cross structure — RTP

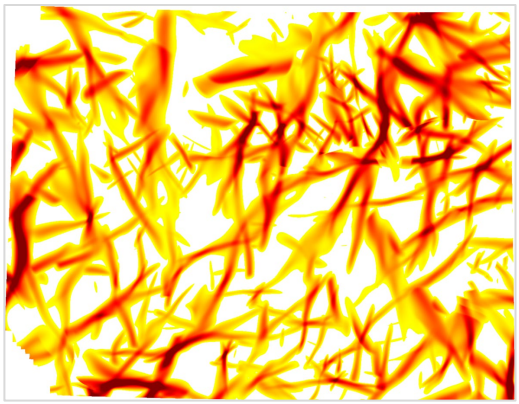

Figure 29: Representative image** showing 2000m belt-crossing structure detection results for the RTP data. TOP: Cross structures detected. MIDDLE: The same results in vectorized form (displayed line thickness varies according to structure's median value). BOTTOM: Vectorized results co-displayed with the RTP image.

ABS_RMI_Fixed_RTP_Struct2000_Cross

ABS_RMI_Fixed_RTP_Struct2000_Cross_Vec

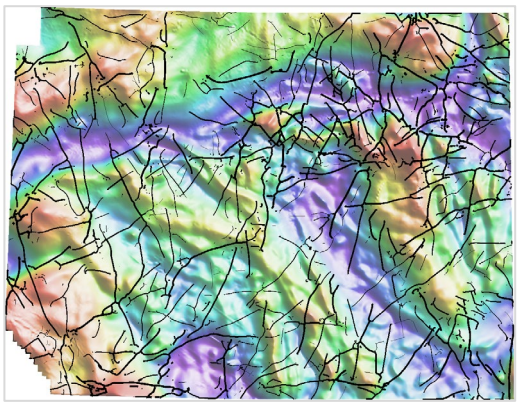

ABS_RMI_Fixed_RTP_Struct2000_Cross_Vec

ABS_RMI_Fixed_RTP_HSI_NE

** *Further scales of results also delivered.*

Magnetic data-processing results images (continued)

▶ Parallel/cross structure — AGC

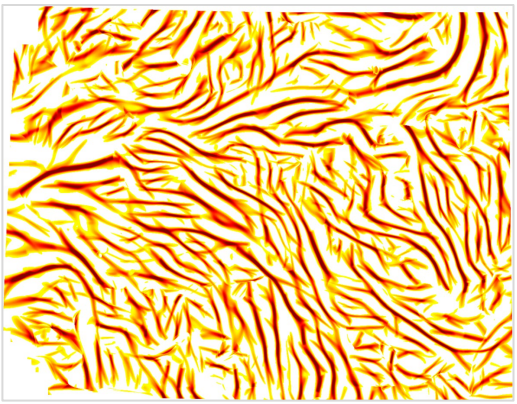

Figure 30: Representative image** showing 2000m belt-parallel structure detection results for the RTP's AGC. TOP: Parallel structures detected. MIDDLE: The same results in vectorized form (displayed line thickness varies according to structure's median value). BOTTOM: Vectorized results co-displayed with the RTP image.

ABS_RMI_Fixed_RTP_AGC20_Struct2000_Para

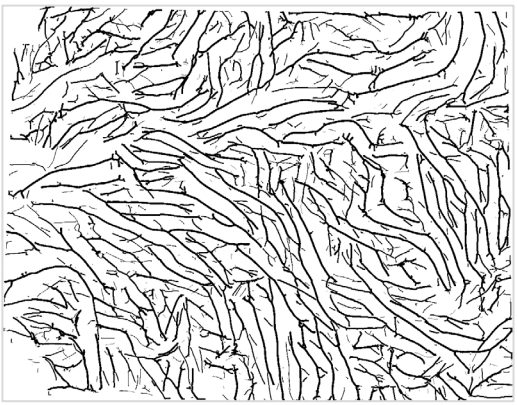

ABS_RMI_Fixed_RTP_AGC20_Struct2000_Para_Vec

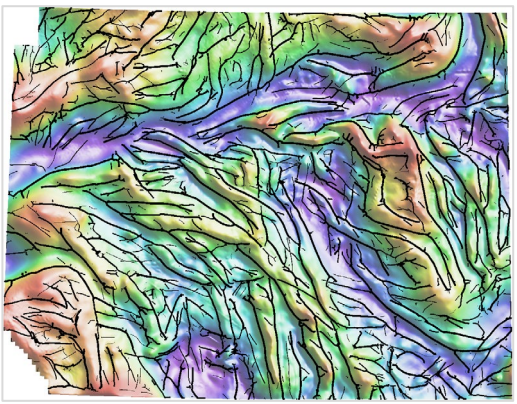

ABS_RMI_Fixed_RTP_AGC20_Struct2000_Para_Vec

ABS_RMI_Fixed_RTP_HSI_NE

** *Further scales of results also delivered.*

Magnetic data-processing results images (continued)

▶ Parallel/cross structure — AGC

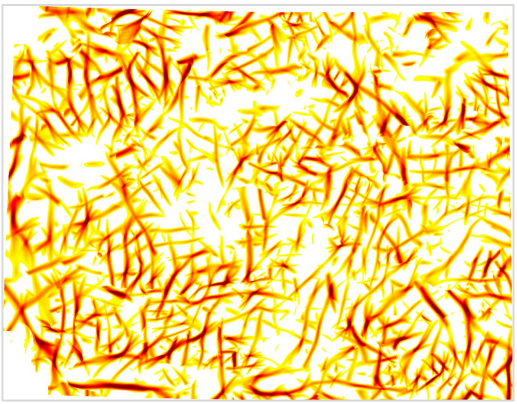

Figure 31: Representative image** showing 2000m belt-crossing structure detection results for the RTP's AGC. TOP: Cross structures detected. MIDDLE: The same results in vectorized form (displayed line thickness varies according to structure's median value). BOTTOM: Vectorized results co-displayed with the RTP image.

ABS_RMI_Fixed_RTP_AGC20_Struct2000_Cross

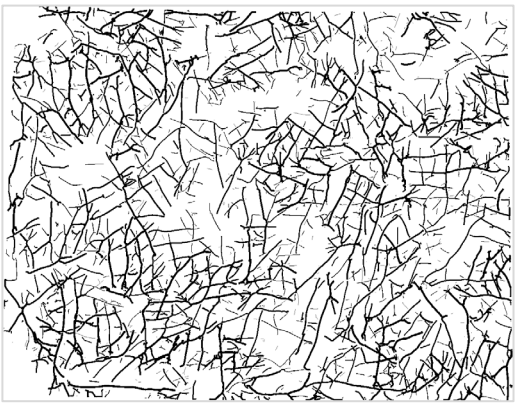

ABS_RMI_Fixed_RTP_AGC20_Struct2000_Cross_Vec

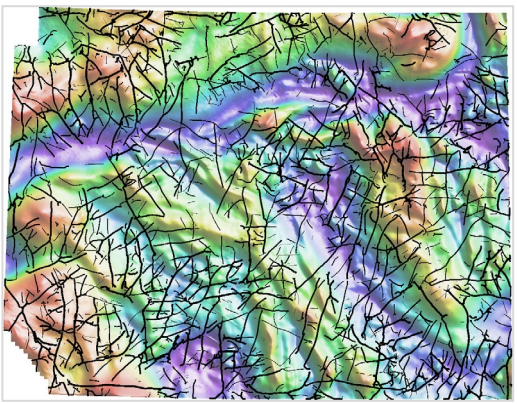

ABS_RMI_Fixed_RTP_AGC20_Struct2000_Cross_Vec

ABS_RMI_Fixed_RTP_HSI_NE

** *Further scales of results also delivered.*

Magnetic data-processing results images (continued)

▶ Radial symmetry analysis — RTP

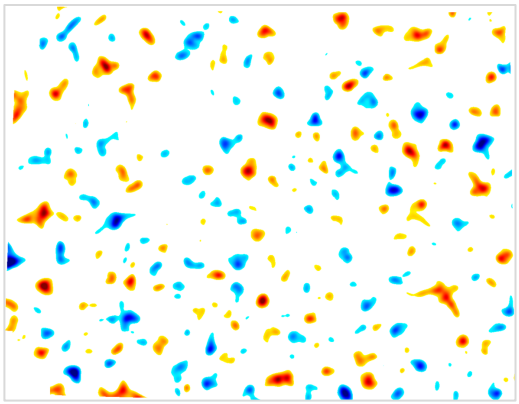

Figure 32: Representative image** showing 4000m magnitude-independent radial symmetry results for the RTP data. TOP: Radially symmetric features detected (both positive and negative anomalies). MIDDLE: Vectorized polygons representing strong anomalies obtained via thresholding. BOTTOM: Polygons co-displayed with the RTP image.

ABS_RMI_Fixed_RTP_res1000_16000_ RSym4000_mi_HighsAndLows

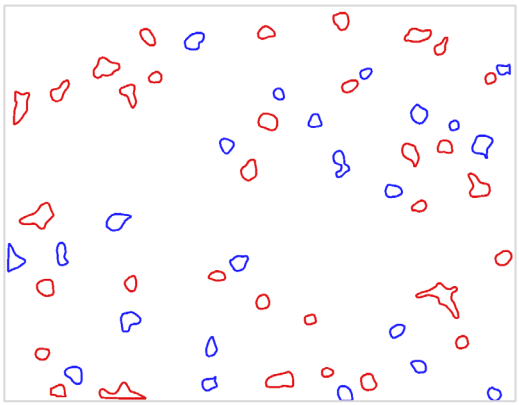

ABS_RMI_Fixed_RTP_res1000_16000_ RSym4000_mi_HTh_Vec_Highs

ABS_RMI_Fixed_RTP_res1000_16000_ RSym4000_mi_HTh_Vec_Lows

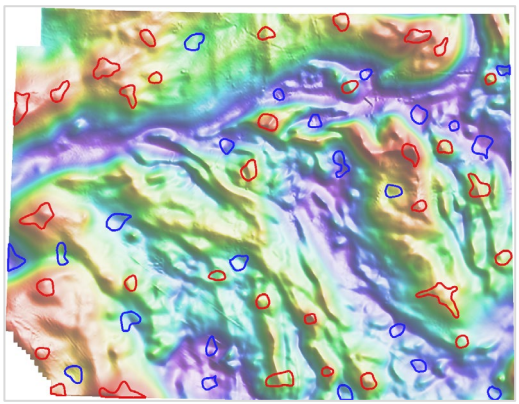

ABS_RMI_Fixed_RTP_res1000_16000_ RSym4000_mi_HTh_Vec_Highs

ABS_RMI_Fixed_RTP_res1000_16000_ RSym4000_mi_HTh_Vec_Lows

ABS_RMI_Fixed_RTP_HSI_NE (grayscale)

** *Further scales of results also delivered.*

Magnetic data-processing results images (continued)

▶ Depth to magnetic source — Depth

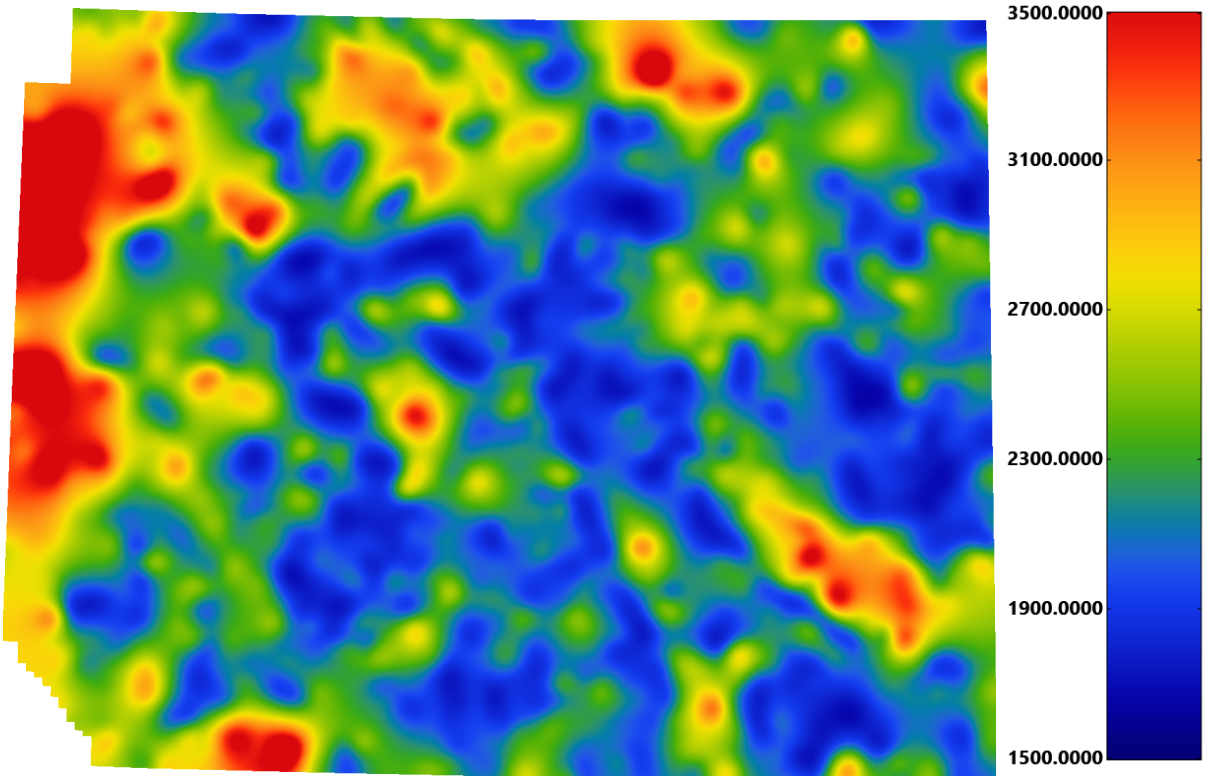

ABS_RMI_Fixed_RTP_res2000_6000_Depth_gs12

Figure 33: The depth to magnetic source results are shown colored according to the color bar on the right. The units are in meters below the topographic surface. The surface is broadly deeper in the northern and western parts of the dataset. It is relatively flat through the rest of the area with only small areas that are deeper. The depths are to magnetic basement. In some cases, this calculation may overestimate the depth to basement if the basement in a given area is non-magnetic.

Magnetic data-processing results images (continued)
▶ Depth to magnetic source — Surface elevation

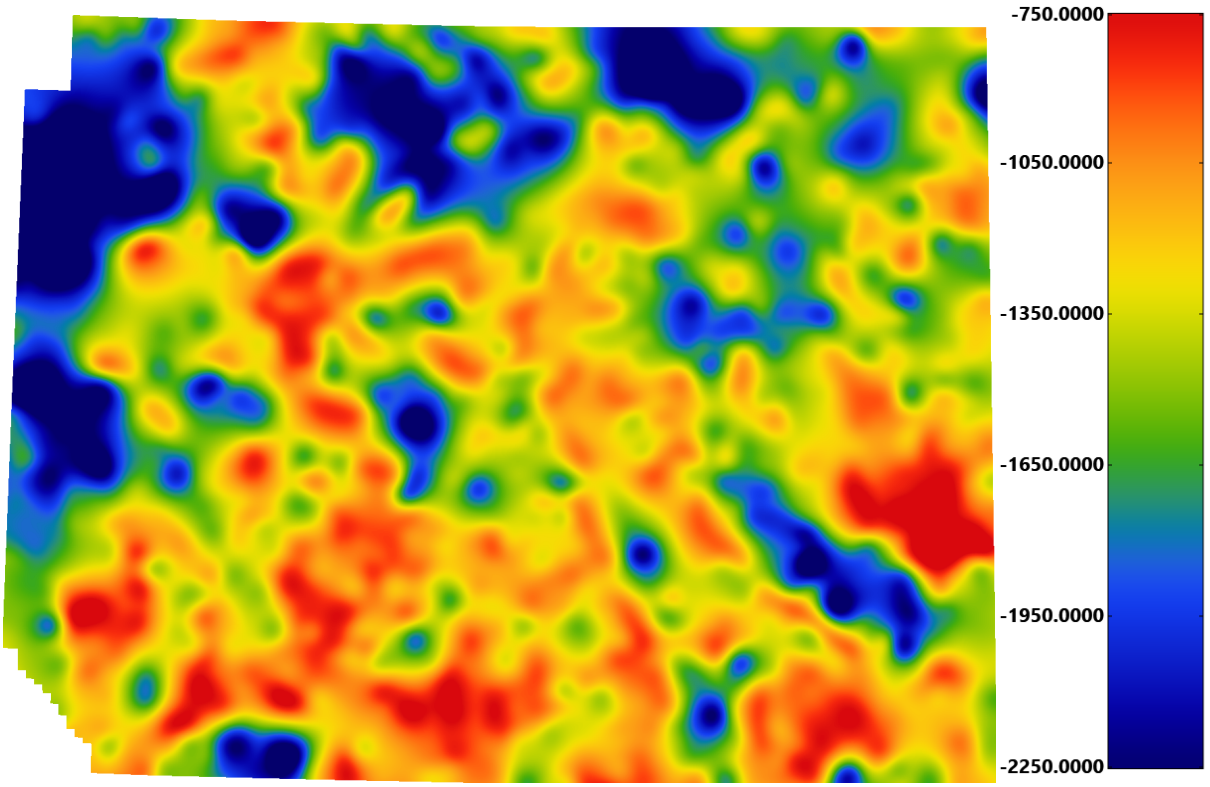

ABS_RMI_Fixed_RTP_res2000_6000_Basement_Surface_gs12

Figure 34: The elevation of the magnetic basement surface is shown colored as indicated by the color bar to the right of the image. The surface elevation shows less variation than the depth to basement. This happens because the far western part of the area has high elevation and that increases the distance to the magnetic source. Therefore the elevation change on the surface in the west is not as great as the depth change.

Appendix 1: Structure detection algorithm

The goal in developing structure detection was to move towards automated interpretation of potential field data that would be most similar to an interpretation by a person. The structure detection is a phase congruency algorithm based on oriented exponential filters (**Kovesi, 1999**).

The structure detection filter is a feature detection algorithm used to highlight ridges, valleys or edges in gridded data. The results are significantly different from other feature detection routines.

Perhaps the biggest difference is that the results are a measure of symmetry or asymmetry, irrespective of amplitude. This is because the analysis is completed using the local phase rather than the signal amplitude.

This means that features in areas of low contrast are highlighted just as well as those in areas of high contrast, as long as the frequencies are present. High values in the structure grid indicate that the structure is close to a step edge. A small step change will have a higher value than a higher amplitude change that is more gradual.

The method is also multi-scale by design. For structures to be highlighted, they must be present at more than one scale. This eliminates more-minor edges that may be present over a narrow frequency range.

The use of exponential filters to determine the scale allows for some inference as to the depth of the structures detected when the filter is applied to potential field data. The wavelength in the filename is the shallowest upward continuation level used and the approximate depth should range between 0.5 and 1 times this wavelength.

This depth estimate is based on **Jacobsen (1987)**. This method is not perfect at separating sources from different depths. It is possible to generate long-wavelength features from shallow sources as evidenced by the fact that there are long wavelength features present in radiometric data, which do not have a significant depth component. However, the method should provide a good first pass estimate of which features extend to depth and which are only surficial. It is possible for deep tapping structures to be missed if there is not a significant property contrast across them.

Appendix 1: Structure detection algorithm (continued)

The structure detection filter produces orientation grids that show the orientation of the strongest edge at a given location. When these orientation grids have been thresholded to remove low amplitude features, it's easier to see the prominent structural orientations.

References

Kovesi, P., 1999, Image Features From Phase Congruency. Videre: A Journal of Computer Vision Research, v. 1, no. 3.

Jacobsen, B.H., 1987, A case for upward continuation as a standard separation filter for potential-field maps. Geophysics, v.52, no. 8, pp. 1138-1148.

Appendix 2: Radial symmetry algorithm

The goal in developing the radial symmetry filter is a move towards automated interpretation of potential field and topographic data that would be most similar to an interpretation by a person.

The filter highlights round features (as opposed to linear features) in the data. This allows us to locate areas that have a higher likelihood of being intrusive bodies or discrete alteration zones.

We have developed several radial symmetry filters. The filter that was used for this project is a gradient-based filter that looks for points where the grid slopes away in all directions. Detected locations are magnetic highs that are discrete bodies. Discrete magnetic lows are areas where the grid slopes toward the location from all directions. This algorithm is based on **Loy and Zelinsky (2002)**.

The filter can be used in a magnitude independent (MI) or magnitude dependent (MD) mode. The MI measure is a strict measure of radial symmetry, making it a direct measure of how round an anomaly is, irrespective of the magnitude of the gradients involved there. The MD measure is the MI measure scaled according to the magnitude of the gradients in the grid.

The filter looks for features with a radius between a base radius and two times that radius. It will not locate features that are significantly smaller than the range used. The filter will highlight the center of some features that are larger than the radius range.

References

Loy G., Zelinsky A., 2002, A Fast Radial Symmetry Transform for Detecting Points of Interest. In: Heyden A., Sparr G., Nielsen M., Johansen P. (eds) Computer Vision — ECCV 2002. ECCV 2002. Lecture Notes in Computer Science, vol 2350. Springer, Berlin, Heidelberg